Physical Modeling and Numerical Simulations of the Slider Air Bearing Problem of Hard

Disk Drives

by

Lin Wu

B.S. (Beijing Institute of Technology, China) 1993

M.S. (Arizona State University) 1997

A dissertation submitted in partial satisfaction of the

requirements for the degree of

Doctor of Philosophy

in

Engineering-Mechanical Engineering

in the

GRADUATE DIVISION

of the

UNIVERSITY of CALIFORNIA, BERKELEY

Committee in charge:

Professor David B. Bogy, Chair
Professor Stanley A. Berger
Professor Ole H. Hald

Spring 2001

The dissertation of Lin Wu is approved:

_____
Chair   Date

_____
                                                                                                         Date

_____
                                                                                                         Date

University of California, Berkeley

Spring 2001

Physical Modeling and Numerical Simulations of the Slider Air Bearing Problem of Hard

Disk Drives

ABSTRACT

Physical Modeling and Numerical Simulations of the Slider Air Bearing Problem of

Hard Disk Drives

By

Lin Wu

Doctor of Philosophy in Engineering-Mechanical Engineering

University of California, Berkeley

Professor David B. Bogy, Chair

The continued increase in the storage density of hard disk drives requires corresponding reduction of the thickness of the air bearing between the slider and the disk surfaces that provides the needed lubrication. The current thickness of the gas layer is already only an order of magnitude larger than the diameter of gas molecules. At such small spacing, the physical models that describe the air bearing phenomenon well at much larger spacing can no longer give predictions close to reality. As a result, it is important to have an improved lubrication model that works under the extremely rarified condition and is free of pressure singularities caused in some existing models by the unavoidable contact between the slider and disk surface at such small spacing. The industry also needs an efficient design code to help design the air bearing surfaces, to ensure that the sliders with the read/write elements attached at their trailing edge fly at desirable attitudes with respect to the moving disk. This thesis focuses on these two topics.

Two new lubrication equations are derived first. They are based on slip velocity assumptions at the gas-solid interface. The new equations are free of contact pressure singularities that some other existing models contain. The causes of these unphysical singularities are also studied.

Next the problem of accurate solution of the lubrication equation is addressed. Unstructured adaptive triangular mesh generation techniques that suit the particular geometry of slider air bearing simulation of hard disk drives are implemented. Different refinement and adaptation techniques are used to generate several levels of good quality mesh over sliders with complex rail shapes. The overall mesh generation procedure offers great flexibility and control over the quality and distribution of the generated mesh, which makes it superior to its much simpler structured counterpart. An explicit vertex based finite volume method based on Patankar's scheme is first constructed. Then the explicit scheme is extended to a fully implicit one. Unconditional stability of the scheme is achieved. A non-nested full approximation storage (FAS) multi-grid algorithm is then used to significantly speed up the convergence rate of the implicit finite volume scheme. The steady state flying attitude of the slider is obtained by a Quasi-Newton iteration method.

To further improve the efficiency and accuracy of the code, three other different multi-grid numerical schemes are presented. The so called flux difference splitting, the multi-dimensional upwind residue distribution and the SUPG finite element techniques are used to discretize the governing equation. Improved results are obtained.

Finally, the intermolecular force effect on the flying attitude of new ultra-low flying slider designs is investigated numerically. It is found that the van der Waals force has

significant influence on the flying height and has non-negligible effect on the pitch angle for both positive pressure sliders and negative pressure sliders, when the flying height is below 5 nm. When the flying height is below 0.5 nm, the repulsive portion of the intermolecular force becomes important and also has to be included.

_____

Professor David B. Bogy,   Chair

To my family members

TABLE OF CONTENTS

LIST OF FIGURES

LIST OF TABLES

Chapter 2

ACKNOWLEDGMENTS

I would like to express my sincere gratitude to my research advisor, Professor David B. Bogy, for his continued academic guidance and financial support throughout my graduate study at University of California at Berkeley. Working with Professor Bogy has been an invaluable and honorable experience from which I will benefit thorough my entire life.

I would also like to thank Professor Stanley A. Berger and Professor Ole H. Hald for their sitting on my qualify exam committee and my dissertation committee. Learning courses from them has been a wonderful experience.

It is my pleasure to thank my colleagues at CML. They have made CML a nice place to stay not only academically but also personally. Special thanks go to fellow graduate student Weidong Huang, Roger Lo, Liangsheng Chen, and a visiting scholar, Dr. Qinghua Zeng.

I also want to thank my parents and my sister and brothers for their continued encouragement and support.

CHAPTER 1

INTRODUCTION

Since its introduction in 1956 by IBM, the hard disk drive (see Fig. 1.1) has become the most important type of data storage device due to its low cost per megabyte, high data access rate and short access time compared with other alternative storage hierarchies such as optical storage and solid state memory. The cost for hard disk drives has recently been reduced to 1 cent per megabyte. The major cause for the rapid and continued decrease of the cost of hard disk drives is the increase of areal storage density. RAMAC, the first hard disk drive from IBM, had an areal density around $10^{-3} MB/in^2$. An areal density of 25 GB/in^2 has already been achieved in today's hard disk drives. The hard disk drive industry's next goal is to increase the areal density to 100 GB/in^2. Projects for 1 TB/in^2 are underway. Thus the areal density has been increased by a factor of ten million in the last four decades. With the introduction of the magnetoresistive (MR) and the giant magnetoresistive (GMR) heads in the earlier 90's, the rate of density increase has reached a factor of 2 every year. Although there are some physical limits (one of them is that the smallest size for a thermally stable magnetic grain is believed to be about 10 nanometers) that will eventually slow down the rapid improvement rate, an even faster rate of increase is foreseeable in the next 10 years.

Reducing the spacing between the read/write transducer and the magnetic bits is one of the most important enabling factors that lead to the increase of areal density, following the scaling law. In a modern hard disk drive, magnetic bits are written and stored on stacks of disks, which usually have a size from 1.5 inches to 3.5 inches in diameter and are mounted on a rotating spindle. The spindle usually rotates at a speed

from a few thousands to tens of thousands revolutions per minute. The accessing of the magnetic bits is achieved through a read/write transducer attached to a small millimeter sized air bearing slider, which is separated from the disk surface to avoid wear by the air-bearing force generated by a thin air layer squeezed into the narrow space between the slider and the disk surface due to the high rotation speed of the disk. The slider is mounted on the tip of a suspension arm, and the suspension arm is controlled by a position motor to locate the magnetic bits on the disk (see Fig. 1.2).

The slider's flying height and other geometric parameters like pitch, skew and roll angles (see Fig. 1.2 for definition), have a profound influence on the read back signals and consequently the performance of the hard disk drives. These geometric parameters are determined by the balance of the forces and torques generated by the spring suspension, the air bearing, and other forces such as intermolecular forces if the spacing approaches molecular distance. In the hard disk drive industry the flying attitude goal is obtained by carefully designing the rail shape of the slider, which is generally very complicated. To reduce the design cost, accurate and efficient steady state air bearing design software is required.

Simulation of the air bearing force accurately and efficiently becomes the key issue in the design of sliders. To simulate the air bearing problem accurately involves two steps. The first step is to model the problem accurately and obtain a physically justified governing equation. For the air bearing problem it is a modified Reynolds lubrication equation. The second one is to develop numerical methods that solve the Reynolds equation accurately and efficiently. This thesis focuses on both issues.

Chapter 2 gives a brief introduction to the generalized lubrication theory for ultra-thin gas layers with minimum spacing under 100 nanometers. Then a new modified Reynolds equation is derived based on physical principles for rarefied gas for compressible and extremely thin layer gas lubrication. For the one dimensional problem, theoretical analysis and numerical simulation are employed to show that the new equation does not predict an unphysical unbounded pressure singularity in the limit of contact between the bearing surface and the moving surface. We also show the same is true for other existing models with higher than first order slippage correction, which introduce additional diffusion terms that are functions of the spacing with similar order to that of the convection terms. These developments remove the ambiguity of some previously published analyses and corrects prior erroneous statements that all existing generalized Reynolds equation models predict nonintegrable singular pressure fields in the limit of contact. The asymptotic analysis also supplies a means for deriving the needed additional boundary condition at the boundary of a contact region. For the two dimensional problem, we again show by numerical analysis that there are no unbounded contact pressure singularities for the new model and other models with corrections higher than first order, and that the singularity is weaker than in the 1-D case for these lower order correction models due to the cross diffusion effect introduced by the additional dimension.

In Chapter 3, new derivations of the first order and the second order velocity slip Reynolds equations are presented. In the previous derivations of the first order and the second order slip models of the generalized Reynolds equation, a length scale equal to the mean free path of the gas molecules was used in a Taylor expansion of the mean velocity

field. The first order slip model comes from a first order Taylor expansion and the second order slip model comes from a second order Taylor expansion. The coefficients of the derived lubrication equation depend on that length scale. The choice of the length scale to be exactly the mean free path is arbitrary to some extent. In this Chapter, the first order and the second order slip models are re-derived by using a somewhat more physical approach, in which the requirement of the expansion length scale to be the mean free path is relaxed. The momentum transfer rate across each surface element is obtained by summing up the contributions from each group of molecules impinging with an angle q to the surface normal within a solid angle dw. New slip velocity boundary conditions at the gas-solid interface are derived and new first order and second order slip lubrication equations are obtained. The new second order slip lubrication equation appears to be preferable to the original one when the inverse Knudsen number is small, and it is free of any contact pressure singularity.

In Chapter 4, unstructured adaptive triangular mesh generation techniques and vertex based finite volume schemes that suit slider air bearing simulation for hard disk drives are constructed and implemented. Different refinement and adaptation techniques are used to generate several levels of good quality mesh over sliders with complex rail shapes. At each level, either one geometrical or one physical property of the problem is captured. The overall mesh generation procedure offers great flexibility and control over the quality and distribution of the generated mesh, which makes it superior to its much simpler structured counterpart. An explicit vertex based finite volume scheme is first constructed. The modified Reynolds equation is locally integrated over the control volumes that are taken to be the Voronoi polygons. Backward differencing is used to discretize the

unsteady term. Patankar's strategy is used to evaluate the numerical flux across each edge of the control volumes. A local time stepping technique is adopted to speed up the convergence rate. To further improve the convergence rate, the explicit scheme is extended to a fully implicit one, and the resulting simultaneous linear algebraic equations are solved iteratively by the Gauss-Seidel method. Unconditional stability of the scheme is achieved, and preliminary calculation shows rapid convergence compared to the explicit scheme.

In Chapter 5, a non-nested full approximation storage (FAS) multi-grid algorithm over unstructured triangular meshes is presented. The multi-grid algorithm can significantly speed up the convergence rate of the implicit finite volume scheme presented in the previous chapter. The multi-grid algorithm requires no relationship between the fine and coarse meshes, which offers greater convenience and flexibility in the mesh generation and takes into account the fact that the mesh generated by Delaunay triangulation in the previous chapter is not nested. When combined with the implicit and adaptive finite volume scheme that has been shown to have good high frequency error damping qualities, it achieves fast convergence. The overall simulation strategy, including the mesh generation and adaptation, the implicit finite volume scheme and the multi-grid algorithm, has proved to be an efficient way of solving the generalized Reynolds equation over sliders with complex rail systems. In addition, the steady state flying attitude is obtained by a Quasi-Newton iteration method.

In Chapter 6, we present and compare three different multi-grid numerical schemes over unstructured triangular meshes. For each fixed slider attitude the air bearing pressure is obtained by solving the generalized Reynolds equation using one of the three

schemes. In the first scheme the convection part of the generalized Reynolds equation is modeled by the "flux difference splitting" technique. Higher order accuracy in space is achieved by a linear reconstruction technique with flux limiters incorporated to prevent oscillation in the high-pressure gradient regions. In the second scheme the convection part is modeled by the multi-dimensional upwind residue distribution approach. In the third scheme the SUPG finite element approach, cast in residue distribution form, is used to model the convection part. In all three schemes, a Galerkin method is used to discretize the diffusion terms. The results of the current three schemes and the other two schemes are compared.

When the spacing between the slider and the disk is smaller than 10 nm, the effect of the intermolecular forces between the two solid surfaces can no longer be ignored. This effect on the flying attitude of practical slider designs is investigated in Chapter 7 numerically. The 3-D slider surface is discretized into non-overlapping unstructured triangles. The intermolecular forces between each triangular cell of the slider and the disk surface are formulated, and their contributions to the total vertical force, as well as the pitch and roll moments, are included in the steady state air bearing design code presented in previous chapters. It is found that the van der Waals force has significant influence on the flying height and has non-negligible effect on the pitch angle for both positive pressure sliders and negative pressure sliders, when the flying height is below 5 nm. When the flying height is below 0.5 nm, the repulsive portion of the intermolecular force becomes important and also has to be included.

Fig. 1.1 The IBM Travelstar 25GB hard disk drive.
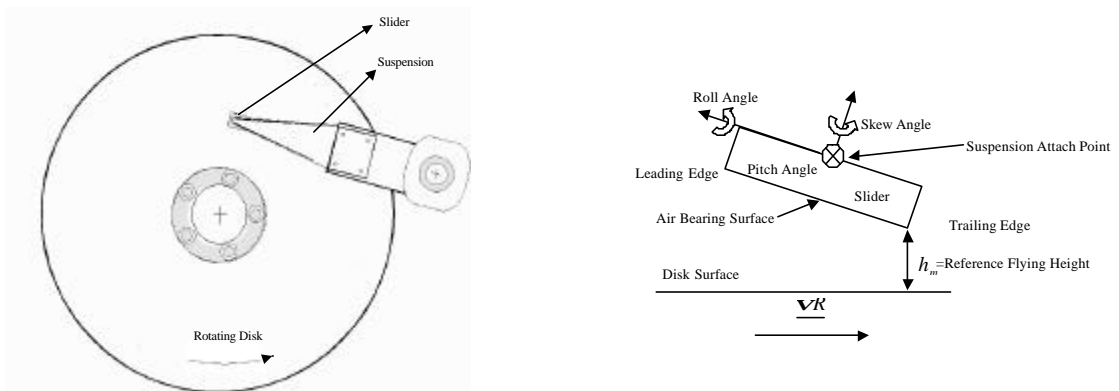
Fig. 1.2 A sketch of the hard disk drive assembly.

CHAPTER 2

A GENERALIZED COMPRESSIBLE REYNOLDS LUBRICATION EQUATION

WITH BOUNDED CONTACT PRESSURE

2.1. Introduction

In gas lubrication bearings contact between the bearing surface and the moving surface is unavoidable under certain situations. The contact gas bearing pressure plays an important role in the dynamic response of bearing systems with intermittent contact. In modern hard disk drives, the read-write head flies above the disk where magnetic information is stored at a height generally less than 50 nm. The extremely thin air bearing between the slider (head) and rotating disk provides the necessary equilibrating lifting force, so the head can fly at the desired height. To increase the areal density further, to the range of 1 Tbit/in^2, a flying height around 3nm is believed to be necessary. The peak-to-peak roughness of the disk surface is unavoidable and may be about 10-20 nanometers. As a result, intermittent contact between the slider and the disk could be a frequent phenomenon. To predict the bearing pressure accurately, even when actual contact occurs, becomes extremely important in the design of the components of the hard disk drive and other near contact gas lubrication systems.

At these low flying heights, which are only a fraction of the gas molecular mean free path, the traditional macroscopic Reynolds equation based on the continuum assumption with non-slip boundary conditions is no longer valid. Two approaches to modify the Reynolds equation, taking into account the slippage at the boundaries and

rarefication effects, have been presented in the literature. The first order slip model of Burgdorfer (1959), the second order slip model of Hsia and Domoto (1983) and the 1.5 order slip model of Mitsuya (1993) fall under the first approach, which incorporates different order slippage boundary conditions into the integration of the traditional macroscopic continuum compressible Stokes equation under the isothermal assumption. The FK model of Fukui and Kaneko (1988) is an example of the second approach, which uses the linearized Boltzmann equation with slip boundary conditions.

There has been a widely accepted view that all of the above models predict unbounded nonintegrable, singular pressure fields at contact points (Anaya-Dufresne and Sinclair, 1997, Huang and Bogy, 1998 and Huang et al., 2000). Although Anaya-Dufresne and Sinclair's three term simple polynomial expansion analysis did show there is a possibility that the lowest order term is non-singular at the contact point (Anaya-Dufresne and Sinclair, 1997), their purpose was to find the orders of possible singularity solutions in simple polynomial form, but their analysis could not determine if contact pressure singularities actually occur. In a related problem Anaya-Dufresne (1996) successfully removed the contact singularity in the incompressible Taylor plate scraping problem by introducing additional slippage into Maxwell's slip boundary condition through a momentum balance inside the Knudsen layer where the molecules collide or bounce back from collision with the solid wall. He derived a new incompressible Reynolds equation using the new slip boundary condition, and he showed that the equation does not predict a contact pressure singularity. He also numerically showed that the incompressible second and 1.5 order slip models do not have contact pressure singularities. He also assumed that the same conclusions would hold for the compressible case even though he did no

further analysis. Here we extend his approach to derive a slip boundary condition at the gas-solid boundary for the compressible case, which is found to be essentially the same as that of the incompressible case (Anaya-Dufresne, 1996). Therefore, to a first order approximation, compressibility can be ignored in this derivation. Also a 2-dimensional modified Reynolds equation is derived by incorporating the modified slip boundary condition into the Stokes equation. The resulting equation has a form similar to that of the second order and the 1.5 order correction models, differing only by the coefficients in the diffusion terms.

Analytical solutions are derived near the contact point for a 1-dimensional parabolic asperity contact problem, using the first order and second order slip models after simplification of the governing equations by dimensional analysis. Numerical solutions of the full equations are also obtained by a finite volume scheme. The theoretical and numerical solutions are found to be in excellent agreement, and they show there is no unbounded pressure singularity at the contact point for second order type models. This is contradictory to previous analysis and assertion (Anaya-Dufresne and Sinclair, 1997, Huang and Bogy, 1998 and Huang et al., 2000). As the minimum spacing is reduced to near contact, a narrow boundary layer appears near the contact point within which the pressure quickly drops from the upwind positive value to a sub-ambient value downwind of the point. A shock wave like bounded discontinuity appears when actual contact occurs, which is consistent with the fact that the upwind and downwind transfer of information is blocked by the contact. This spacing reduction limiting process suggests a way to supply the additional boundary condition needed at the contact edge to solve the problem in which gas is funneled into a converging corner or expands from a

diverging corner. Since the Reynolds equation is second order it needs two boundary conditions. In the far field ($X = \pm 1$), ambient pressure is assumed as one boundary condition, but it is somewhat difficult to envision the appropriate boundary condition at the contact edge. The asymptotic values obtained from another problem with symmetrical geometry immediately before or after the discontinuity can be used as the boundary condition at the contact point for the converging corner or the diverging corner problem.

It is then shown that unbounded pressure fields are predicted by the first order slip model and the FK model near the contact region. This happens because the order of the diffusion terms expressed as functions of the spacing parameter of the first order slip model and the FK model are higher than those of the convection terms, so the convection effect has no balancing diffusion counter part. Thus the unbounded and nonintegrable pressure singularity is unavoidable in these cases. The singularity in the first order slip model is stronger than that of the FK model, due to the fact that the diffusion term of the first order slip model is asymptotically smaller than in the FK model. We conclude from this asymptotic analysis that removal of the contact singularity, which is viewed as non-physical, requires the diffusion term to scale to the same order in the spacing as the convection term.

For the two dimensional problem in which the 1-D parabolic asperity is rotated about its symmetry axes, similar conclusions can be reached by numerical calculation. The only difference is that the pressure profile is smoother and without the discontinuity for the higher order correction models and the singularity is weaker for models that have a contact singularity.

2.2. Derivation of a Modified Reynolds Equation with Bounded Contact Pressure

For low Reynolds number steady state flow, the governing equation is the Stokes equation. After taking into account the small slope and much smaller spacing in the bearing thickness direction than the length scales in the horizontal directions, one obtains the following lubrication equations

$$\frac{\partial}{\partial x}(\boldsymbol{r}u) + \frac{\partial}{\partial y}(\boldsymbol{r}v) = 0 ,$$

$$0 = -\frac{\partial p}{\partial x} + \boldsymbol{m}\frac{\partial^2 u}{\partial z^2} ,$$

$$0 = -\frac{\partial p}{\partial y} + \boldsymbol{m}\frac{\partial^2 v}{\partial z^2} ,$$

$$\frac{\partial p}{\partial z} = 0 , \tag{2.1}$$

where p is the pressure, $\boldsymbol{m}$ is the dynamic viscosity of the gas, u and v are gas velocities in the x and y directions, respectively. The above equations can be integrated in the z direction to give the velocity distribution. But two boundary conditions are needed, one at the upper and one at the lower gas-solid interfaces.

The Maxwell slip velocity at the gas-solid interface is derived by equating the momentum transfer rate from the gas molecules to the solid wall through collisions to the macroscopic shear stress of the gas at the solid wall (Kennard, 1938),

$$u_{slip} = \frac{2-a}{a}l\frac{\partial u}{\partial z}\bigg|_{z=0} = al\frac{\partial u}{\partial z}\bigg|_{z=0}, \qquad (2.2)$$

where a is the accommodation coefficent representing the portion of the molecules inside the Knudsen layer that collide with the wall, which usually is taken to be 1. a is the surface correction coefficient. In solving Taylor's incompressible plate scraping problem, Anaya-Dufresne (1996) argues that when the scraper is vertical, $u = 0$ along the scraper and so $\frac{\partial u}{\partial z} = 0$ at the contact point, so eq. (2.2) gives zero slip velocity there where a maximum slip velocity, which reduces the mean velocity to zero, is required physically. As a result, he used momentum balance along the wall direction inside the Knudsen layer, so the normal stress gradient in the direction of the moving plate also forces some slippage. Here we extend his idea to derive a compressible slip boundary condition. By using a control volume with a length $\Delta x, \Delta y$ and $\Delta z = l$ in the x, y and z directions, respectively (see Fig. 2.1), ignoring higher order terms, and applying the x momentum balance we obtain

$$t_{x0} = m\frac{\partial u}{\partial z}\bigg|_{z=l} + l\frac{\partial s_x}{\partial x}\bigg|_{z=\frac{1}{2}l}, \qquad (2.3)$$

where

$$t_{x0} = \frac{r\bar{c}au_{slip}}{2(2-a)}$$

13

is the momentum transfer rate from the gas molecules to the solid wall (Kennard, 1938). $\bar{c}$ is the average molecular speed, u_{slip} is the slip velocity in the x direction. $\boldsymbol{s}_x$ is the normal stress

$$\boldsymbol{s}_x = -p - \frac{2}{3}\boldsymbol{m}liv\underline{u} + 2\boldsymbol{m}\frac{\partial u}{\partial x}. \tag{2.4}$$

Just as in the derivations of the first and second order slip boundary conditions, the length of the control volume in the direction normal to the wall is assumed to be the mean free path. Since $\boldsymbol{l}$ is a small number, on the order of 10^{-8}, and ignoring higher order effects, we can evaluate the terms on the right hand side of eq. (2.3) at $z = 0$ instead of at $z = \boldsymbol{l}$ and $z = \boldsymbol{l}/2$, respectively. Substituting eq. (2.4) into eq. (2.3) and using the relationship (Kennard, 1938)

$$\boldsymbol{m} = \frac{1}{2}\,r\bar{c}\boldsymbol{l}$$

while keeping terms $O(\boldsymbol{l})$, we obtain for the slip velocity in the x direction

$$u_{slip} = \frac{(2-\boldsymbol{a})}{\boldsymbol{a}}\left(\boldsymbol{l}\frac{\partial u}{\partial z} - \frac{2\boldsymbol{l}}{r\bar{c}}\frac{\partial p}{\partial x}\right), \tag{2.5a}$$

which is exactly the same as that derived by Anaya-Dufresne (1996) for an incompressible gas. Therefore compressibility introduces only higher order effects that

can be ignored in the first order approximation. Similarly, we can derive the slip velocity in the y direction

$$v_{slip} = \frac{(2-\boldsymbol{a})}{\boldsymbol{a}}\left(\boldsymbol{l}\frac{\partial v}{\partial z} - \frac{2\boldsymbol{l}}{\boldsymbol{r}c}\frac{\partial p}{\partial y}\right). \qquad (2.5b)$$

The velocity components u and v can be obtained as functions of z after integrating eq. (2.1) and applying equations (2.5a) and (2.5b) at the upper and lower solid surfaces. The compressible Reynolds equation then follows from substituting the velocities into and integrating the continuity equation. After using the assumptions that the gas is ideal and the gas layer is isothermal, we obtain

$$\frac{\partial}{\partial X}\left[\left(PH^3 + \boldsymbol{b}K_n H^2 + \boldsymbol{g}K_n^2 \frac{H}{P}\right)\frac{\partial P}{\partial X}\right] + \frac{\partial}{\partial Y}\left[\left(PH^3 + \boldsymbol{b}K_n H^2 + \boldsymbol{g}K_n^2 \frac{H}{P}\right)\frac{\partial P}{\partial Y}\right]$$
$$= \Lambda_x \frac{\partial}{\partial X}(PH) + \Lambda_y \frac{\partial}{\partial Y}(PH)$$

$$(2.6)$$

In the above equation, P and H are the dimesionless pressure and spacing between the upper and lower surfaces, normalized by the ambient pressure p_a and the smallest spacing h_0, respectively. $K_n = \boldsymbol{l}_a/h_0$ is the ambient Knudsen number, and $\boldsymbol{l}_a$ is the ambient mean free path. $\Lambda_x = 6\boldsymbol{m}UL/p_a h_0^2$ and $\Lambda_y = 6\boldsymbol{m}VL/p_a h_0^2$ are the bearing numbers in the x and y directions, respectively, which represent the relative importance between the convection effect and the diffusion effect. L is the horizontal length scale. X and Y are

15

dimensionless coordinates normalized by L. $\boldsymbol{b}$ and $\boldsymbol{g}$ are two model constants, which for the current derivation, are $\boldsymbol{b} = 6a$ and $\boldsymbol{g} = 12a$. Other slip models are also represented by different values of $\boldsymbol{b}$ and $\boldsymbol{g}$. In fact, $\boldsymbol{b} = 6a$ and $\boldsymbol{g} = 0$ gives the first order slip model of Burgdorfer (1959), $\boldsymbol{b} = 6a$ and $\boldsymbol{g} = 6a$ gives the second order slip model of Hsia and Domoto (1983), and finally $\boldsymbol{g} = 6a$ and $\boldsymbol{g} = 8/3$ gives the 1.5 order slip model of Mitsuya (1993).

2.3. 1-D Theoretical and Numerical Solutions Near a Contact Point

We consider the 1-D problem of a moving surface with velocity U nearly contacted by a fixed asperity as shown in Fig. 2.2. To simplify the problem, we specify the dimensionless shape of the asperity as a parabola

$$H = \frac{AL^2}{h_0} X^2 + 1, \tag{2.7}$$

in which $A = 10^4 \ 1/M$, $L = 0.5\boldsymbol{m}M$. These parameters represent a typical size of the asperities in hard disk drives. The gas is assumed to be air at room temperature, under normal working conditions, $\boldsymbol{m} = 1.85 \times 10^{-5} N \cdot S / M^2$, $p_a = 0.101 MPa$, $\boldsymbol{l} = 65NM$, $U = 10M/S$. h_0 is considered to be about 1 NM or less, approaching zero. For the one-dimensional case eq. (2.6) can be simplified and rearranged into

16

$$\frac{\partial}{\partial X}\left[\left(\frac{p_a h_0^2}{6\textbf{\textit{m}}UL}PH^3 + \frac{\textbf{\textit{b}}p_a \textbf{\textit{l}}h_0}{6\textbf{\textit{m}}UL}H^2 + \frac{\textbf{\textit{g}}p_a \textbf{\textit{l}}^2}{6\textbf{\textit{m}}UL}\frac{H}{P}\right)\frac{\partial P}{\partial X}\right] = \frac{\partial}{\partial X}(PH). \qquad (2.8)$$

It is seen that the first two terms on the diffusion side are functions of the minimum spacing h_0, but the third term is not for models where $\textbf{\textit{g}}$ is not equal to zero. As the spacing is reduced to contact or near contact, the first two terms can be dropped near the contact region, while the third term remains and provides the higher order slip effects. This regime is refered to as the higher order slip effect regime. Notice that the first and second terms increase as the third and second powers of H, respectively. When H is increased somewhat, the second term dominates the third term and this is refered to as the first order slip effect regime, since its diffusion effect is dominated by the first order slip correction. As H increases further, the first term becomes dominant and the traditional continuum and non-slip regime is recovered.

For the problem under consideration here, the first two terms are much smaller than the third one even at the outer edge ($X = \pm 1$) where the largest H is found. As a result it is reasonable to keep only the third term. We define a new dimesionless parameter

$$\Gamma = \frac{\textbf{\textit{g}}p_a \textbf{\textit{l}}^2}{6\textbf{\textit{m}}UL}. \qquad (2.9)$$

17

Later we will show that the pressure distribution near the contact region depends only on this new parameter and one boundary condition at $X = 1$ or -1. Eq. (2.8) now assumes the simplified form

$$\frac{\partial}{\partial X}\left[\Gamma\frac{H}{P}\frac{\partial P}{\partial X}\right] = \frac{\partial}{\partial X}(PH),$$ (2.10)

which can be integrated once to give

$$\frac{dP}{dX} - \frac{1}{\Gamma}P^2 - \frac{C}{\Gamma H}P = 0,$$ (2.11)

where C is an integration constant. This is a Riccati equation which can be readily integrated again. After using the boundary condition at $X = -1$, we obtain

$$\frac{1}{P} = Exp\left(-\frac{C}{\Gamma}\int_{-1}^{X}\frac{1}{H}dx\right)\left[\frac{1}{P_L} - \frac{1}{\Gamma}\int_{-1}^{X}Exp\left(\frac{C}{\Gamma}\int_{-1}^{X}\frac{1}{H}dX\right)dX\right],$$ (2.12)

where C can be obtained from the boundary condition at $X = 1$. Since the right hand side of eq. (2.12) is quite complicated, a numerical root finding code similar to that of Ridders's method (Press et al., 1992) is needed to find C. Using the geometry specified in eq. (2.7), we obtain from eq. (2.12)

18

$$P = Exp\left\{\frac{C}{\Gamma L}\sqrt{\frac{h_0}{A}}\left[Atan\left(\sqrt{\frac{A}{h_0}}L\right) + Atan\left(\sqrt{\frac{A}{h_0}}LX\right)\right]\right\} \cdot$$

$$\left\{\frac{1}{P_L} - \frac{1}{\Gamma}\int_{-1}^{X}Exp\left[\frac{C}{\Gamma L}\sqrt{\frac{h_0}{A}}\left[Atan\left(\sqrt{\frac{A}{h_0}}L\right) + Atan\left(\sqrt{\frac{A}{h_0}}LX\right)\right]\right]dX\right\}^{-1} \cdot \quad (2.13)$$

Then letting h_0 approach zero, we obtain the following closed form asymptotic solution with actual contact at $X = 0$ after using the boundary condition at $X = 1$,

$$P = \begin{cases} \dfrac{P_L\Gamma}{\Gamma - P_L(1+X)}, & -1 \le X < 0 \\[3mm] \dfrac{P_R\Gamma}{\Gamma + P_R(1-X)}, & 0 < X \le 1 \end{cases} \quad (2.14)$$

When h_0 approaches zero in (2.13), C approaches to infinity so as to maintain $Ch_0^{0.5}$ constant to satisfy the boundary condition at $X = 1$.

An interesting property of the solution (2.14) is that a shock wave like discontinuity appears at the contact point. Before the contact point ($X < 0$), the solution depends only on the left boundary condition at $X = -1$. While the solution after the contact point ($X > 0$) depends only on the right boundary condition at $X = 1$. This is reasonable physically, since the contact blocks communication between the two sides. Expression (2.14) clearly shows that the solution of the higher order slip correction model is bounded and integrable around the contact point.

To demonstrate that the present asymptotic analysis is valid we also numerically solved the full equation (2.8) with the boundary conditions $P_L = P_R = 1$, using a finite volume method for the convection and diffusion type equations similar to that in Patankar (1980). Figure 2.3 shows the pressure profiles predicted by the 1.5 order slip model ($g = 8/3$) for different values of the minimum spacing. The analytical and numerical solutions are shown to be in good agreement in the limit of small spacing, which justifies discarding the higher order terms. As the minimum spacing is reduced, both the analytical and numerical solutions approach the asymptotic solution given by eq. (2.14). The solution clearly shows a boundary layer behavior near the minimum spacing point before the contact occurs. Furthermore, at contact the solution breaks into two separate branches at the contact point to form a shock wave type discontinuity. Figures 2.4 and 2.5 show similar curves of the second order slip model ($g = 6a$) and our new slip model ($g = 12a$).

From Figs 2.3-5, it is seen that the different models predict different pressures at the contact point, and the limit contact pressure at the upwind side is also quite different from that at the downwind side. The contact pressure at the upwind side is larger than the ambient pressure, due to the fact that although the contact brings the mean gas velocity to zero, the random motion of the gas molecules still produces a non-zero pressure at that point, the converging geometry compresses more molecules there than in the ambient region. As a result, a higher than ambient pressure is expected at the upwind contact edge. A similar explanation can be used to explain why the contact pressure at the downwind side is lower than the ambient value. But neither value is zero, as was assumed by Huang and Bogy (1998). In their paper, the authors assumed that when the

20

spacing is below the diameter of the gas molecules there are no gas molecules to provide pressure. As a result, they suggested setting the pressure to zero at each grid point where the spacing is below the gas molecule diameter as a numerical boundary condition in the numerical simulation to avoid the contact singularity. The above results suggest that their simple treatment may not be good enough to capture the complete physics at the contact point. Physically there must be a pressure jump from the region with a spacing larger than the molecule diameter to the region smaller than the molecule diameter. It is justified to set the pressure equal to zero in regions where gas molecules can not enter, but on the gas side edge, a value like that given by eq. (2.14) is needed to serve as the boundary condition. It is noted that Huang and Bogy's DSMC simulation (1998) also showed a subambient pressure in the downwind portion.

Based on the above analysis, we now propose a way to supply the one needed boundary condition for contact geometries as shown in Fig. 2.6. For the left converging corner, one boundary condition at grid point $i = N$ is needed before the second order Reynolds equation can be solved numerically. If the geometry between grid points $i = N - 1$ and $i = N$ can be approximated by a parabola, then the contact pressure at the upwind side given by eq. (2.14) can be used at point N, while the length scale L is defined as $dX = X_N - X_{N-1}$. Result (2.14) also implies that L (the grid size) must be small enough to make Γ large enough so the denominator will not become zero when X is in the range -1 to 0. For geometries other than a parabola, similar analyses can be conducted to derive a formula like eq. (2.14). Similar arguments hold for the right diverging corner problem.

For the first order slip model, $\boldsymbol{g} = 0$, and the third term on the left hand side of eq. (2.8) drops out. Then we only need to keep the second term to get

$$\frac{\partial}{\partial X}\left(\frac{\boldsymbol{b}p_a\boldsymbol{l}h_0}{6\boldsymbol{m}UL}H^2\frac{\partial P}{\partial X}\right) = \frac{\partial}{\partial X}(PH). \tag{2.15}$$

After using the boundary condition at $X = -1$, we can integrate this simplified equation to obtain

$$P = Exp\left(\int_{-1}^{X}\frac{\Lambda}{\boldsymbol{b}k_n}\frac{1}{H}dX\right)\cdot\left[1 + \frac{C\Lambda}{\boldsymbol{b}k_n}\int_{-1}^{X}\frac{1}{H^2}EXP\left(-\int_{-1}^{X}\frac{\Lambda}{\boldsymbol{b}k_n}\frac{1}{H}dX\right)\right]. \tag{2.16}$$

This equation has an unbounded singularity at the contact point.

For the FK model, near the contact point, the Reynolds equation can be written as

$$\frac{\partial}{\partial X}\left[-\frac{2\boldsymbol{l}P_ah_0}{\boldsymbol{p}\boldsymbol{m}UL}H^2\log\left(\frac{\sqrt{\boldsymbol{p}}h_0}{2\boldsymbol{l}}PH\right)\right] = \frac{\partial}{\partial X}(PH), \tag{2.17}$$

which can not be solved analytically.

Figures 2.7 and 2.8 show the numerical solutions of the first order slip model and the FK model as the minimum spacing is reduced, respectively. The two figures clearly demonstrate a trend toward an unbounded pressure singularity at the zero spacing when contact occurs. They also show the singularity is weaker for the FK model. At very

small spacing the pressure profile is almost symmetric around the contact point as opposed to the antisymmetric results in the bounded solutions and previous DSMC solutions of Huang and Bogy (1998). In fact this kind of behavier can be seen from eq. (2.15) and (2.17). When contact occurs, we can not use expression (2.7) to describe the geometry. Instead $H = AL^2 X^2/h_0$ can be used, where h_0 is taken to be a nonzero small characteristic spacing. $H->0$ as the contact point is approached. The diffusion term of the first order slip model scales like $O(H^2)$, while in the FK model it scales like $O(-H^2 \log H)$. When $H->0$, these terms are much smaller than the convection term, and as a result they can be ignored. The unbalanced convection produces a singular pressure C/H, where C is an integration constant. If the asperity geometry H is defined by a symmetric function about $X=0$ (as for the previously studied parabola), the singular pressure profile is also symmetric about $X=0$. Since $O(-H^2 \log H) >> O(H^2)$ as $H->0$, a weaker pressure singularity is expected for the FK model than for the first order slip model.

Since the convection term of the generalized Reynolds equation is $O(H)$ as $H->0$ the diffusion terms must also scale like $O(H)$ in order to balance the convection effect. Otherwise an $O(1/H)$ singularity is unavoidable. It was shown that for all the existing models only the 1.5 order slip model, the second order slip model and the new model derived here obey this kind of asymptotic behavior near the contact point. As a result, they are free of a contact pressure singularity. Other models which violate this condition, i.e. the first order slip model, the FK model and the continuum model, experience an unbounded contact pressure singularity.

2.4 2-D Numerical Solution Near a Contact Point

The two dimensional problem is much more difficult to treat analytically, so here we use numerical methods to demonstrate that the conclusions for the 1-D problem also hold for the 2-D problem. The asperity is taken to be the axisymmetric one obtained by rotating the parabola (2.7). The domain is taken to be a square region $-1 \le X \le 1$ and $-1 \le Y \le 1$.

Since the performance of the higher order corrections and the new model are qualitatively the same, here we just use the second order slip model as an example. Figure 2.9 shows the pressure distributions along the $Y = 0$ center line. As the spacing is reduced, the pressure profile becomes steeper. When $h_0 = 1E - 12M$, the curve is almost the same as that with contact. The contact curve does not have a shock wave discontinuity at the contact point, as did the 1-D problem, and the pressure distribution is much smoother than that of the 1-D problem with a lower peak pressure. This can be attributed to the cross diffusion effect introduced by the additional Y dimension. Figure 2.10 shows the pressure contour.

Figure 2.11 clearly demonstrates a trend of an unbounded singular pressure field for the first order slip model at the contact point as was seen in the 1-D problem. But its peak pressure is lower than that of the 1-D problem, which implies a weaker contact singularity here than in the 1-D problem. Figure 2.12 shows the corresponding pressure contours.

Figures 2.13 and 2.14 show the results for the FK model, and it is seen that they have the same quality as that of the first order slip model with a less steep distribution and lower peak pressure. They show contact singularities that appear to be weaker than that of the first order slip model.

2.5 Discussion and Conclusion

Following the approach of Anaya-Dufresne (1996) to derive a slip boundary condition at the gas-solid interface through a momentum balance along the wall direction for the incompressible problem, we obtained the compressible counterpart, which is found to be the same as that of the incompressible case. The compressibility only introduces a higher order effect that can be ignored in the first order approximation. A new modified Reynolds equation for isothermal and compressible gas lubrication is then derived by using the new slip boundary condition. The resulting equation has a form similar to that of the second order and the 1.5 order slip models in the literature but with different coefficients that come from terms associated with the higher order slippage correction. However the higher order slippage correction terms of the second and 1.5 order slip models were derived from a purely mathematical point of view, i.e. they come from the second order Taylor series expansion terms of the velocity field in the derivation of the slip boundary condition. In our derivation they come from the additional slippage introduced by the Poiseuille flow effect.

Theoretical and numerical simulations performed on a 1-D parabola contacting asperity show that there are no unbounded contact singularities for these higher order correction models. Instead, a shock wave like discontinuity appears at the contact point. When the asperity approaches contact, a boundary layer appears around the minimum spacing point. As the spacing is reduced, the pressure curve approaches continuously the one for contact. A new contact boundary condition for the Reynolds equation at the converging or diverging corner is proposed, based on the asymptotic analysis, which can be used as the numerical boundary condition at the contact edge in the numerical simulation if locally the geometry near the contact point can be approximated by a parabola. For the first order slip model and the FK model, we analytically and numerically showed that a symmetric contact singularity of $O(1/H)$ appears at the contact point as $H->0$. A general conclusion can be drawn, that for any modified Reynolds equation to be free of a contact singularity, it must have diffusion terms that go to zero no faster than the convection terms near the contact point as the minimum spacing is reduced to zero.
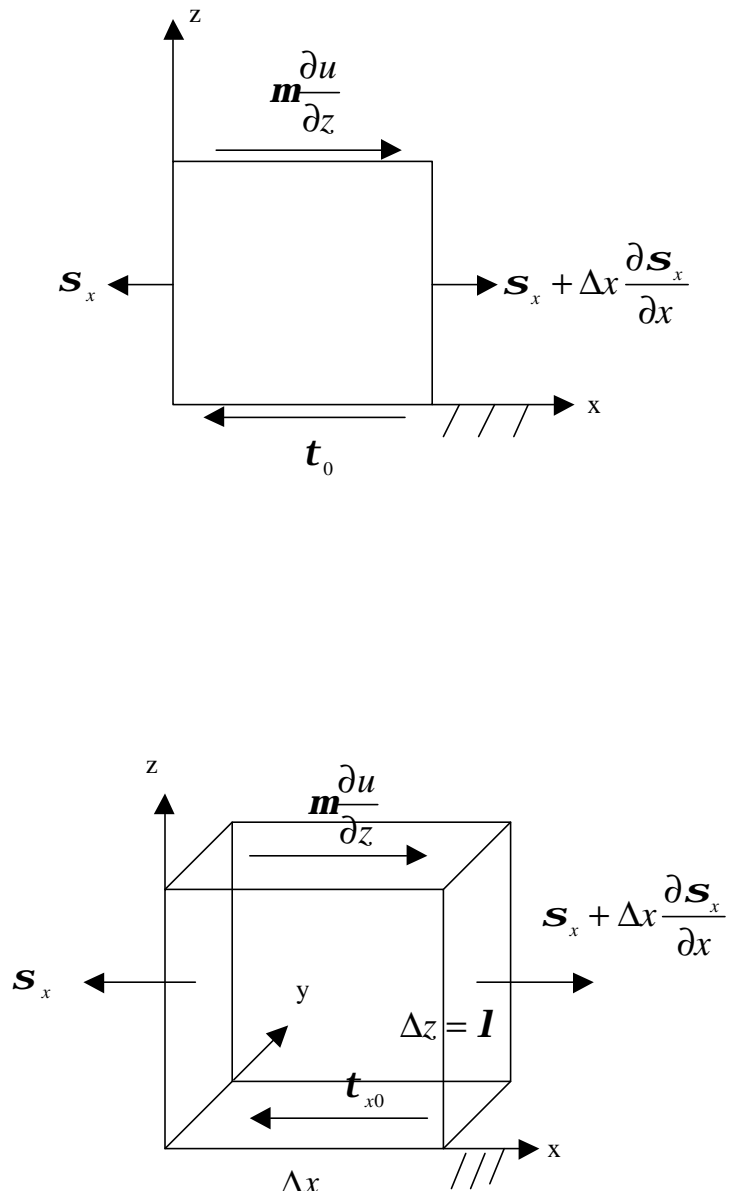
Fig. 2.1 The control volume for momentum balance in the x direction with higher order stress contributions ignored under gas lubrication condition.
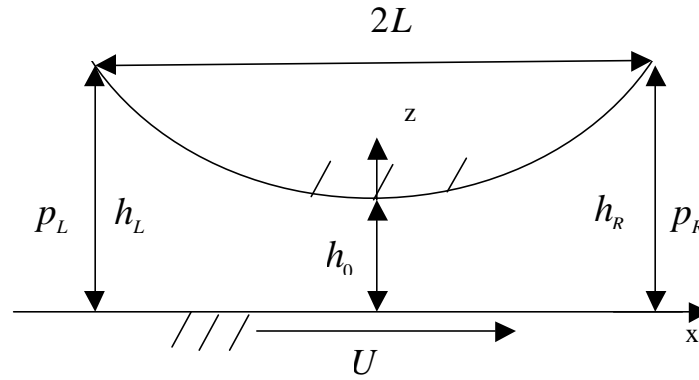
Fig. 2.2 The assumed geometry of the contacting asperity.
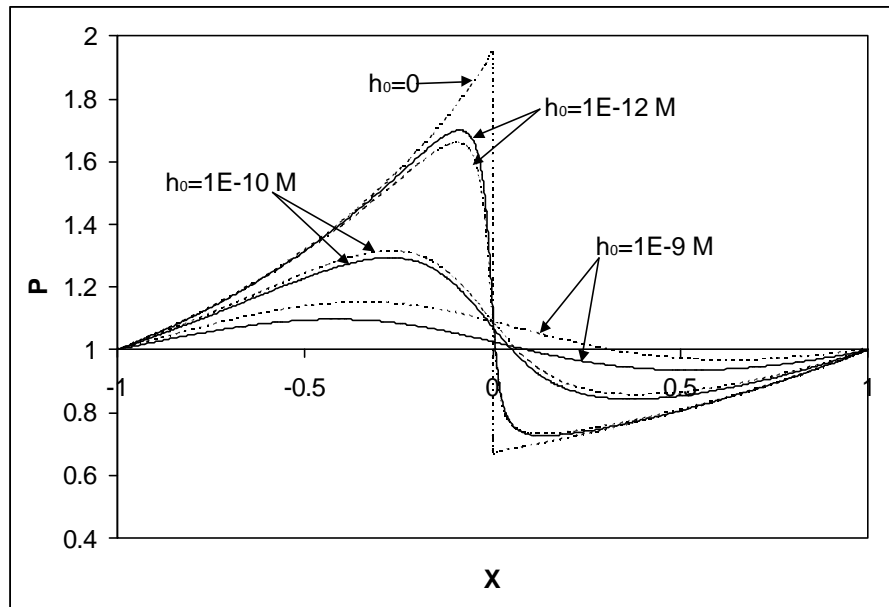
Fig. 2.3 The pressure profiles predicted by the 1.5 order slip model ($g = 8/3$) for different minimum spacing h_0; Solid line: numerical solution of full eq. (2.8); dashed line: analytical solution given by eq. (2.13) and the asymptotic curve of eq. (2.14) (when $h_0 = 0$).
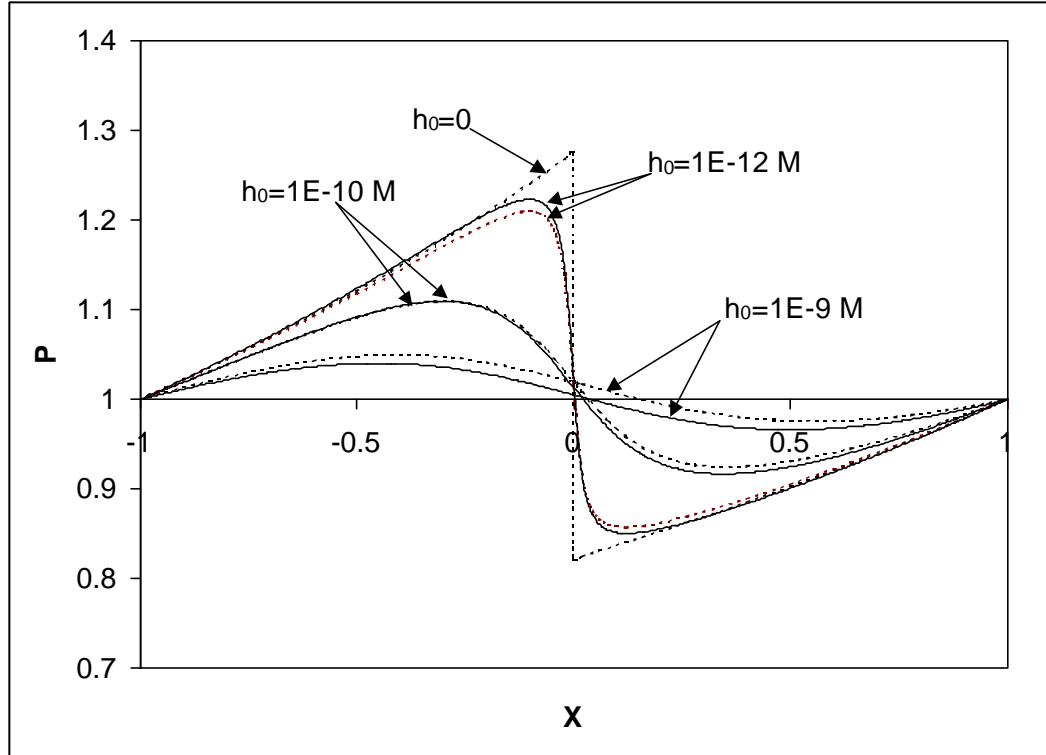
Fig. 2.4 The pressure profiles predicted by the second order slip model ($\boldsymbol{g} = 6a$) for different minimum spacing h_0; Solid line: numerical solution of full eq. (2.8); dashed line: analytical solution given by eq. (2.13) and the asymptotic curve of eq. (2.14) (when $h_0 = 0$).
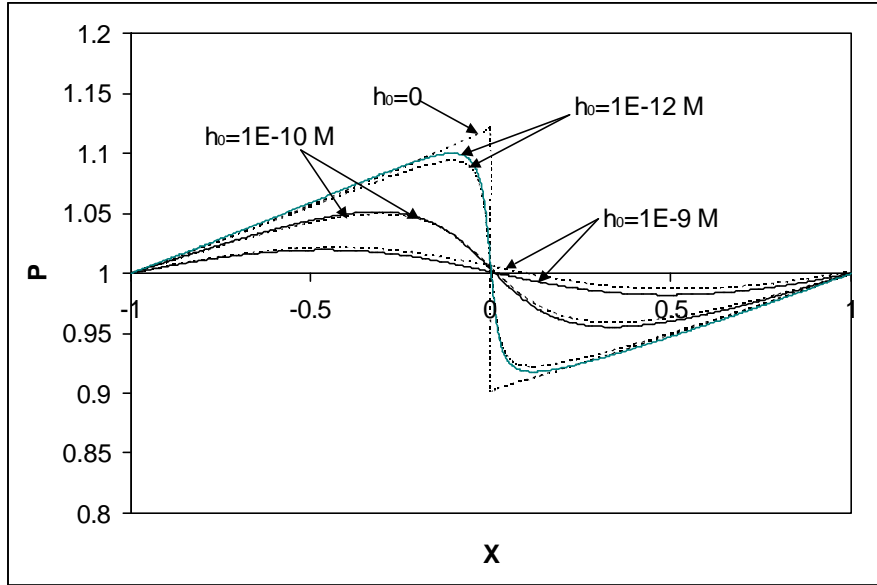
Fig. 2.5 The pressure profiles predicted by the new order slip model ($g = 12a$) for different minimum spacing h_0; Solid line: numerical solution of full eq. (2.8); dashed line: analytical solution given by eq. (2.13) and the asymptotic curve of eq. (2.14) (when $h_0 = 0$).

Fig. 2.6 The converging corner and the diverging corner around a contact area.
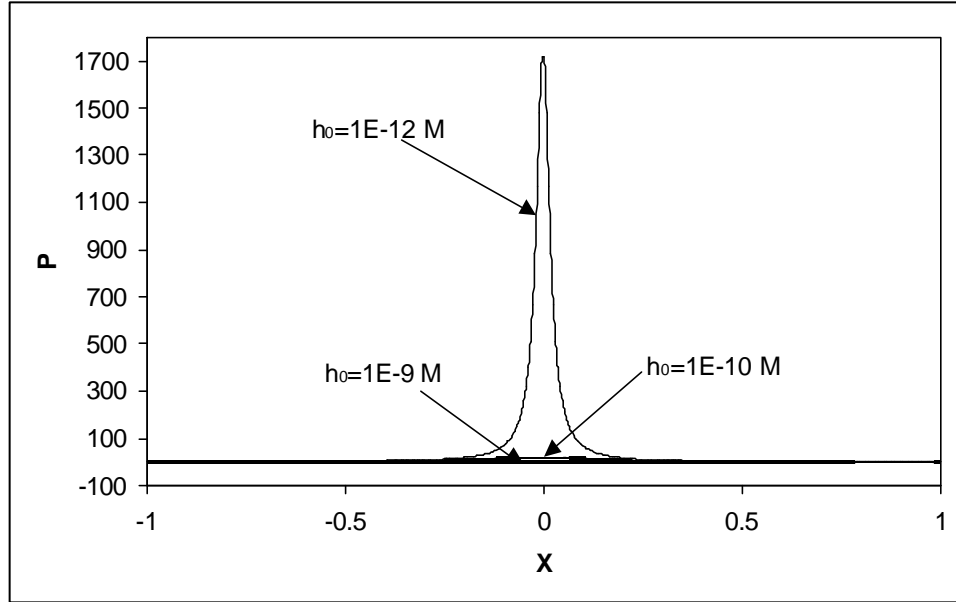
Fig. 2.7 The pressure profiles predicted by the first order slip model for different
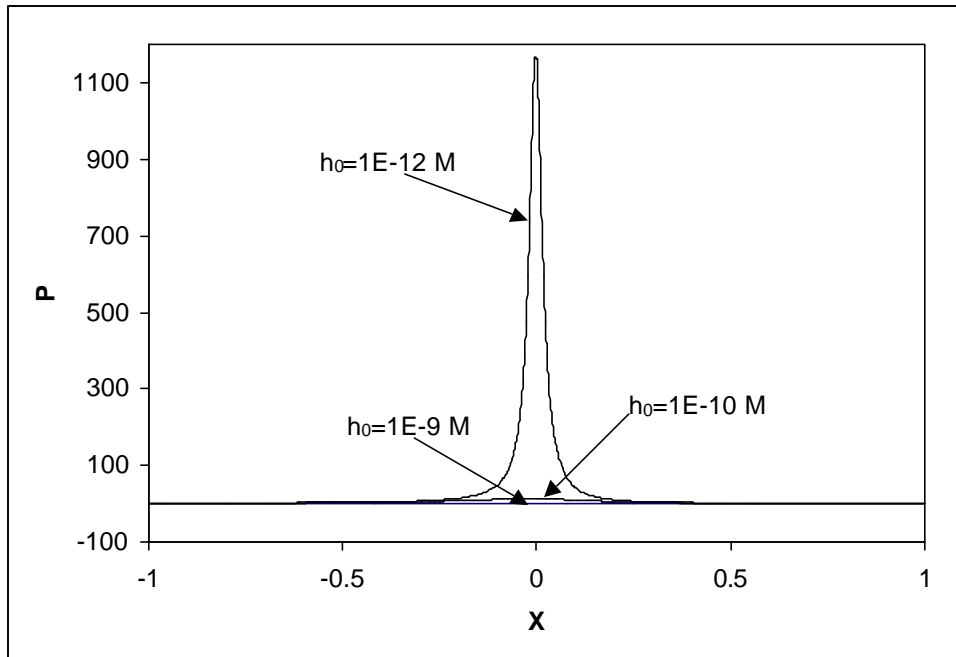
minimum spacings.

Fig. 2.8 The pressure profiles predicted by the FK model for different minimum spacings.
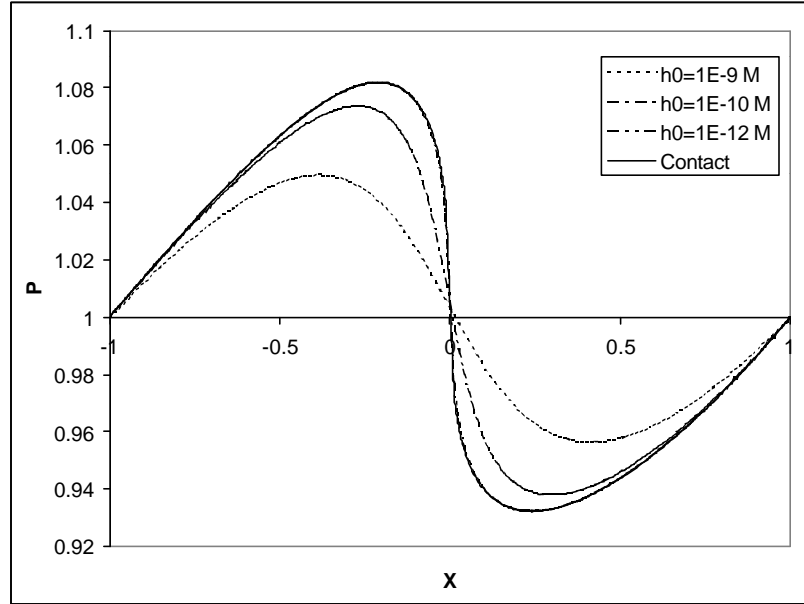
Fig. 2.9 The pressure profiles along the center line $Y = 0$ for the two dimensional problem as predicted by the second order slip model for different minimum spacings.
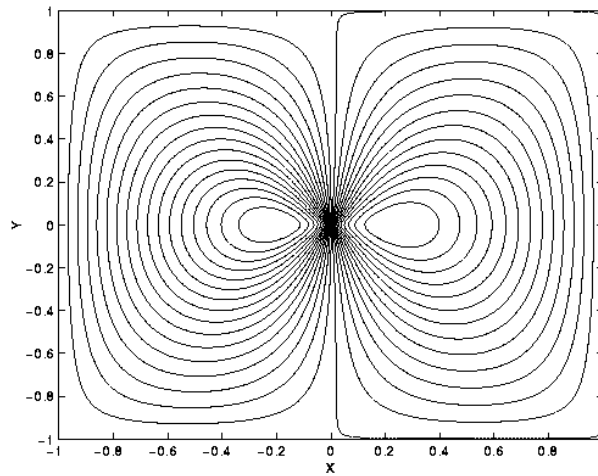
Fig. 2.10 The pressure contours for the two dimensional problem predicted by the second order slip model with contact.
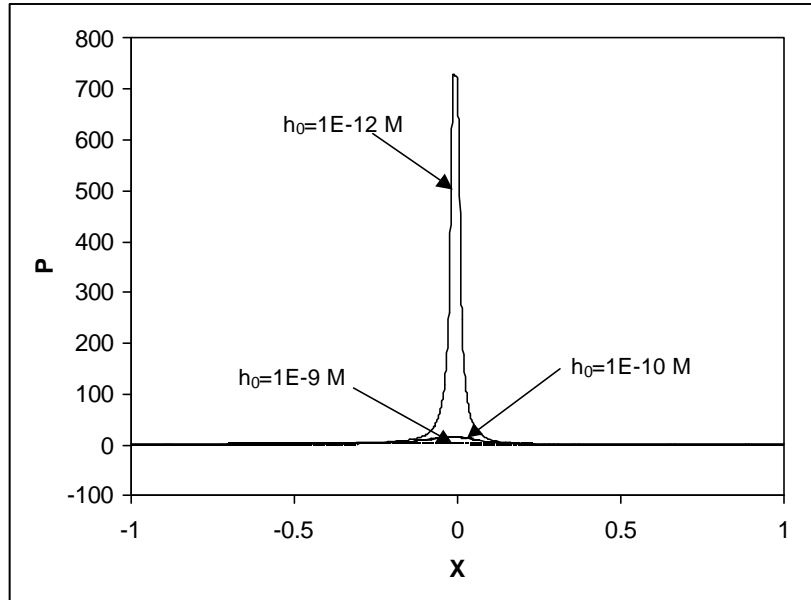
Fig. 2.11 The pressure profiles at the center line $Y = 0$ for the two dimensional problem predicted by the first order slip model for different minimum spacings.
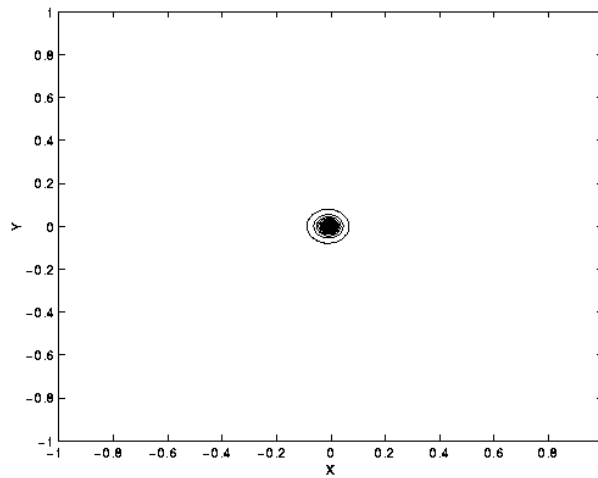
Fig. 2.12 The pressure contours for the two dimensional problem as predicted by the first order slip model with $h_0 = 1E - 12\ M$.
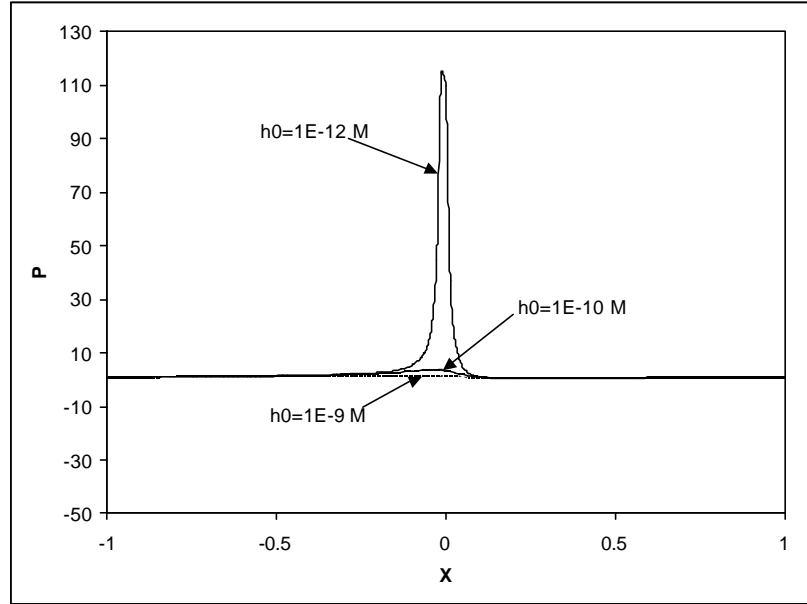
FIG. 2.13 The pressure profiles along the center line $Y = 0$ for the two dimensional problem as predicted by the FK model for different minimum spacings.
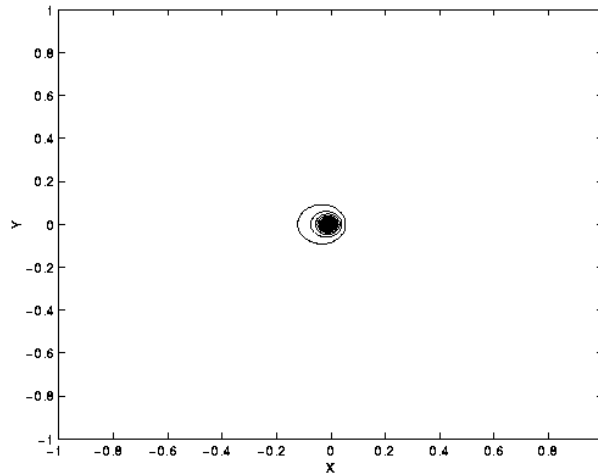
FIG. 2.14 The pressure contours for the two dimensional problem as predicted by the FK model with $h_0 = 1E - 12\,M$.

34

CHAPTER 3

A NEW DERIVATION OF THE FIRST AND SECOND ORDER SLIP MODELS

FOR THE COMPRESSIBLE REYNOLDS EQUATION

3.1 Introduction

Among all the existing models, the FK model was previously believed to give the most accurate results for large Knudsen numbers. This is shown not to be true in the previous chapter. The FK model and the first order slip model have unbounded contact pressure singularities but the second order slip model, the 1.5 order slip model and a new model derived in Chapter 2 do not have this unphysical singularity, which means the FK model can not predict the pressure correctly at very large Knudsen numbers (or at or near contact) since there is physically no unbounded contact pressure singularity. In addition, the prediction of the second order slip model and the FK model is not significantly different when the flying height of the slider is below 100 nm but away from the contact or near contact regime. Models based on slip velocity conditions at the gas-solid interface together with the continuum assumption have a much simpler form than the FK model. As a result they still have value in some actual applications.

In this chapter, we re-derive the first order and the second order slip models from a more physical point of view. The new models have similar forms to the old counterparts but with different coefficients. The new second order slip model is shown to have closer performance to the FK model, in the regime where the latter has reasonable predictions, than the old second order slip model at smaller inverse Knudsen number.

3.2 Derivation of the Slip Velocity Boundary Condition

From kinetic theory, molecules are expected to cross a small plane of area from all directions. The number of molecules that cross a plane of unit area from one side with an angle $\boldsymbol{q}$ with respect to the normal of the plane and with a solid angle $d\boldsymbol{w}$ (see Fig. 3.1) is

$$\frac{1}{4\boldsymbol{p}} n\bar{v}\cos\boldsymbol{q}d\boldsymbol{w}, \tag{3.1}$$

where n is the number density of molecules, and $\bar{v}$ is the mean molecular speed (Kennard, 1938). The solid angle element $d\boldsymbol{w}$ is defined as

$$d\boldsymbol{w} = \sin\boldsymbol{q}d\boldsymbol{q}d\boldsymbol{j} , \tag{3.2}$$

where $\boldsymbol{j}$ is the azimuthal angle. Assume a shear flow (the bulk gas velocity is parallel to the plane), then the momentum transfer rate across the unit plane by molecules with a trajectory making an angle $\boldsymbol{q}$ with the normal of the plane from both sides is

$$d\boldsymbol{t} = \frac{1}{4\boldsymbol{p}} mn\bar{v}\cos\boldsymbol{q}d\boldsymbol{w}\left(u(z+l_z)-u(z-l_z)\right), \tag{3.3}$$

where m is the molecule mass, and $u(z+l_z)$ and $u(z-l_z)$ are gas velocities at $z+l_z$ and $z-l_z$, respectively. Here we assume the gas molecules maintain the same bulk velocity as the point $\boldsymbol{l}$ (mean free path) away from the collision point at the plane along their traveling direction (see Fig. 3.1). This is justified, because the change of the bulk

36

velocity can only be achieved through collisions with other molecules or boundaries. As a result, we have $l_z = l\cos q$. As usual, the bulk velocities at $z + l_z$ and $z - l_z$ are approximated by a Taylor series as

$$u(z + l_z) = u(z) + l_z \frac{\partial u}{\partial z} + \frac{l_z^2}{2} \frac{\partial^2 u}{\partial z^2},$$

$$u(z - l_z) = u(z) - l_z \frac{\partial u}{\partial z} + \frac{l_z^2}{2} \frac{\partial^2 u}{\partial z^2}. \tag{3.4}$$

Substituting l_z and eq. (3.4) into eq. (3.3), we obtain

$$d\boldsymbol{t} = \frac{1}{4\boldsymbol{p}} mn\overline{v} \cos\boldsymbol{q} d\boldsymbol{w} \left(2\boldsymbol{l} \cos\boldsymbol{q} \frac{\partial u}{\partial z} \right). \tag{3.5}$$

Integrating the above equation over the half sphere, we obtain the momentum transfer rate across the unit area plane by molecules from both sides

$$\boldsymbol{t} = \frac{1}{2\boldsymbol{p}} mn\overline{v}\boldsymbol{l} \frac{\partial u}{\partial z} \int_0^{2\boldsymbol{p}} \int_0^{\frac{\boldsymbol{p}}{2}} \cos^2\boldsymbol{q} \sin\boldsymbol{q} d\boldsymbol{q} d\boldsymbol{j} = \frac{1}{3} mn\overline{v}\boldsymbol{l} \frac{\partial u}{\partial z}. \tag{3.6}$$

On the other hand the shear stress from the macroscopic, or continuum, point of view is

$$\boldsymbol{t} = \boldsymbol{m} \frac{\partial u}{\partial z}. \tag{3.7}$$

Equating (3.6) and (3.7), the dynamic viscosity of the gas is found to be

$$\boldsymbol{m} = \frac{1}{3} mn\overline{v}\boldsymbol{l}. \tag{3.8}$$

37

Similarly, the momentum transfer rate at the gas-solid interface by molecules with an angle q between their velocity and the normal of the interface and with a solid angle element dw can be written as

$$dt = \frac{1}{4p} amn\bar{v} \cos q \, dw \left(u(l_z) - u_{plate} \right)$$
$$= \frac{1}{4p} mn\bar{v} \cos q \, dw \left(u_{slip} + l_z \frac{\partial u}{\partial z}\bigg|_{z=0} + \frac{l_z^2}{2} \frac{\partial^2 u}{\partial z^2}\bigg|_{z=0} \right), \quad (3.9)$$

where a is the accommodation coefficient. Integrate eq. (3.9) over the half sphere, and then the momentum transfer rate at the gas-solid interface can be written as

$$t = \frac{1}{4p} amn\bar{v} \int_0^{2p} \int_0^{\frac{p}{2}} \left[\begin{array}{c} u_{slip} \cos q \sin q + l \frac{\partial u}{\partial z} \cos^2 q \sin q \\ + \frac{l^2}{2} \frac{\partial^2 u}{\partial z^2} \cos^3 q \sin q \end{array} \right] dq \, dj$$
$$= \frac{1}{4} amn\bar{v} \left(u_{slip} + \frac{2}{3} l \frac{\partial u}{\partial z} + \frac{l^2}{4} \frac{\partial^2 u}{\partial z^2} \right). \quad (3.10)$$

The second order slip velocity of the gas molecules at the interface is obtained then by equating (3.7) and (3.10) to get

$$u_{slip} = \frac{2}{3} \left(\frac{2-a}{a} \right) l \frac{\partial u}{\partial z} - \frac{l^2}{4} \frac{\partial^2 u}{\partial z^2}. \quad (3.11\ a)$$

The first order slip velocity is obtainded by dropping the second order derivative term

$$u_{slip} = \frac{2}{3}\left(\frac{2-a}{a}\right)l\,\frac{\partial u}{\partial z}.$$

<div align="right">(3.11 b)</div>

3.3 Derivation of a First Order and a Second Order Slip Lubrication Equations

Under lubrication conditions, the Navier-Stokes equation can be simplified to

$$\frac{\partial}{\partial x}(ru) = 0\ ,$$

$$0 = -\frac{\partial p}{\partial x} + m\frac{\partial^2 u}{\partial z^2}\ ,$$

$$\frac{\partial p}{\partial z} = 0.$$

<div align="right">(3.12)</div>

The velocity distribution within the gas layer for a second order slip model is

$$u = \frac{1}{2m\partial x}\frac{\partial p}{\partial x}\left[z^2 - hz - \left(\frac{2}{3}al\right)h - \frac{l^2}{2}\right] + U\left[1 - \frac{z + \left(\frac{2}{3}al\right)}{h + 2\left(\frac{2}{3}al\right)}\right],$$

<div align="right">(3.13)</div>

which is obtained by integrating eq. (3.12) subject to the two slip velocity boundary conditions at the two gas-solid interfaces

$$u\Big|_{z=0} = U + \frac{2}{3}al\frac{\partial u}{\partial z}\Big|_{z=0} - \frac{1}{4}l^2\frac{\partial^2 u}{\partial z^2}\Big|_{z=0},$$

<div align="center">39</div>

$$u\big|_{z=h} = -\frac{2}{3}a\boldsymbol{l}\frac{\partial u}{\partial z}\bigg|_{z=h} - \frac{1}{4}\boldsymbol{l}^2\frac{\partial^2 u}{\partial z^2}\bigg|_{z=h}, \tag{3.14 a}$$

where h is the clearance spacing, and a is the surface correction coefficient. The mass

flow rate at each cross section is obtained by integrating eq. (3.13)

$$q = \boldsymbol{r}\int_0^h u\,dz = -\frac{\boldsymbol{r}}{2\boldsymbol{m}}\frac{\partial p}{\partial x}\left[\frac{h^3}{6} + \left(\frac{2}{3}a\boldsymbol{l}\right)h^2 + \left(\frac{\boldsymbol{l}^2}{2}\right)h\right]. \tag{3.15}$$

The dimensionless flow rate for the second order slip model can be written as

$$Q_p = -\frac{q}{h^2\dfrac{\partial p}{\partial x}\dfrac{1}{\sqrt{2RT_0}}} = \frac{D}{6} + \left(\frac{2}{3}\right)\frac{\sqrt{\boldsymbol{p}}}{2}a + \left(\frac{1}{2}\right)\frac{\boldsymbol{p}}{4}\frac{1}{D}, \tag{3.16}$$

where the modified inverse Knudsen number D is defined as

$$D = \frac{\sqrt{\boldsymbol{p}}}{2}\frac{1}{K_n} = \frac{\sqrt{\boldsymbol{p}}}{2}\frac{h}{\boldsymbol{l}}. \tag{3.17}$$

Similar analysis can be carried out for the first order slip model by using the first

order slip velocity condition (3.11b). For the first order slip model,

$$Q_p = \frac{D}{6} + \left(\frac{2}{3}\right)\frac{\sqrt{\boldsymbol{p}}}{2}a. \tag{3.18}$$

40

The compressible Reynolds equation then follows from substituting the velocities into and integrating the continuity equation. After using the assumptions that the gas is ideal and the gas layer is isothermal, we obtain a new second order slip lubrication equation

$$\frac{\partial}{\partial X}\left[\left(PH^3 + \boldsymbol{b}K_n H^2 + \boldsymbol{g}K_n^2 \frac{H}{P}\right)\frac{\partial P}{\partial X}\right] = \Lambda_x \frac{\partial}{\partial X}(PH).$$
(3.19)

In the above equation, P and H are the dimesionless pressure and spacing between the upper and lower surfaces, normalized by the ambient pressure p_a and the smallest spacing h_0, respectively. $\Lambda_x = 6\boldsymbol{m}UL/p_a h_0^2$ and $\Lambda_y = 6\boldsymbol{m}VL/p_a h_0^2$ are the bearing numbers in the x and y directions, respectively, which represent the relative importance between the convection effect and the diffusion effect. L is the horizontal length scale. X and Y are dimensionless coordinates normalized by L. $\boldsymbol{b}$ and $\boldsymbol{g}$ are two model constants, which for the new second order slip model, are $\boldsymbol{b} = 4a$ and $\boldsymbol{g} = 3$.

Similarly, a new first order slip lubrication equation with $\boldsymbol{b} = 4a$ and $\boldsymbol{g} = 0$ is obtained by dropping the higher order term. Other slip models are also represented by the same equation with different values of $\boldsymbol{b}$ and $\boldsymbol{g}$. The $\boldsymbol{b}$ and $\boldsymbol{g}$ for some of the known models are listed in Table 3.1.

3.4 Discussion

To compare the performance of the newly derived second order slip lubrication equation with other models, we first plot in Fig. 3.2 the dimensionless flow rates of the

different models as a function of the modified inverse Knudsen number. For the continuum model, $Q_p = D/6$, which is a straight line in the figure. The data for the FK model is taken from Fukui and Kaneko's (1990) database. For the first order slip model $Q_p = D/6 + \sqrt{p}a/2$. It gives a lower flow rate than the FK model. The old second order slip model gives, $Q_p = D/6 + \sqrt{p}a/2 + p/(4D)$, which gives a larger flow rate than the FK model. $Q_p = D/6 + \sqrt{p}a/2 + p/(9D)$ is for the 1.5 order slip model. Finally eq. (3.16) gives the flow rate of the newly derived second order slip model and eq. (3.18) gives the flow rate of the new first order slip model. The figure shows the new second order slip model gives a flow rate slightly smaller than the FK model when the modified inverse Knudsen number is larger than 1, and it predicts a larger flow rate when the modified inverse Knudsen number is smaller than 0.1. The flow rate of the new second order slip model is closer to that of the FK model than the old second order slip model when the inverse Knudsen number is small.

Figure 3.3 shows the geometry of a two dimensional flat faced slider, with a fixed ratio $h_1/h_2 = 2$, and with the bearing number $\Lambda_x = 10$. Figure 3.4 shows the normalized load capacity of the flat faced slider as a function of the ambient modified inverse Knudsen number $D_0 = \sqrt{p}h_1/(2l_0)$. The load is normalized by the ambient pressure and the length of the slider L. From the figure, we see that the first order slip model over predicts the load and the old second order slip model underpredicts the load, compared with the prediction of the FK model. The new first order slip model predicts a higher load than the old first order slip model. The new second order slip model predicts a slightly higher load than the FK model when the modified inverse Knudsen number is

larger than 1 and predicts a smaller load when the modified inverse Knudsen number is smaller than 0.1. But the new second order slip model gives a closer prediction to the FK model than the old second order slip model at small modified inverse Knudsen numbers.

Since $g = 3$ in the new second order slip model, it follows from the results of the previous chapter, that the new second order slip model also does not have an unbounded contact pressure singularity. As explained previously the new first order slip model still has an unbounded contact pressure singularity.

3.5 Conclusions

New first order and second order slip model lubrication equations are derived from a more physical point of view, in which we do not assume that the length scale in the Taylor expansion of the bulk velocity is equal to the mean free path. In this sense, the derivation is free of any arbitrarily chosen value. The newly derived lubrication equations have forms similar to the old first order and the second order slip models, but the new second order slip model predicts results closer to the FK model when the modified inverse Knudsen number is small. The new second order slip model equation does not suffer from the pressure singularity of the FK model at contact.

Table 3.1 The model coefficients b and g for some modified Reynolds equation.

Models	b	g
1st order slip model	$6a$	0
2nd order slip model	$6a$	$6a$
1.5 order slip model	$6a$	$8/3$
Model in Ch. 2	$6a$	$12a$
New 1st order slip model	$4a$	0
New 2nd order slip model	$4a$	3
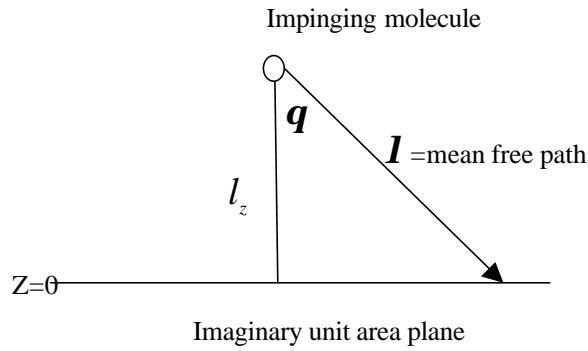
Fig.3.1 A molecule crosses an imaginary plane.
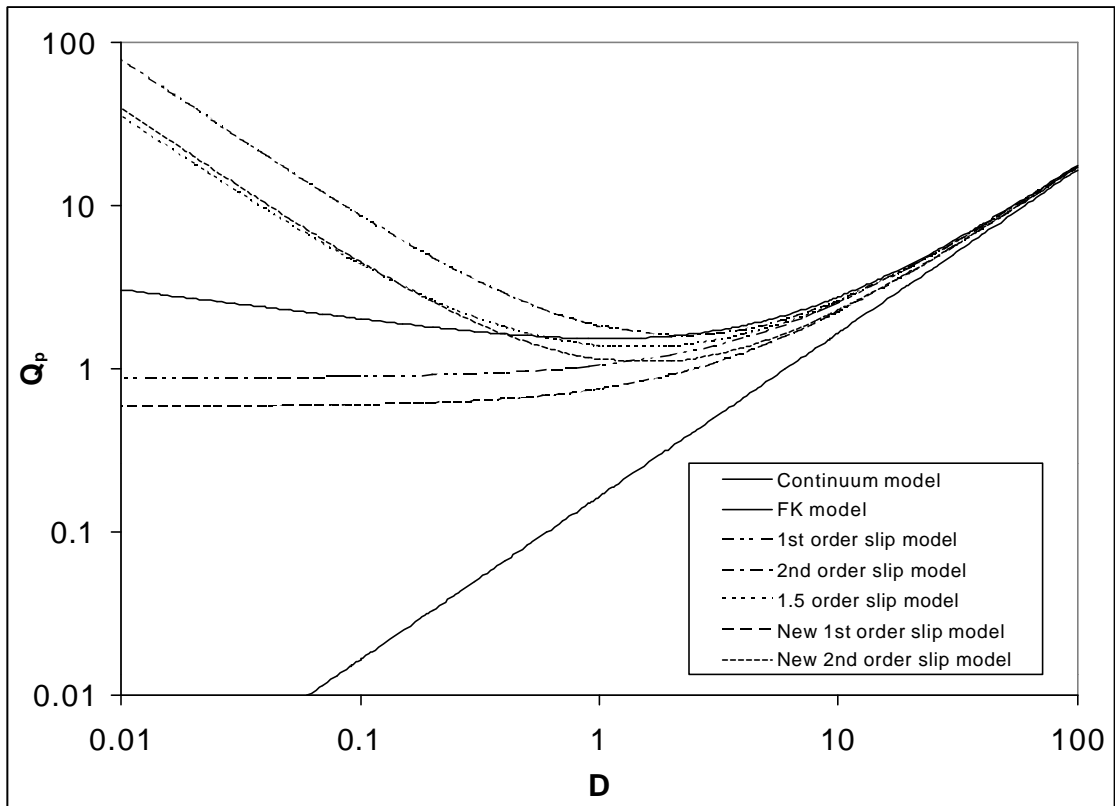
Fig. 3.2 The comparison of the dimensionless flow rate.
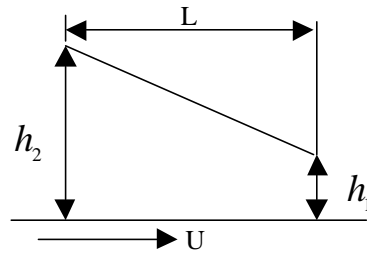
Fig. 3.3 The geometry of a flat faced 2-dimensional slider.
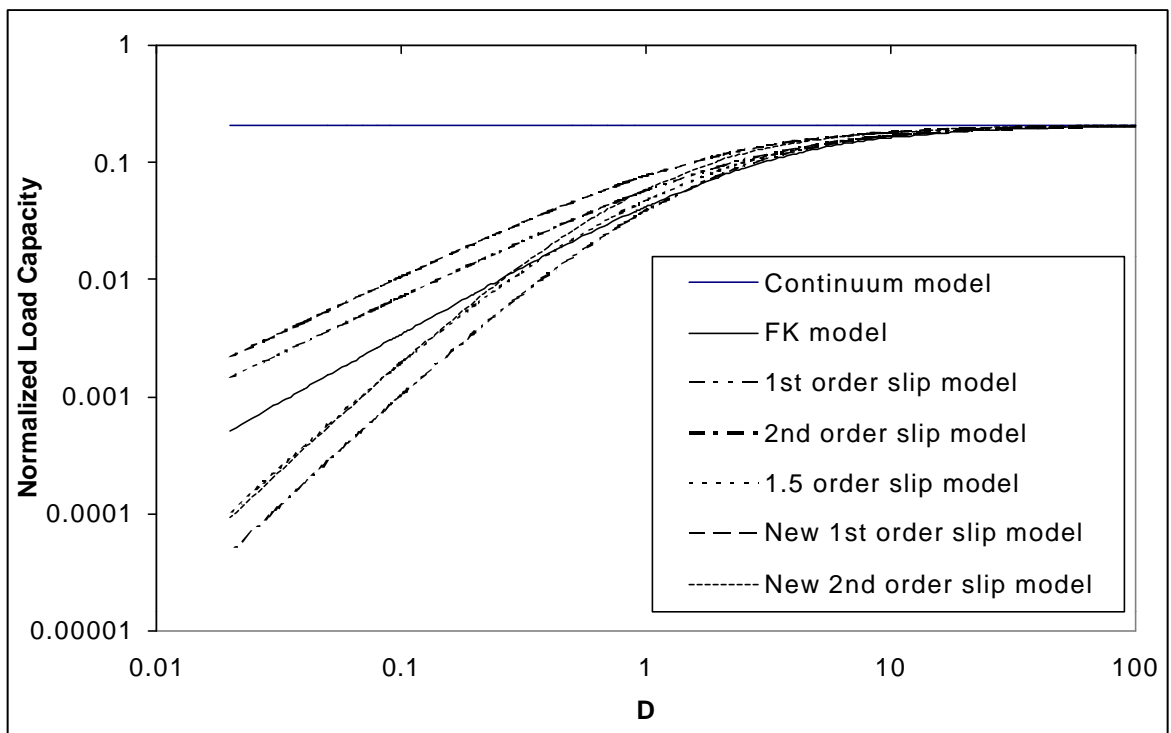
Fig. 3.4 The comparison of the normalized load capacity.

CHAPTER 4

UNSTRUCTURED ADAPTIVE TRIANGULAR MESH GENERATION TECHNIQUES AND FINITE VOLUME SCHEMES

4.1 Introduction

To increase the storage capacity of the hard disk drives, the sliders must fly lower with rail shapes that are becoming increasingly complicated, imposing a great challenge to the numerical simulation. To meet an increasing need, unstructured triangular mesh generation techniques and numerical schemes that are suitable for the air bearing simulation of complicated shapes have been recently developed in CML.

Current sliders in hard disk drives are characterized by complicated rail shapes and highly recessed air bearing regions between the rails. The rails are joined to the fully recessed regions by abruptly changing wall profiles determined by the etching process. According to previous investigations, in addition to having enough mesh in high pressure gradient regions, an accurately specified wall profile is also necessary for getting accurate numerical results, which requires the clustering of very fine meshes in the narrow recess wall regions. When the rail boundary is curved or not aligned with the coordinate axes, and a Cartesian rectangular mesh system is used, it is extremely difficult to achieve the above goals without refining the mesh in other regions where a fine mesh is not needed. This normally causes the mesh number to become much too large for efficient numerical simulation, since the CPU time needed to get converged results increases very rapidly with the total grid number.

A properly chosen grid system and its corresponding generation technique are as important in the numerical simulations as the numerical scheme itself. A good grid generator must be efficient and convenient to use. At the same time, it must give the user enough flexibility and control such that reasonably distributed meshes with the desired quality can be generated for each specific problem.

Because of its geometric flexibility in constructing a quality mesh around complex configurations and relative convenience in incorporating an adaptive methodology, the triangular unstructured mesh has become popular in recent years in many applications. Two major techniques have been used to generate unstructured triangular meshes in the CFD field. One is the advancing front method (Lo 1985). In this method, new triangles are formed from the front advancing away from domain boundaries. The advantage of this approach lies in its robustness and relative ease of application. Compared with other triangulation procedures like Delaunay triangulation, this method suffers the shortcoming that it is less efficient and permits limited control over the quality of the generated triangles. The second one is the Delaunay method, as will be fully described later. Due to its efficiency and its ability to generate optimal connections of the existing node points, say maximizing the minimum angle of each triangle, the Delaunay method is used as a building block in our approach. Here we use two different techniques to generate the Delaunay triangulation. One is the Bowyer-Watson algorithm (Bowyer 1981 and Watson 1981), the other is Sloan's algorithm (1987). Traditionally, all node points are generated by a certain means before they are connected into triangles using the above algorithms. Then one by one, these nodes are inserted into the existing triangulation. But before the insertion, a search is needed to locate the triangle that encloses the new node. When the

number of nodes is large, the efficiency of the above algorithms is greatly reduced due to the searching process. Rebay (1993) proposed an incremental approach, in which the locations of new nodes are simultaneously decided by a local property of the previous triangulation as new connections are formed, instead of being decided before the triangulation. This eliminates the need to do the search. We adopt Rebay's incremental ideas in our approach.

In our simulation process a multi-grid technique is used to achieve fast convergence. As a result, we need several levels of meshes ranging from very fine to very coarse. We use three different grid refinement and adaptation techniques to generate these levels of grids. To ensure accuracy and efficiency of the following simulations, each of them will capture either one geometrical or one physical characteristic of the problem. At the coarsest level it's important that the boundaries of the rail be fully defined by triangle sides in the triangulation. Otherwise, the represented geometry can be easily distorted far away from the actual one, which may cause detrimental effects on the following multi-gird iteration process. If the geometry represented by the coarsest grids is quite different from that represented by the finer grids, the iteration on the coarsest mesh may converge to a quite different solution from that of the finer meshes. A conforming Delaunay refinement technique in Ruppert (1995) is adopted to generate the conformed coarsest mesh. At the second level of grids, with more grids available, it's possible to specify the wall profile to some extent. The longest-side-bisection Delaunay refinement technique in Rivara *et.al*. (1997) is adopted so that a high quality fine mesh can be clustered in the recess wall region based on geometrical considerations. In the air bearing field, the majority region with smoothly changing pressure is surrounded by small regions with

extremely high-pressure gradients. Global grid refinement is definitely not a good choice, since enormous amounts of computer resources will be wasted in regions with smoothly changing pressure profiles where high grid resolution is not needed. In such a situation, the grid adaptation technique has proved to be an efficient way to improve the accuracy of simulation at a much lower cost than that of the global grid refinement strategy. An adaptive mesh refinement technique, which uses the undivided pressure difference as the sensor, is developed to refine a good quality mesh in the high-pressure gradient regions during the simulation process, which gives the finest grid.

In recent years extensive effort has been devoted to the simulation of slider air bearings of hard disk drives with complex rail shapes. Most numerical methods fall into one of three categories: finite difference methods, finite volume methods (also called control volume methods) and finite element methods. All of them have been used in air bearing simulations (White *et al.,* 1980, Lu 1997 and Garcia-Suarez *et al.,* 1984). The finite difference method is known for its efficiency if smooth and adequate meshes can be generated. When the geometry is complicated, generally a body-fitted mesh system that can smoothly follow the boundaries is generated by either solving a PDE (Thompson *et al.,* 1977) or simply using algebraic interpolation. A coordinate transformation is carried out to transform the curvilinear meshes in the physical domain into the equally spaced rectangular mesh in the computational domain. But in the air-bearing field, in most cases, only Cartesian rectangular mesh systems have been used, so the potential of the finite difference method has not been fully explored. When the geometry is very complicated, generating good structured meshes becomes extremely difficult, and the finite volume and finite element methods are preferred. Both the finite volume and finite element

method are integral methods that can be implemented in the physical domain without the need of coordinate transformation, and unstructured meshes can be used, which makes the mesh generation much easier and more flexible. Due to their local conservative quality, the finite volume methods are good at capturing sharp gradients, which, in the air bearing simulation, are unavoidable. Therefore the finite volume method is used in our approach.

Both explicit and implicit finite volume schemes have been constructed to locally integrate the general Reynolds equation over the control volumes that are taken to be the dual Voronoi polygons of the triangles (see Fig. 4.1). The pressure is stored at the nodes. The property that each edge of the Voronoi polygon is a perpendicular bisector of the triangle edge that connects its generation point and the generating point of the adjacent Voronoi polygon makes it possible to use Patankar's strategy (1980) to evaluate the numerical flux across the edges of the control volume. Backward differencing is used to discretize the unsteady term resulting in first order accuracy in time. The solution is evolved by marching in time until the steady state is reached. For steady state problems, the unsteady term is not needed physically, but it is kept here to serve as an under-relaxation term. When a relatively large time step is used, the unsteady term can be ignored, and the technique is more like a direct iteration than time marching. The Gauss-Seidel iteration technique is used to solve the linear algebraic equations. The implicit scheme is unconditionally stable, so an arbitrarily large CFL number (dimensionless time step) such as 1.0E12 (used in the following simulations) can be used.

This approach also has its disadvantages. Due to its unstructured nature, additional information about connectivity between meshes must be stored, and a complicated data

structure must be set up and used to locate the needed information. This indirect addressing results in increased computational time and memory. Most mature and well-tested numerical algorithms developed for structured mesh systems can no longer be used or at least require modification. Solvers over unstructured meshes are more complicated than their structured counterparts. Historically, solvers based on unstructured meshes were less efficient. However, after several years of development, implicit time stepping and multi-grid techniques have been successfully developed and implemented in unstructured solvers to the point where both their accuracy and efficiency can compete with their structured counterparts. Most importantly, compared with a rectangular Cartesian mesh, much fewer meshes are needed, and it is well known that the computational time increases quickly with increased mesh number.

4.2 Delaunay Triangulation and Its Dual Voronoi Regions

In 1850, Dirichlet proposed a way to divide a domain into a series of non-overlapping convex polygons. These polygons are called Voronoi regions. Each Voronoi region is associated with a generating point. A Voronoi region is defined as the set of points that are closer to their own generating point than to the generating point of any other Voronoi region (see Fig. 4.1). The Delaunay triangulation is formed by connecting the generating points of neighboring Voronoi regions. From the definition of the Voronoi regions and their dual Delaunay triangulation, it can be seen, in two dimensions, that each vertex of a Voronoi polygon is the center of the circumscribing circle of one of the triangles. Each edge of the triangle is perpendicularly bisected by an edge of two Voronoi polygons, with

the two end points of the triangle edge being the generating points of the two neighboring Voronoi regions. The circumscribing circle of each triangle does not include any other triangle nodes. This last local quality of the Delaunay triangulation forms the basis for the different Delaunay triangulation algorithms.

4.3 Bowyer-Watson Algorithm for Two Dimensional Problems

In this algorithm (Bowyer 1981 and Watson 1981), new nodes are sequentially introduced into the previous triangulation. The triangle that encloses a new node is first located, then starting from this triangle, a local search is conducted to find all the triangles of the previous triangulation that violate the Delaunay circle test, which is used to check if the circumcircle of a certain triangle encloses the new node. Then all triangles violating the test are agglomerated into a cavity. These triangles are deleted from the list and new triangles are formed by connecting the new node with each edge of the cavity. The procedure continues until all the nodes have been inserted into the domain. This algorithm is known for its simplicity and readiness to be extended to three dimensional problems.

4.4 Sloan Algorithm

Sloan's algorithm (1987) is a swapping process that works fast for two dimensional problems. In this scheme, when a new node is introduced into the domain, three new triangles are formed first by connecting the new node to the three vertices of the triangle that enclose it, then the old triangle is deleted. The net increase of the number of triangles is two. All adjacent triangles that share the edges opposite to the new node are placed in a "last-in-first-out" stack (initially with three triangles in it). The algorithm is: pop up the last triangle in the stack, check if the new node is outside the circumcircle of the triangle, if not, Lawson's swapping scheme (1977) is executed. The diagonal of the quadrilateral formed by the popped up triangle and the adjacent one that contains the new node is replaced by the other diagonal that includes the new node, or in other words, the two old triangles are replace by two new triangles with the minimum angle being maximized. After this, place all the triangles that are opposite the new node into the stack. The process continues until the stack runs out of triangles.

4.5 Conforming Background Mesh Generation

It is desirable for the boundary lines of the rails to coincide with triangle sides in the triangulation of the coarsest mesh. Our approach is based on Ruppert's scheme (1995). First, a series of binary search trees (see Fig. 4.2) are constructed with the first elements being lines that form the boundary of the rail, or the line of the taper, or the boundary of

the slider. To avoid certain confusing situations in the following encroachment test, one must take care to insure there is no overlapping between these 'mother' lines. Overlapping will happen when the rails touch the boundary of the slider. In that case, the two partly or completely overlapping lines are replaced by subsidiary lines that do not overlap. In most cases, the slider's shape is rectangular, so the whole domain can be initially divided into two triangles. If the slider's shape is not rectangular, the domain can be divided into more triangles. The list of triangles (initially with two triangles) is first expanded by inserting the vertices of the rail polygons into the domain using either the Bowyer-Watson algorithm or the Sloan algorithm. After that, starting from the beginning of the list, we check if the longest side of the triangle is smaller than a prescribed tolerance or if the aspect ratio of the triangle is larger than a prescribed value. The aspect ratio is defined as the ratio between the longest and the shortest sides of the triangle. If the answer is no, we move to the next triangle in the list. Otherwise, we calculate the location of a new node at the center of the circumscribing circle of the triangle. A search is conducted to see if any 'mother' or 'child' of the search tree list, which does not have any further 'children', is encroached by the node at the center of the circumscribing circle. A line is said to be encroached when the new node lies within the diametral circle of the line. If the answer is no, the location of the new node is final. Otherwise, we divide the encroached line at the middle to form two 'children' and put them under the new 'mother' in the search tree. Then we modify the location of the new node from the circumscribing circle center of the triangle to the middle of the new 'mother'. Finally, we insert the new node into the domain using the above algorithms. Newly formed triangles are put at the end of the list, while triangles not in the

triangulation any more are deleted from the list. The process is continued until the end of the triangle list is reached or the number of triangles has reached a prescribed value.

The above procedure gives the users great flexibility in controlling the quality and the distribution of the grids by choosing the following three parameters. The first one is the allowable minimum of the triangle's longest side, which controls the coarseness of the grids. It is beneficial to specify different minimum tolerances for the rail region and recessed region, because normally, the pressure profile in the rail region changes more rapidly than that in the recessed region. Consequently, a finer mesh is needed in the rail region. The second one is the aspect ratio of the triangles, which controls the quality of the grids. The last one is the maximum allowable number of triangles.

4.6 Clustering of Meshes to the Recess Wall Regions

As stated at the beginning, accurate simulation requires a fine mesh in the recess wall region. At the same time, the quality of the mesh must be maintained. Although, the Delaunay triangulation gives optimal connections, if the nodes are not properly positioned, the generated mesh still can be highly distorted. To make things worse, bad quality triangles tend to form local clusters. A highly skewed and distorted mesh may cause severe problems in the simulation, such as slowing down the convergence, destabilizing the code or deteriorating the result. The mixed longest-side-bisection and Delaunay technique of Rivara *et al* (1997) is essentially a method that combines the node placement strategy of the longest-side-bisection technique (Rivara 1997) with the Delaunay node insertion technique. The propagating node placement strategy of the

longest-side-bisection technique gives the advantage of smoothly distributed nodes with a linear cost. The Delaunay technique gives the optimal connections of these nodes. When they are coupled together, satisfactory results can be obtained. Although the pure longest-side-bisection technique is faster than the mixed technique, it is worthwhile to sacrifice a certain amount of computer resource to the quality of the mesh.

To cluster a fine mesh in the recess wall region, starting from the first triangle in the triangle list, we conduct a test to see if the maximum recess height difference between any pair of nodes is greater than a prescribed value. If the answer is no, we move to the next triangle in the list, otherwise we find the longest side of the triangle and put its middle point into a last-in-first-out stack. Then we check to see if the longest side is also the longest side of the neighboring triangle. If the answer is no, then we set the neighboring triangle as the current triangle. We find the longest side of the current triangle and insert its middle point into the stack, and then another check is conducted. The check-insert process continues until the longest side of the current triangle is also the longest side of its neighboring triangle. When this is done, we check each of the triangles that share one of the vertices of the longest side of the original triangle from the list to see if its longest side is longer than the longest side of the triangle from the list, multiplied by a prescribed constant. If that is true, we insert the middle point of the longest side of this triangle into the stack. After this, all the points in the stack are inserted into the domain using either the Bowyer-Watson algorithm or the Sloan algorithm. New triangles are again put at the end of the list, and triangles no longer in the triangulation are deleted from the list. The refinement process stops when either the end of the list is reached (in

this case, we say the process has converged) or the total number of triangles has reached a prescribed value.

By changing the allowable maximum value of the recess height difference in each triangle, we can easily control, on the average, how many node points are needed across the narrow recess wall region. For example, when the dimensionless difference between the recess height of the rail and the fully recessed region is 1, if we choose the allowable value to be 0.33, then, when the refinement process converges, at least three nodes appear across the recess wall.

4.7 Grid Adaptation

Except for the regions with dramatic geometric changes (which have been captured by the above refinement algorithms), for sliders with a complex rail system it is difficult to decide in advance the location of the regions with high-pressure gradients, where high grid resolution is needed. A grid adaptation technique proves to be an economical way to improve the accuracy and efficiency of numerical simulation in such situations. Grid adaptation techniques generally fall into two categories; the r-refinement and the h-refinement methods. In the r-refinement strategy, the total number of nodes is fixed, while the locations of the nodes are gradually shifted in favor of the regions where fine meshes are needed. This is the method used in the current rectangular grid CML code. In the h-refinement strategy, the positions of the nodes do not move, instead, nodes are locally added to or deleted from the region according to the need. The method of incremental Delaunay triangulation makes the h-refinement a natural choice.

A good sensor that can detect the place where fine meshes are needed is important in grid adaptation. If the sensor is too sensitive, wide spread regions will be refined, resulting in too many nodes, which makes the adaptation meaningless. The other extreme is also not acceptable. In the air-bearing simulation, it is desirable to add fine meshes to the high-pressure gradient regions. Pressure gradient seems to be a good choice for the sensor. But adaptation is basically an iteration process, in which meshes are added or moved gradually until a certain standard is met by the sensor. Pressure gradient is a physical value, which does not change with the size of the grids when the solution is grid converged. In most cases, the gradient will increase with the refinement of the mesh. This makes the pressure gradient a poor choice as the sensor. Instead, the absolute value of the pressure difference along the edges of the triangle can be used as the sensor. To have the same absolute pressure difference, a smaller mesh size is needed in the high-pressure gradient region. When the mesh is refined, the absolute pressure difference will drop, which makes convergence possible.

Another important thing is to choose an adequate value for the sensor below which no refinement is carried out. The average value of the absolute pressure difference of all the lines, multiplied by a prescribed constant, is used in our approach.

Only one adaptation is carried out in our simulation. After enough iterations are done on the relative coarse mesh, the average value of the absolute pressure difference of all the lines is calculated. Starting from the first triangle in the triangle list, the largest absolute pressure difference of the triangle is calculated using the current pressure distribution. If the value is greater than the average value multiplied by a constant, the same mixed longest-side-bisection and Delaunay refinement process is carried out as

above. The pressure at the new nodes is taken as the mean value of the two nodes of the longest edge. The process continues until the end of the list is reached.

4.8 Laplacian Smoothing

After the generation of the mesh, a simple Laplacian type smoother is widely used to slightly reposition the location of the nodes to distribute them more smoothly throughout the domain (Mavriplis 1988). It is an iteration process. At each step, the locations of the nodes are updated as

$$x = x_{old} + \frac{\varpi}{n} \sum_{k=1}^{n} \left(x_k - x_{old} \right),$$

$$y = y_{old} + \frac{\varpi}{n} \sum_{k=1}^{n} \left(y_k - y_{old} \right),$$
$$\text{(4.1 a,b)}$$

where ϖ serves as a relaxation factor, and n is the number of the neighboring nodes. Either a fixed number iteration can be carried out or it can continue until convergence is reached. Our experience shows that a fixed number of 20 to 30 iterations will give a satisfactory result.

4.9 Governing Equations and Boundary Conditions

In air bearing simulations, the generalized Reynolds equation is solved to get the pressure field. In the derivation of the traditional Reynolds equation, many severe assumptions, based on dimensional analysis, have been made. The slider air bearing brings up additional challenging issues. Because of the extremely narrow spacing between the slider and the disk (in the order of 10 nm, which is only a fraction of the mean free path of the gas molecules), the gas in the spacing is extremely rarefied and the gas molecules near the solid surfaces no long simply adhere to them (although the non-slip condition has been under attack even in normal situations, it is much more severe here), instead they are slipping. The continuity and non-slip condition assumptions are no longer an acceptable approach to the actual physics. Until now, the modified versions of the Reynolds equation that take the rarefaction and slipping effect into account give the best results. The modification makes the equation appear more complicated, but from the numerical point of view, it also gives the equation a better numerical quality than that of the traditional Reynolds equation, since the pressure fields given by modified versions have less steep pressure profiles than those predicted by the traditional equation. The different versions of the Reynolds equation can be written in a unified dimensionless from as

$$s \frac{\partial}{\partial T}(PH) = \frac{\partial}{\partial X}\left(QPH^3 \frac{\partial P}{\partial X} - \Lambda_x PH\right) + \frac{\partial}{\partial Y}\left(QPH^3 \frac{\partial P}{\partial Y} - \Lambda_y PH\right) \qquad (4.2)$$

where $S = \dfrac{12\,\mu\omega L^2}{P_a h_m{}^2}$ is the squeeze number, which represents the relative importance

between the unsteady effect and the diffusion effect, with μ being the dynamic viscosity

of the gas, ω being the angular velocity of the disk, L being the length scale of the slider,

p_a being the ambient pressure, h_m being the flying height. $T = \omega t$ is the dimensionless

time, $X = \dfrac{x}{L}$ is the dimensionless x coordinate, $Y = \dfrac{y}{L}$ is the dimensionless y

coordinate, $P = \dfrac{p}{p_a}$ is the dimensionless pressure, $H = \dfrac{h}{h_m}$ is the dimensionless normal

distance from the disk to the slider, $\Lambda_x = \dfrac{6\mu U L}{p_a h_m{}^2}$ and $\Lambda_y = \dfrac{6\mu V L}{p_a h_m{}^2}$ are the bearing

numbers in the x and y direction, respectively, which represent the relative importance

between the convection effect and the diffusion effect. Q is the flow factor, which marks

the difference between different rarefaction models of the equation. Different Q for

different models are briefly listed below. The details can be found in Burgdorfer (1959),

Hsia *et al* (1983) and Fukui *et al* (1988).

$Q = 1,$ continuum model.

$Q = 1 + 6a\dfrac{K_n}{PH},$ first order slip model.

$Q = 1 + 4a\dfrac{K_n}{PH},$ new first order slip model.

$Q = 1 + 6a\dfrac{K_n}{PH} + 6a\left(\dfrac{K_n}{PH}\right)^2,$ second order slip model.

$Q = 1 + 4a\dfrac{K_n}{PH} + 3\left(\dfrac{K_n}{PH}\right)^2,$ new second order slip model.

$$Q = 1 + 6a\frac{K_n}{PH} + 12a\left(\frac{K_n}{PH}\right)^2, \quad \text{pressure gradient slip model.}$$

$$Q = f\left(\frac{K_n}{PH}\right) \quad \text{Fukui-Kaneko model.}$$

Where $a = \dfrac{2-a}{a}$, α is the accomodation factor, $K_n = \dfrac{l}{h_m}$ is the Knudsen number, λ is the mean free molecular path.

Along the outside boundary of the slider, the pressure is simply taken as the ambient pressure.

4.10 Explicit Finite Volume Discretization of the Governing Equation

After the computational domain has been decomposed into a series of non-overlapping conforming triangles, the Reynolds equation is locally integrated over each control volume. Generally, there are two choices for storing the dependent variables. One is to store the variables at the centroid of the triangles, where the corresponding finite volume scheme is called the cell centered scheme. The other is to store the variables at the vertices of the triangles, where the corresponding scheme is called the nodal scheme or vertex based scheme. Here we store our pressure at the triangle vertices. This is based on the consideration that the number of triangles is roughly two times the number of nodes. This can be seen from the Delaunay triangulation process. In Sloan's algorithm (1987), when a new node is introduced into the domain, the old triangle enclosing the new node

is first replaced by three new triangles with a net increase of two. In the following operation, the number of triangles is not changed. Using the same mesh, since the number of unknowns is smaller, the nodal scheme normally runs faster than the cell centered scheme. In addition, the information stored at the vertices can be more conveniently and fully used in the nodal scheme approach. We chose the Voronoi polygons as our control volumes (see Fig. 4.3). The Voronoi polygons and the triangles form dual meshes to each other.

The Reynolds equation in integral form can be written as

$$\iint_\Omega \left[s \frac{\partial}{\partial T}(PH) - \frac{\partial}{\partial X}\left(QPH^3 \frac{\partial P}{\partial X} - \Lambda_x PH \right) - \frac{\partial}{\partial Y}\left(QPH^3 \frac{\partial P}{\partial Y} - \Lambda_y PH \right) \right] d\Omega = 0.$$

(4.3)

After using the divergence theorem, we have

$$\iint_\Omega s \frac{\partial (PH)}{\partial T} d\Omega - \oint_s \left[\left(QPH^3 \frac{\partial P}{\partial X} - \Lambda_x PH \right) n_x + \left(QPH^3 \frac{\partial P}{\partial Y} - \Lambda_y PH \right) n_y \right] ds = 0,$$

(4.4)

where s is the boundary around the control volume, ds is the length of the line element, and n_x and n_y are the unit outward normal vector components in the x and y direction respectively. Define the local normal bearing number as

$$\Lambda_n = \Lambda_x n_x + \Lambda_y n_y = \frac{6\boldsymbol{mL}\left(Un_x + Vn_y\right)}{p_a h_m^{\ 2}} = \frac{6\boldsymbol{mL}U_n}{p_a h_m^{\ 2}}, \tag{4.5}$$

with $U_n = Un_x + Vn_y$ being the disk velosity component normal to the control volume boundary, and the normal outward pressure derivative along the boundary as

$$\frac{\partial P}{\partial n} = \frac{\partial P}{\partial X}n_x + \frac{\partial P}{\partial Y}n_y. \tag{4.6}$$

Then the integral equation becomes

$$\iint_\Omega \boldsymbol{s}\,\frac{\partial(PH)}{\partial T}d\Omega - \oint_s \left(QPH^3\frac{\partial P}{\partial n} - \Lambda_n PH\right)ds = 0. \tag{4.7}$$

Over the Voronoi polygon surrounding vertex i (see Fig. 4.3), the above equation can be approximated as

$$\left(A\boldsymbol{s}\,\frac{\partial(PH)}{\partial T}\right)_i - \sum_{j=1}^{M}\left(QPH^3\frac{\partial P}{\partial n} - \Lambda_n\right)_{ij}ds_j = 0, \tag{4.8}$$

where the first term is the unsteady term, A_i is the area of the control volume around vertex i and the lumped assuption (the value of the integrand at vertex i is taken to be the value all over the control volume) has been used. M is the number of sides of the Voronoi

polygon and ds_j is the length of its jth side. The expression in the bracket of the second term represents the numerical flux across the sides, which can be evaluated using the information of vertices i and j. Backward differencing is used to discretize the time derivative of the first term, resulting in first order accuracy in time,

$$\left(A\boldsymbol{s}\,\frac{\partial (PH)}{\partial T} \right)_i = A_i\boldsymbol{s}\,\frac{\left[(PH)_i^{\,n+1} - (PH)_i^{\,n} \right]}{\Delta T},$$

(4.9)

Here subscript n+1 represents the new value at time level n+1, n means the old value at time level n. The Delaunay trangulation and its dual Voronoi polygon have the quality that each side of the Voronoi polygon is a perpendicular bisector of the triangle side that connects the two adjacent generating points of the Voronoi polygon where the pressure is stored (in Fig.4.3, the line connecting vertices i and j is perpendicularly bisected by the jth side of the Voronoi polygon around i). Patankar's strategy (1980) is employed to calculate the numerical flux across each side of the control volume. The governing equation is locally taken to be steady and one dimensional with the space coordinate in the direction of the local outward unit normal vector, and the equation is linearized by freezing the coefficients with the value of the last time step. The resulting ordinary differential equation is solved to give the needed numerical flux. The final explicit discretization form of the equation can be written as

$$\frac{A_i H_i}{\Delta T}\,P_i^{\,n+1} = \sum_{j=1, j\neq i}^{M} C_{ij}\,P_j^{\,n} + \left(\frac{A_i H_i}{\Delta T} - C_i \right)P_i^{\,n},$$

(4.10 a)

66

with

$$C_{ij} = D_{ij} A(|P_{ij}|) + [[-F_{ij}, 0]], \qquad (4.10\ b)$$

$$C_i = \sum_{j=1,\ j\neq i}^{M} (C_{ij} + F_{ij}), \qquad (4.10\ c)$$

where the operator $[[a,b]]$ yields the larger of a and b. Function $A(|P|)$ can be written for

the different schemes as (Patankar 1980)

$$1 - 0.5|P|, \qquad \text{Central difference}$$

$$1, \qquad \text{Upwind}$$

$$[[0, 1 - 0.5|P|]], \qquad \text{Hybrid}$$

$$[[0, (1 - 0.1|P|)^5]], \qquad \text{Power law}$$

$$\frac{|P|}{[\exp(|P|) - 1]}, \qquad \text{Exponential}$$

and

$$D_{ij} = \frac{(QPH^3)_{ij}\, ds_j}{sl_{ij}},$$

$$F_{ij} = \frac{\Lambda_n H_{ij} ds_j}{s},$$

$$P_{ij} = \frac{F_{ij}}{D_{ij}}.$$

l_{ij} is the distance between vertices i and j. All other values with the double subscripts ij are related to the vertices i and j.

Equation 4.10 is solved by marching in time, where a maximum time step is enforced by the stability requirement. The CFL number (Courant-Friedrichs-Lewy number) can be defined as $\frac{\Lambda \Delta T}{s \Delta l}$, which is the local dimensionless time step that governs the stability of the wave equation. Λ is taken as the local value of $\sqrt{\Lambda_x^2 + \Lambda_y^2}$, and Δl is taken to be the diameter of the control volume. If the ultimate goal is the steady state solution, then the time step does not need to be uniform throughout the domain. Instead, it can be taken as the local maximum allowable value. Larger time steps can be used for larger control volumes. We chose a uniform CFL number. The local time stepping technique allows the information to propagate more quickly throughout the domain to increase the convergence rate.

4.11 Extension of the Explicit Scheme to a Fully Implicit Scheme

The fully implicit scheme can be written at each time step as

$$\left(\frac{A_i H_i}{\Delta T} + C_i \right) P_i^{n+1} - \sum_{j=1, i \neq j}^{M} C_{ij} P_j^{n+1} = \frac{A_i H_i}{\Delta T} P_i^n, \tag{4.11}$$

in which all of the coefficents are the same as in the explicit scheme. For the steady state problem, the unsteady term only serves as an under-relaxation term. The simultanous linear algebraic equations can be written in matrix form as,

$$[C]^n\{P\}^{n+1} = \{d\}^n,$$

(4.12)

where $[C]^n$ is the coefficient matrix evaluated using the most recent values available , $\{P\}^{n+1}$ is the unknown vector at the new time level, and $\{d\}$ is the known source term. Because of the unstructured nature of the mesh, $[C]^n$ is a sparce matrix. At each row, only the elements that are associated with the directly neighboring vertices of the diagonal element vertex are not zero. Matrix $[C]^n$ can be broken into three parts,

$$[C]^n = [M]^n + [D]^n + [N]^n,$$

(4.13)

where $[M]^n$ is the lower triangular matrix, $[D]^n$ is the diagonal matrix and $[N]^n$ is the upper triangular matrix. The solution of the algebraic equation can be obtained by classical point iterations. For the point Jacobi method, the equations can be rearranged into

$$[D]^n\{P\}^{n+1} = \{d\} - [M]^n\{P\}^n - [N]^n\{P\}^n.$$

(4.14)

This equation can be readily solved by direct inversion of $[D]^n$. To speed up the convergence, the newly updated variables can be used, which result in the point Gauss-Seidel iteration

$$[D]^n \{P\}^{i+1} = \{d\} - [M]^n \{P\}^{i+1} - [N]^n \{P\}^i. \qquad (4.15)$$

Here the superscript i means the level of the inner iteration. Each iteration consists of two sub-iterations. The outer iteration is used to update the matrices, the inner iteration is used to solve the resulting linear equations. Since the final value of the matrices depends on the converged pressure, it is not necessary to get a converged result in the inner iteration; instead, a fixed number of iterations are carried out. The first sweep of the iteration starts from the beginning of the list, then the following sweep begins with the end of the list. This takes into account the effect that the diffusion terms of the Reynolds equation are elliptic in nature, and the disturbance is propagating in all directions at the same time. In this way, unconditional stability is achieved, and the time step can be chosen as arbitrarily large. When it is taken to be infinite, the above process is equivalent to direct interation.

4.12 Results and Discussion

The "LU" slider of Zeng and Bogy (1999) was chosen as an example for the mesh generation techniques as well as the explicit and implicit finite volume schemes. The simulation was done for a disk velocity of 13 m/s with a flying attitude of 25 nm fly

height, 155 $mrad$ pitch, 0 roll, and 0 skew. Figure 4.4 shows the coarsest conforming mesh and its dual Voronoi polygons with 605 nodes. It serves also as the coarsest level of mesh in the multi-grid technique that will be discussed in the next chapter. The figure clearly shows that the boundaries of the rail, the line that defines the taper and the boundaries of the slider are all well represented in the triangulation. This is a desirable quality for the multi-grid iterations. The meshes on the rail are also made finer than in the fully recessed region, and the mesh size and distribution can be easily controlled as explained above. Figure 4.5 shows a finer mesh with 7614 nodes. It can be seen that extremely fine meshes have been clustered toward the recess wall regions which makes the specification of the wall profile possible. Normally these regions with rapid geometrical changes are also regions with high-pressure gradients. The meshes on the rail were also refined. A high mesh size gradient was achieved while at the same time preserving the quality of the mesh. Figure 4.6 shows the adaptively refined mesh with 18150 nodes. From this figure we can see that several regions have been refined with a very fine mesh. They are the regions around the boundary and along the taper line of the two forward pads, the downwind recess wall region and the trailing part of the rail. From Figs. 4.7 and 4.8, which present the pressure contours and the three dimensional pressure profile, it can be seen that the high-pressure gradient regions have been accurately and efficiently captured by the adaptation process. Figure 4.9 shows the convergence history of the explicit and the implicit schemes. The explicit time marching was done on the mesh shown in Fig. 4.5 with a CFL of 1. It is clear that the explicit scheme converges very slowly. Even with 4000 time steps, the result is far from converged. The sudden jump of the error for the implicit scheme at the 200 time step is due to the mesh

71

adaptation. We first did time marching using the mesh shown in Fig. 4.5. After the solution converged to some extent, the adaptation occurred. The following time marching was done on the adapted mesh. The CFL number was 1.0E12. The convergence history shows that the convergence rate of the implicit technique has been greatly improved, with orders of simulation time being saved. Its rapid high frequency error damping quality also makes it a good candidate for multi-grid techniques. The converged result gives a positive force of 6.88 grams and a negative force of 3.75 grams. The maximum pressure is 4.85, and the minimum pressure is -0.74.

4.13 Summary and Conclusions

In this chapter, we present unstructured triangular mesh generation and adaptation techniques together with explicit and implicit finite volume schemes that are suitable for slider air bearing simulations for hard disk drives. Three different refinement and adaptation techniques based on two different Delaunay triangulation algorithms have been utilized to cluster fine meshes to the rail top, the recess wall and the high pressure gradient regions. At the coarsest level, the boundaries of the rail and the slider are well represented in the triangulation, which is important for the multi-grid iteration. At the second level, very fine meshes are clustered in the recess wall region where the geometry and the pressure profile change rapidly. In the simulation process, a mesh adaptation technique is used to refine the meshes in the high-pressure gradient regions. The undivided absolute pressure difference is used as the sensor in this mesh adaptation. The overall mesh generation process gives the user great flexibility and control over the distribution and quality of the meshes. This is demonstrated to be an efficient and

convenient way of generating quality meshes over the complex geometries in the air bearing simulations. An explicit finite volume scheme is first constructed, with which the steady state solution can be obtained by marching in time. But due to the stability limitation, only very small time steps can be used, which makes the convergence very slow. The explicit scheme is successfully extended to an implicit scheme in which the Gauss-Seidel point iteration technique is used to solve the simultaneous algebraic equations. The resulting scheme is unconditionally stable, and an arbitrarily large time step can be used. The convergence rate is greatly improved over the explicit scheme.
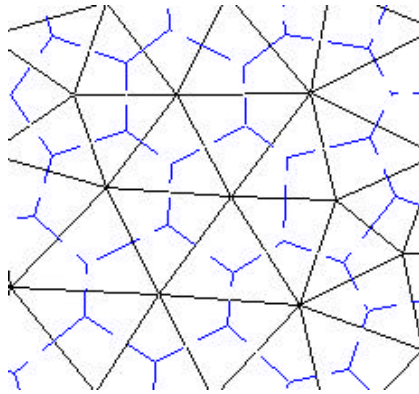
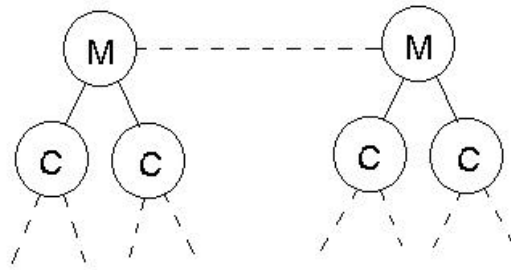**Fig. 4.1** Delaunay triangulation and its dual Voronoi diagram.

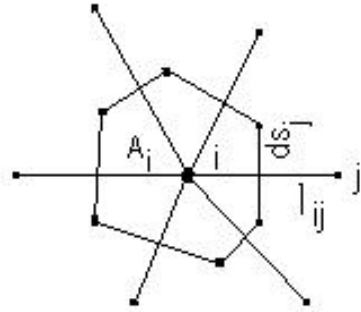**Fig. 4.2** Binary search tree for encroachment test.

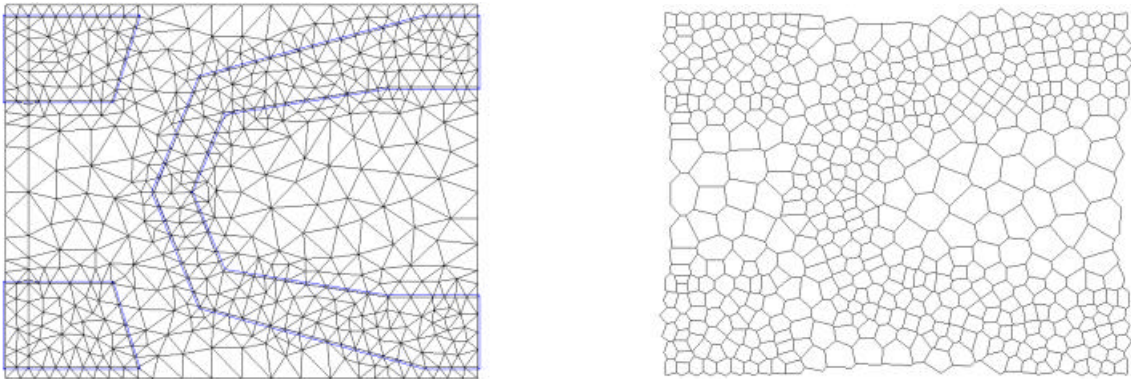**Fig. 4.3** Control volume for vertex based finite volume schemes.

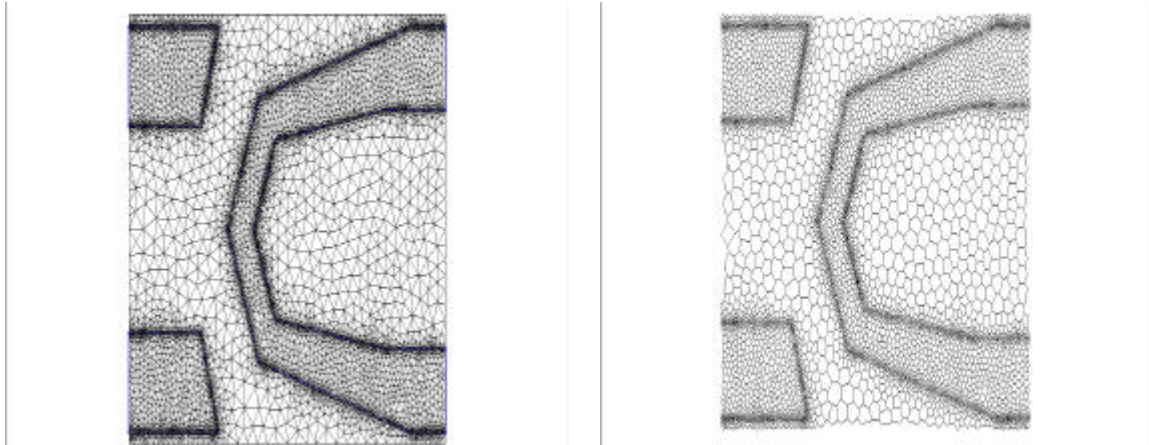**Fig. 4.4** Conforming background mesh and its dual Voronoi polygons (605 nodes).

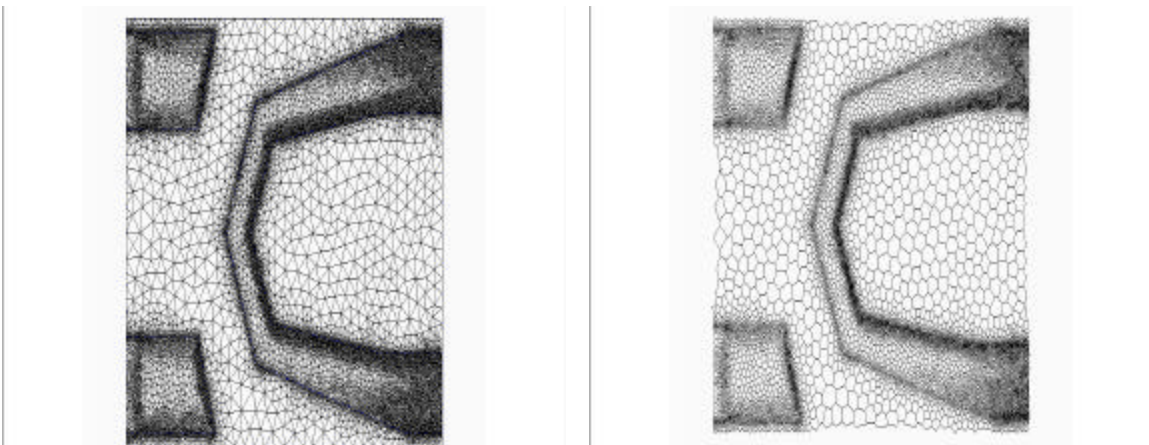**Fig. 4.5** Finer mesh with recess wall region refined and its Voronoi polygons (7614 nodes).

Fig. 4.6 Adapted finest mesh and its dual Voronoi polygons (18150 nodes).
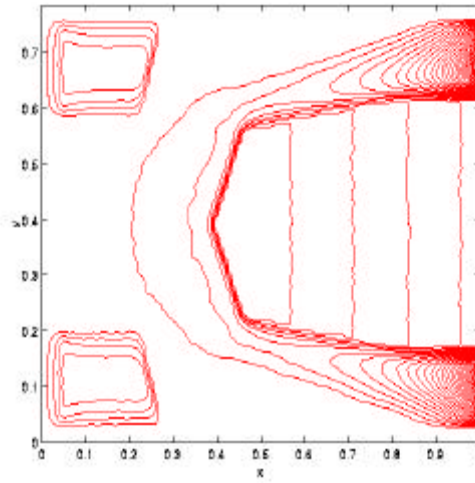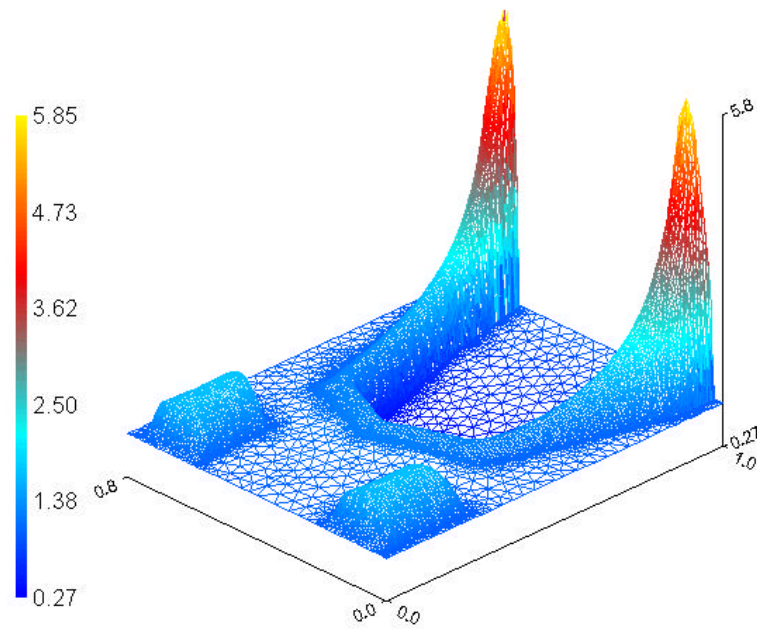
Fig. 4.7 Pressure contours.

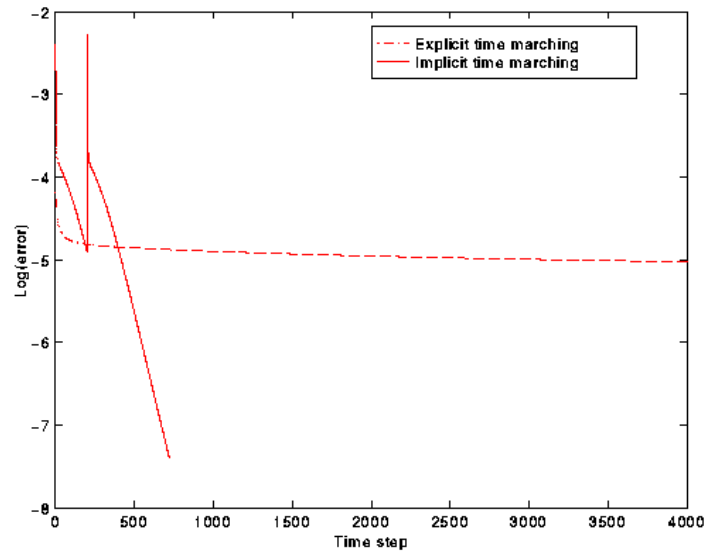**Fig. 4.8** Three dimensional pressure profile.

Fig. 4.9 Comparision of the convergence history for explicit and implicit schemes.

CHAPTER 5

NON-NESTED MULTI-GRID FINITE VOLUME SCHEME

5.1 Introduction

In Chapter 4, we fully discussed the advantages of using an unstructured triangular mesh over the rectangular Cartesian mesh, if the rail geometry is complicated. In that chapter we presented triangular mesh generation and adaptation techniques and an implicit finite volume scheme. The scheme is unconditionally stable and has good high frequency error damping qualities. Even though the time step can be chosen arbitrarily large the code still does not converge fast enough, due to the nature of the Gauss-Seidel smoother employed. From the convergence history it can be seen that the error drops very quickly at the beginning, its magnitude can be reduced about two orders with only a few time steps. But after the high frequency errors have been smoothed out, the convergence rate declines. In such cases, the multi-grid technique has proved to be an efficient way to greatly improve the convergence rate. In this chapter we employ a non-nested multi-grid technique that suits the nature of the new mesh generation process.

The multi-grid methodology was originally developed for solving elliptic equations, and it was later applied to other types of differential equations with great success. It takes into account the fact that most iteration techniques are efficient at smoothing out the error components with wave lengths comparable to or smaller than the mesh size (high frequency errors). But after these error components have been quickly

eliminated the convergence rate can greatly diminish with most computational time being consumed by the inefficient task of reducing the error components with wave lengths larger than the mesh size (low frequency errors). However, a coarser mesh sees these components as relatively higher frequency error, so if subsequent iterations are done on the coarser mesh, the error can be continually reduced efficiently. Therefore, instead of using only one mesh, the multi-grid technique iteratively solves the problem on several sets of mesh ranging from very fine to very coarse by switching back and forth between them. In this manner a fast convergence rate can be achieved.

Most multi-grid techniques are designed for nested meshes, in which several finer meshes can be combined to form a coarser mesh. This makes the transfer of variables and residues between the fine and coarser meshes relatively easy. But due to the nature of the Delaunay triangulation used in our approach, it is impossible to generate nested meshes. Therefore a non-nested multi-grid technique has to be used. Compared with other triangulation techniques like the pure longest-side bisection technique (Rivara 1989) that can be used to generate nested meshes, the relaxation of the nested requirement can also give the user more flexibility in the mesh generation.

In our approach the full storage approximation multi-grid strategy of Brandt (1977) is implemented. Mavriplis and Jameson's (1987 and 1988) restriction and interpolation functions that suit non-nested triangular meshes are used to transfer the variables and residues between the meshes. The resulting multi-grid implicit finite volume scheme is robust and efficient in solving the generalized Reynolds equation. The overall efficiency of the new code can compete with the rectangular mesh CML code even with a similar number of nodes. To get comparable results, the new code is

normally four to five times faster as a result of the significantly reduced number of required meshes.

Finally, the steady state flying height of the slider is found by a Quasi-Newton iteration method fully described in Dennis and Schnabel (1983).

5.2 Grid Transfer Operators for the Multi-Grid Algorithm

In the implementation of the multi-grid algorithm, variables and residues are transferred frequently between different mesh levels. The transfer procedure has vital influence on the overall performance of the multi-grid algorithm. Mavripilis and Jameson's (1987 and 1988) grid transfer operators have been shown to be well suited for multi-grid algorithms over unstructured triangular meshes. Here we simply adopt their techniques.

Let I_{k+1}^k be the operator used to transfer variables or residues from the fine mesh k+1 to the coarse mesh k, it is also called the restriction or projection operator. If I_{k+1}^k is operating on variables, it can simply be taken as a linear interpolation of the variables from the fine mesh nodes to the coarser mesh nodes. For example, if we want to get the pressure at vertex i, (see Fig.5.1) of the coarser mesh, we just need to locate the triangle IJK of the fine mesh that encloses it and do a linear interpolation. If it operates on the residue, then the residue at the vertex of a finer mesh can be distributed to the three vertices of the coarser triangle that encloses the vertex by its three area coordinates. For example, if we want to distribute R_I (the residue at vertex I in Fig. 5.2) to vertices i, j and

k of a coarse mesh, we simply send $L_i R_I$, $L_j R_I$ and $L_k R_I$ to vertices i, j and k respectively. L_i, L_j and L_k are area coordinates or shape functions of point I, which are equal to the area of the triangle formed by the opposite line to i, j and k and I itself and divided by the area of triangle ijk respectively. This can guarantee the conservation of the residue in the transfer process.

Let I_k^{k+1} be the operator used to transfer corrections from the coarse mesh k to the fine mesh k+1, it is also called the interpolation or prolongation operator. It can simply be taken as a linear interpolation. For each vertex of mesh k+1, we just need to locate the triangle of mesh k that encloses it and linearly interpolate the corrections at the three vertices of the triangle to it.

5.3 FAS Multi-Grid Algorithm

The full approximation storage (FAS) algorithm in Brandt (1977) is well suited for non-linear equations. It solves the equations by iterating over several sets of meshes. In abstract form it can be presented as follows. To simplify the expression we assume only two levels of mesh are used (k+1 represents the fine mesh and k represents the coarse mesh). Let L be the differential operator, $\underline{U}$ be the unknown vector and $\underline{F}$ be the source term, then the differential equation can be written as

$$L\underline{U} = \underline{F}. \tag{5.1}$$

On the fine mesh, the equation can be discretized as

$$L_{k+1}\underline{U} = \underline{F}_{k+1},$$ (5.2)

where L_{k+1} is the discretized operator over the mesh k+1. A certain number of iterations can be carried out until the convergence rate becomes slower. Then the solution $\underline{u}^{k+1}$ and the residue $\underline{F}_{k+1} - L_{k+1}\underline{u}^{k+1}$ are transferred to the coarse mesh, and the following equation

$$L_k\underline{U} = I_{k+1}^k(\underline{F}_{k+1} - L_{k+1}\underline{u}^{k+1}) + L_k\left(I_{k+1}^k\underline{u}^{k+1}\right)$$ (5.3)

is solved there with an initial guess $I_{k+1}^k\underline{u}^{k+1}$. L_k is the discretized operator on mesh k. I_{k+1}^k is the grid transfer operator used to transfer either the solution variables or residues from mesh k+1 to k. A solution $\underline{u}^k$ is found after enough iterations. Finally the correction on mesh k is transferred back to k+1, and the solution on mesh k+1, $\underline{u}^{k+1}$ is updated as

$$\underline{u}^{k+1} \leftarrow \underline{u}^{k+1} + I_k^{k+1}\left(\underline{u}^k - I_{k+1}^k\underline{u}^{k+1}\right),$$ (5.4)

which serves as the initial guess of the next multi-grid circle iteration. I_k^{k+1} is the grid transfer operator used to transfer the correction from mesh level k to k+1. The above process continues until the error drops to an acceptable level.

83

For our implicit finite volume scheme, the differential operator on level k+1can be written as

$$(L_{k+1}\underline{P})_i = \left(\frac{A_i H_i}{\Delta T} + C_i\right)P_i^{n+1} - \sum_{j=1,i\neq j}^{M} C_{ij}P_j^{n+1}.$$ (5.5)

Similar expressions hold for the other levels. The source term on the fine mesh k+1 is

$$(\underline{F}_{k+1})_i = \frac{A_i H_i}{\Delta T}P_i^n.$$ (5.6)

On the coarse level k, it can be written as

$$\underline{F}_k = I_{k+1}^k(\underline{F}_{k+1} - L_{k+1}\underline{u}^{k+1}) + L_k\left(I_{k+1}^k\underline{u}^{k+1}\right)$$ (5.7)

In our actual implementation three levels of mesh are used. Figure 5.3 shows the multi-grid V cycles used in the simulation. To get a good initial guess we first do forty iterations on the coarsest mesh, then we linearly interpolate the solution variables to the second level mesh. Twenty iterations are carried out there before we transfer the solution variables to the third level mesh. After that, N V cycles are carried out before we adaptively refine the third level mesh according to the pressure distribution. The following V cycles are performed over the new finest mesh and the other two meshes until convergence is achieved. Each V cycle consists of one iteration on the finest mesh, then the solution variables and residues are transferred to the second level mesh using the

84

operators we previously defined. Then four iterations are done there. Again, solution variables and residues are transferred to the first level mesh. Eight iterations are carried out before the corrections are transferred back and used to update the second level mesh solution. Four more iterations are done on the second level mesh. Finally, the finest mesh solution is updated by the correction transferred from the second level mesh, which serves as the initial guess for the next V cycle. There is no solid physical background for deciding how many outer iterations should be carried out on each mesh level to give the best result. The above choices correspond to optimized results for some sliders. Within each outer iteration, there is no need to solve the linear algebra equations extremely well, since for the final steady state solution the coefficients depend on the solution itself. In each outer iteration we linearized the equations by taking them to depend only on the solution of the previous outer iteration. In our code, about ten to twenty Gauss-Seidel iterations are used to find an approximation solution for the set of linear algebra equations with coefficients updated at the beginning by the solution of the last outer iteration. Again, the choice of the number of inner iterations corresponds to optimized results for some sliders.

5.4 Inverse Problem

In air bearing simulation the steady state flying attitude corresponding to a fixed prescribed load is more important than the pressure distribution of one fixed attitude, because it is the former that influences the performance of the hard disk drive. The

steady state flying attitude is defined as the one at which the pre-enforced suspension force and pitch and roll torques are balanced by their counterparts generated by the air bearing force. We can define a vector $\underline{R} = (R_1, R_2, R_3)$, where

$$R_1 = F_{air} - F_s,\tag{5.8}$$

$$R_2 = \frac{(M_{air})_p + (M_s)_p + (M_{shear})_p}{F_{air}} - X_0,\tag{5.9}$$

$$R_3 = \frac{(M_{air})_r + (M_s)_r + (M_{shear})_r}{F_{air}} - Y_0.\tag{5.10}$$

F_{air} is the air bearing force, F_s is the applied suspension force, M_{air}, M_s and M_{shear} are moments caused by air bearing pressure, applied suspension force and viscous shear force, respectively. Subscripts p and r represent the projection in the pitch and roll directions. X_0 and Y_0 are coordinates of the position where the suspension force is applied. $\underline{R}$ is a non-linear function of the flying height, the pitch angle and the roll angle. The object is to find a particular flying attitude that makes $\underline{R}$ zero, which corresponds to the steady state flying attitude. The Quasi-Newton iteration method for non-linear problems fully described in Dennis and Schnabel (1983) is implemented to find the steady state attitude. Our experience shows that generally only a few Newton steps are needed to find the steady state solution.

5.5 Results and Discussion

The IBM Travelstar slider (Fig. 5.4) and the NSIC load/unload slider (Fig. 5.16) are used to demonstrate the performance of the above multi-grid numerical scheme and the Quasi-Newton iteration method. Figures 5.5, 5.6 and 5.7 show the three initial meshes for the IBM slider. Figure 5.8 shows the adaptively refined third level mesh. Figures 5.9 and 5.10 show the pressure contours at the steady state attitude obtained by the triangular mesh solver and the rectangular mesh solver, respectively. They are almost the same, differing only by some small details. Comparing Fig. 5.8 and Fig. 5.9, we can see that all the regions with large geometric change or pressure gradient have been efficiently captured by our mesh generation and adaptation techniques. Figure 5.11 shows the comparison of the convergence rate between the fully implicit iterations on a single mesh and that of the multi-grid iteration at a fixed attitude without mesh adaptation. The single mesh is the same as the finest mesh of the multi-grid iteration. From the figure it can be seen, for the single mesh iteration, that the error initially drops very fast, only ten iterations are needed to bring the error down from about 10^{-2} to 10^{-4}. But after the high frequency error has been smoothed out, the curve flattens. It takes about another 200 iterations to further reduce the error by two orders of magnitude. The multi-grid curve shows that all error components can be continuously and efficiently removed. The log error drops almost linearly with the number of outer iterations (time steps). Figure 5.12 shows the flying height grid convergence comparison between the triangular mesh solver and the rectangular mesh solver. The former achieves grid convergence with much fewer node points. This is due to the fact that the node points can be much more reasonably distributed by the triangular solver than the rectangular

solver. Figures 5.13 and 5.14 show the pitch angle and roll angle grid convergence history. For the node number corresponding to flying height convergence, both codes reach grid convergence. Figure 5.15 shows a plot of the simulation time for finding the steady state attitude as a function of the grid size. For both solvers the simulation time increases almost linearly with the node number. For the same number of node points, the triangular mesh solver costs a little more time than the rectangular solver. But this is not always true. The rail shape of the modified IBM slider is extremely regular. In this case, the rectangular mesh solver is supposed to do a good job. But the triangular mesh solver can treat all shapes equally well, no matter how complicated they are.

To demonstrate this, the NSIC load/unload slider (Fig. 5.16) is simulated. Figure 5.17 shows the flying height grid convergence history. Again, the triangular mesh solver achieves grid convergence at a much smaller grid size. But this time, the performance of the rectangular mesh solver deteriorates substantially. Figure 5.18 shows the simulation time used to find the steady state flying attitude as a function of node number. This time, at a similar node number, the triangular mesh solver uses almost the same amount of time as the rectangular mesh.

5.6 Summary and Conclusions

A non-nested FAS multi-grid algorithm has been successfully employed to speed up the convergence rate of an implicit finite volume scheme that we previously designed for slide air bearing simulation. The multi-grid algorithm requires no relationship between different mesh levels. On the average nearly one order of simulation time has been saved by implementing the multi-grid algorithm. In addition the steady state flying attitude is found by a Quasi-Newton method. Even though the unstructured nature of the grid makes the situation much more complicated than that of the structured rectangular mesh, and all the information can only be stored and retrieved through a complicated data structure, the efficiency of current code can compete with the rectangular mesh counterpart with similar grid size. To get comparable results, the triangular mesh solver is generally four to five times faster depending on the complexity of the rail shape.
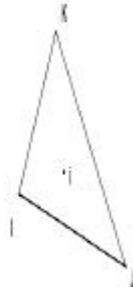
Fig. 5.1 Grid restriction operator.
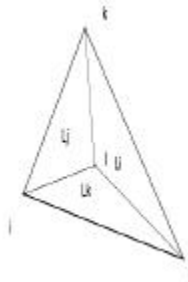
Fig. 5.2 Residue distribution operator.
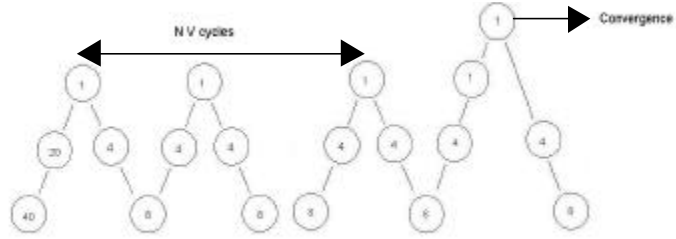
Fig. 5.3 The muti-grid V cycles.
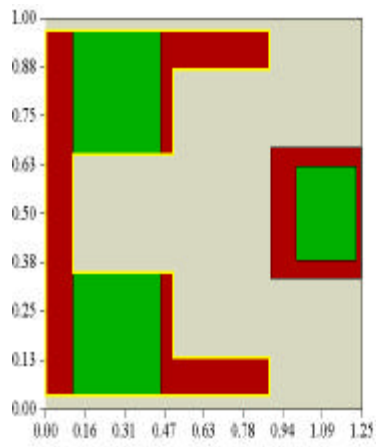
Fig. 5.4 The IBM Travelstar slider with slight modification.
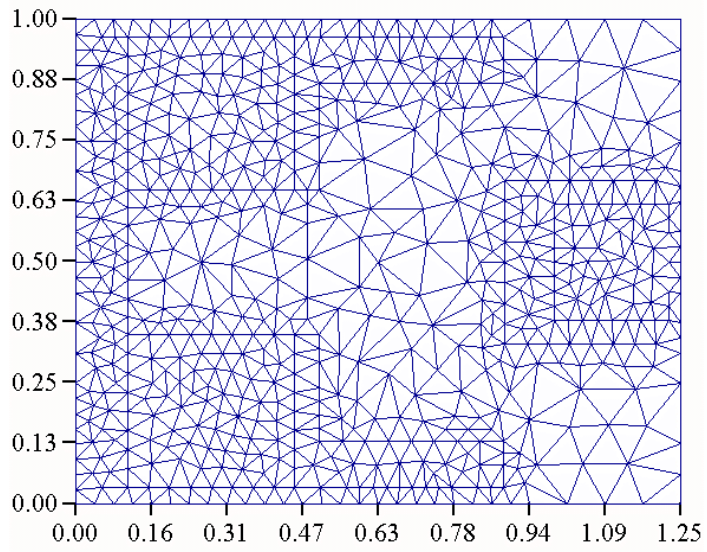
Fig. 5.5 The first level conforming mesh with 656 nodes.
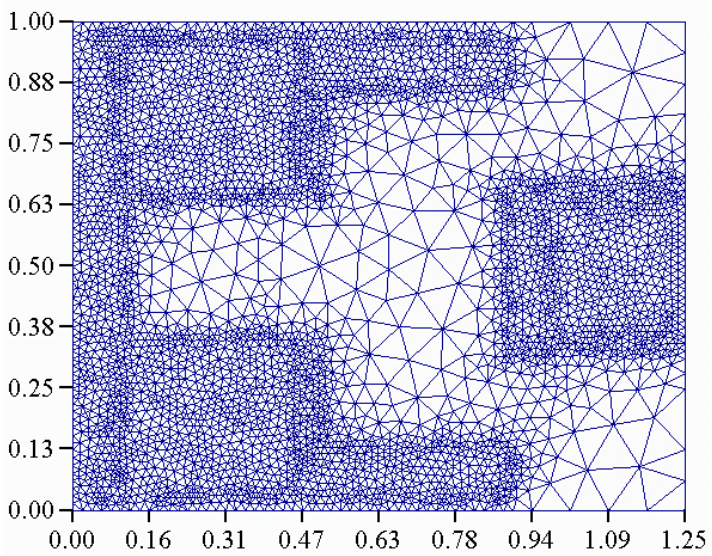

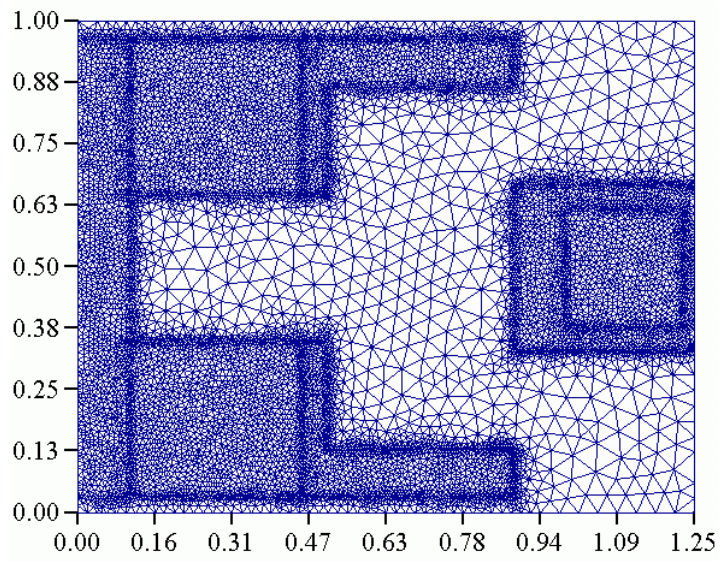**Fig. 5.6** The second level mesh with 4108 nodes.

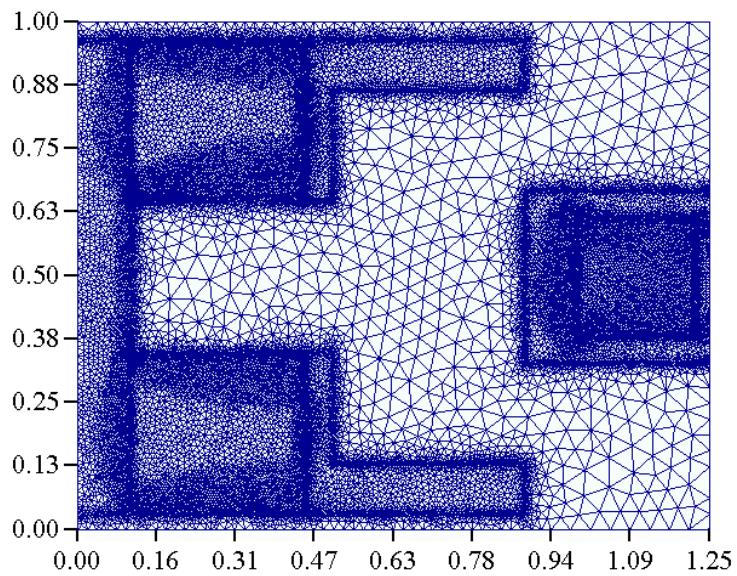**Fig. 5.7** The third level mesh before mesh adaptation with 12642 nodes.

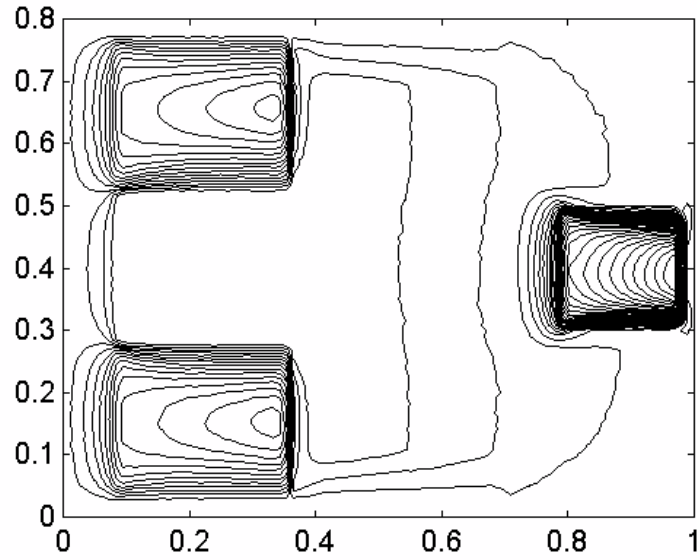**Fig. 5.8** The third level mesh after mesh adaptation with 18145 nodes.

Fig. 5.9 The steady state pressure contour of the solution by the 18145 nodes triangular

mesh solver.
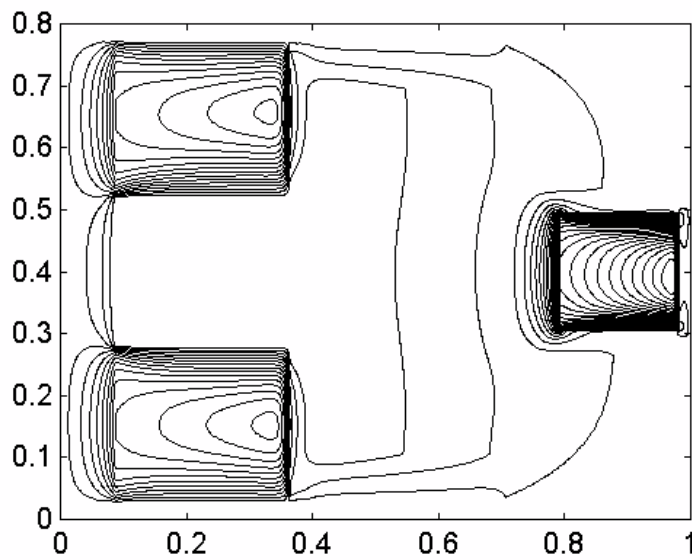
Fig. 5.10 The steady state pressure contour of the solution by the 148225 nodes
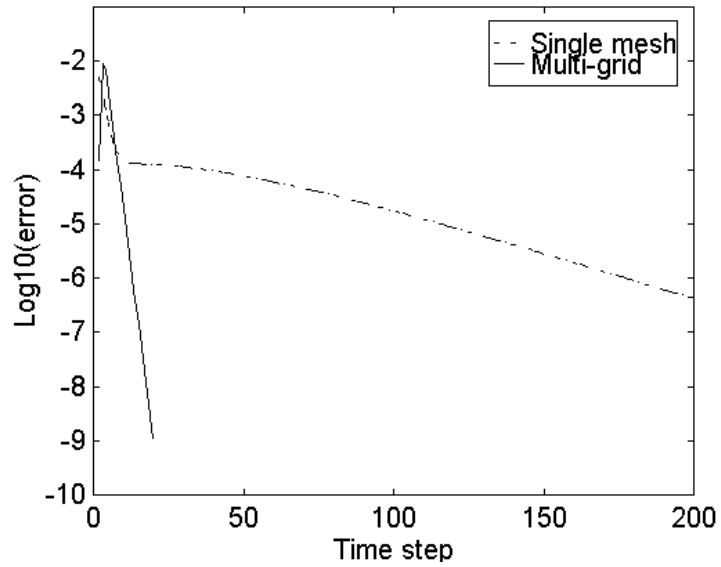
(385X385) rectangular mesh solver.

Fig. 5.11 The convergence history of iteration on a single mesh and multi-grid iteration.
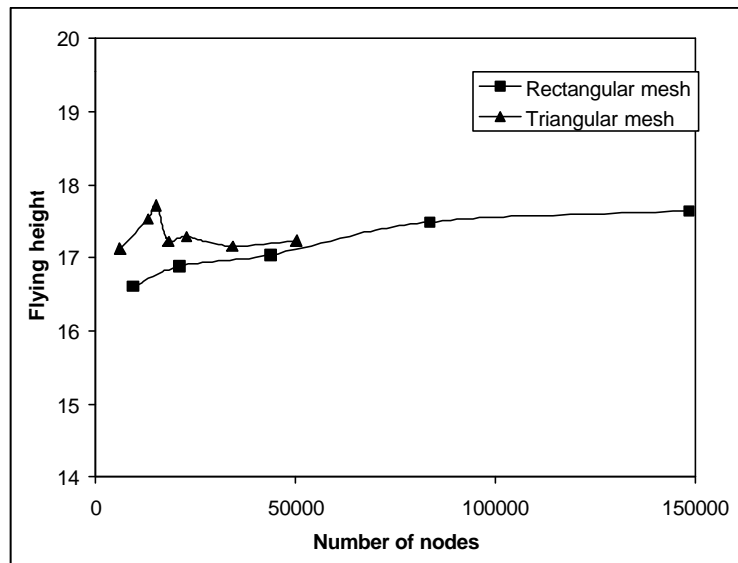

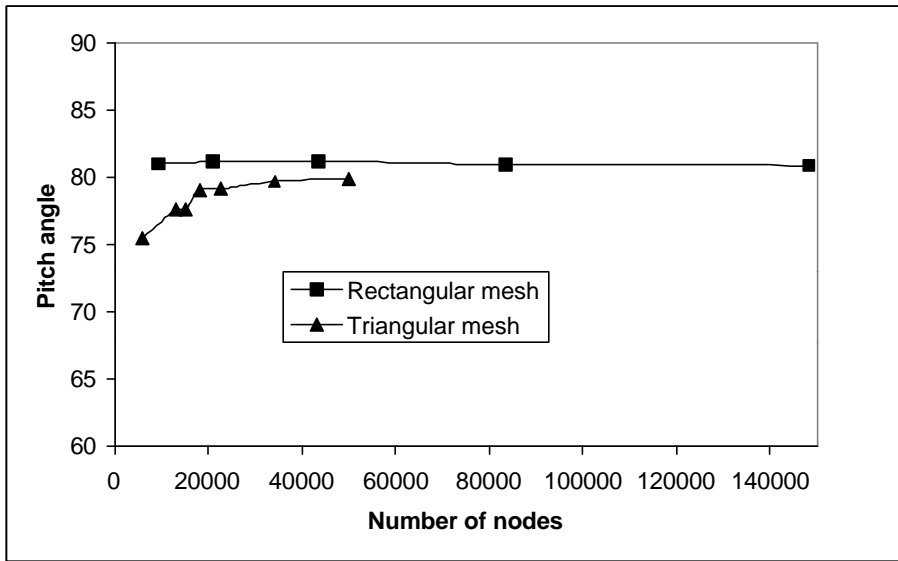**Fig. 5.12** The grid convergence comparison of nominal flying height (NM).

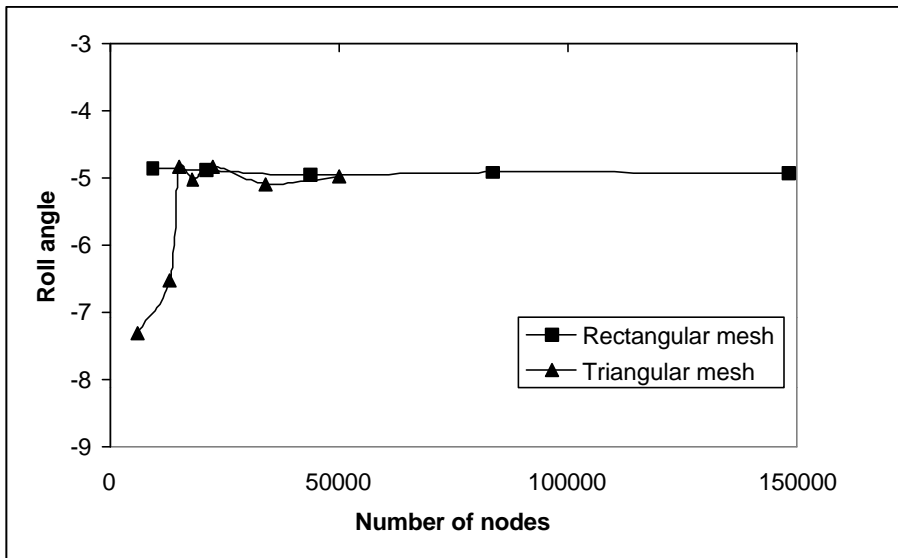**Fig. 5.13** The grid convergence comparison of pitch angle ($mRad$).

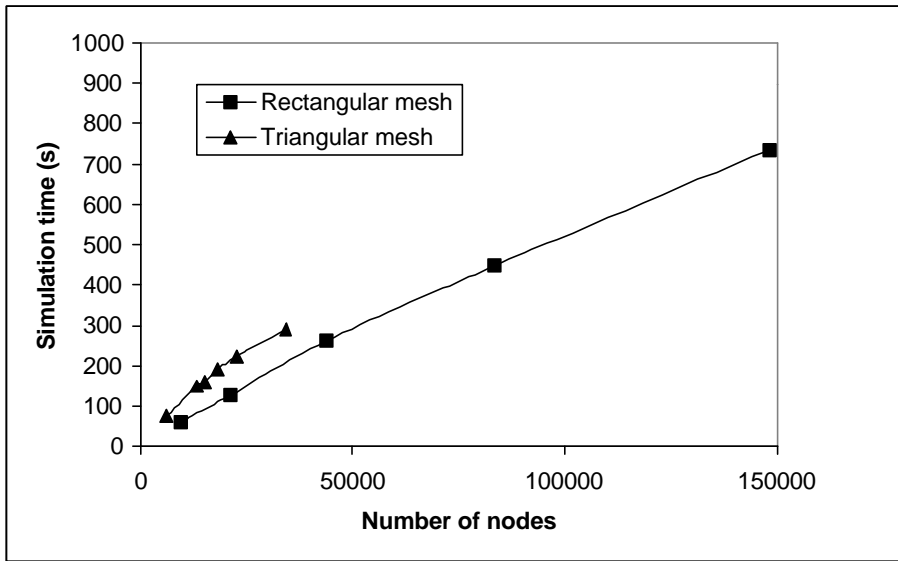**Fig. 5.14** The grid convergence comparison of roll angle ($mRad$).

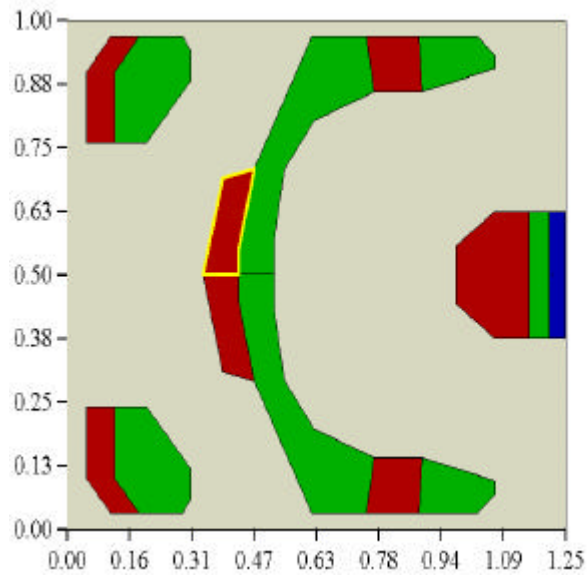**Fig. 5**.**15** The simulation time as a function of node number.
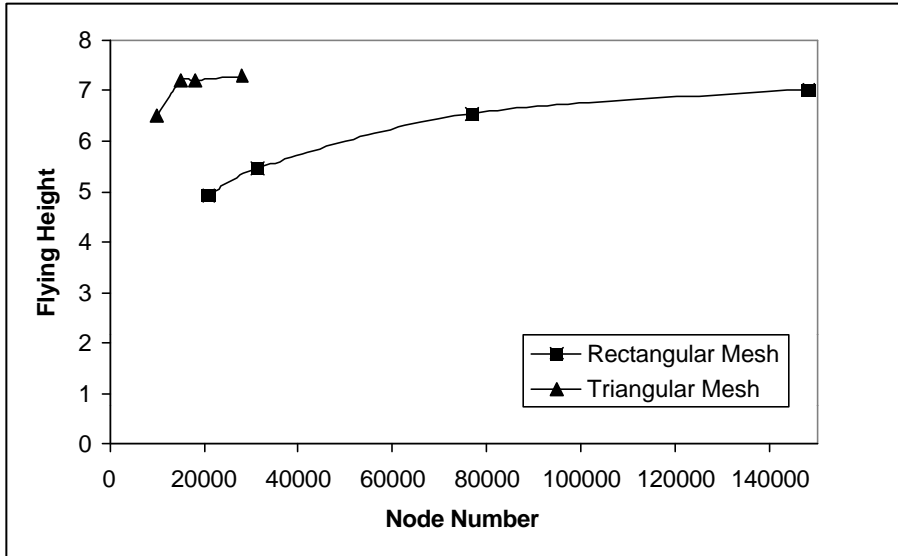

Fig. 5.16 NSIC load/unload slider.

Fig. 5.**17** The grid convergence comparison of nominal flying height (NM) of the NSIC
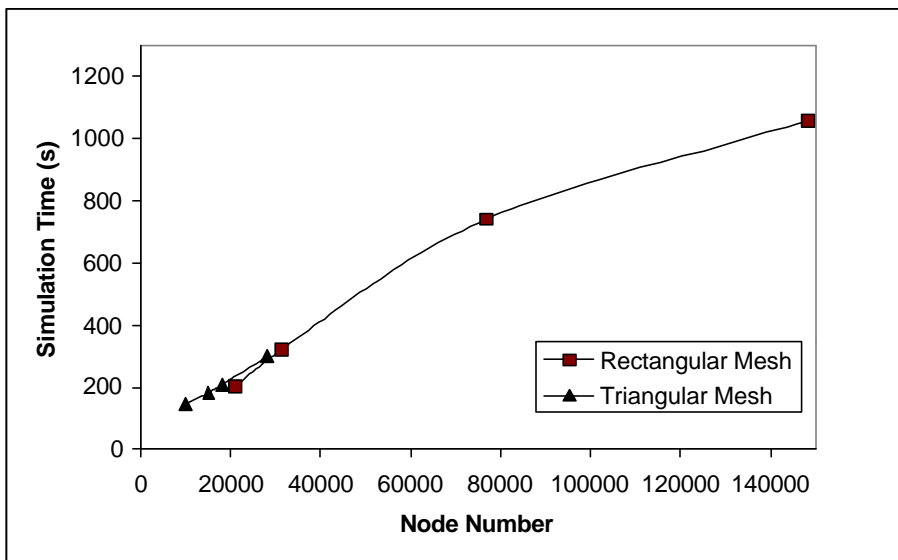
load/unload slider.

Fig. 5.18 The simulation time as a function of node number for the NSIC load/unload

slider.

CHAPTER 6

INTRODUCTION AND COMPARISION OF SEVERAL NUMERICAL

SCHEMES ON UNSTRUCTURED TRIANGULAR MESHES

6.1 Introduction

In Chapters 4 and 5, we presented triangular mesh generation and refinement and adaptation techniques that suit the slider air bearing problem based on the Delaunay method (Sloan, 1987 and Ruppert, 1995) and the longest-side-bisection Delaunay refinement technique (Rivara and Inostroza, 1997). An implicit non-nested multi-grid finite volume scheme was also constructed over this mesh. The numerical scheme gives comparable results with much less simulation time to these of an older code developed in the Computer Mechanics Laboratory (Lu, 1997), which has been widely accepted in the hard disk drive industry. But the new numerical method has two potential shortcomings. First, the scheme is an extension of the numerical schemes listed in (Patankar, 1980) for convection and diffusion type equations on a rectangular Cartesian mesh to the unstructured triangular mesh. These schemes are quite diffusive if the convection is strong, which is true in the slider air bearing problem. Second, the control volumes of the new scheme are the dual Voronoi Polygons of the Delaunay triangulation. This requires the quality of the mesh to be extremely good, otherwise the Voronoi polygon can be highly distorted.

To improve the above potential shortcomings, in this chapter we present three different numerical schemes that use the same meshes as our previous approach but take the median dual of the triangular mesh as the control volume. The median dual is different from the dual Voronoi polygons; it is obtained by connecting the neighboring centroids of the triangles. By the adoption of a less diffusive spatial discretization, we also hope to improve the accuracy of the numerical schemes themselves without significantly increasing the simulation time. In the new approaches, we use the "flux difference splitting" (FDS) technique of Roe (1981), the positive streamwise invariant (PSI) residue distribution approach of Struijs et al. (1991) and Paillere et al. (1994) and the streamline upwind Petrov-Galerkin (SUPG) finite element scheme (Hughes and Brooks, 1979) cast as a residue distribution formula (Deconinck et al., 1993) to discretize the convection part of the generalized Reynolds equation, while a standard Galerkin type method (Barth, 1991) is used to model the diffusion part of the equation. A non-nested multi-grid technique based on the full storage approximation multi-grid strategy of Brandt (1977) is implemented to improve the convergence rate of the Gauss-Seidel smoother used to solve the non-linear discretized equation. Mavriplis and Jameson's restriction and interpolation functions (Mavriplis and Jameson, 1987 and Mavriplis, 1988) that suit non-nested triangular meshes are used to transfer the variables and residues between the meshes.

6.2 the FDS Upwind Discretization of the Convection Equation

Ignore the diffusion terms in the generalized Reynolds equation (eq. 4.2) for the moment and divide all terms of the equation by $\mathbf{s}$. After integrating the convection equation over the median dual Ω (with an area A_Ω) around each vertex, we can rewrite the equation as

$$A_\Omega \frac{\partial}{\partial T}(PH) + \oint_{\partial\Omega}\left[\frac{\Lambda_x}{\mathbf{s}}n_x PH + \frac{\Lambda_y}{\mathbf{s}}n_y PH\right]dl = 0. \tag{6.1}$$

In discretized form this can be writen as

$$\frac{A_\Omega}{\Delta T}\left[(PH)_i^{n+1} - (PH)_i^n\right] + \sum_{j=1}^{M}F_{ij}\cdot\Delta l_{ij} = 0, \tag{6.2}$$

where Δl_{ij} is the distance between the two centroids j' and $(j+1)'$ (Fig. 6.1). F_{ij} is the numerical flux across Δl_{ij} given by Roe's flux difference splitting technique (Roe, 1981) as

$$F_{ij} = \frac{1}{2}\left[F((PH)_L) + F((PH)_R) - |\overline{I}|((PH)_R - (PH)_L)\right]. \tag{6.3}$$

$(PH)_L$ and $(PH)_R$ are the left and right state values of PH to the middle of the line ij. $|\overline{I}|$ is the average wave speed defined as

$$2s|\bar{I}| = \left|(\Lambda_n)_i + (\Lambda_n)_j\right|. \tag{6.4}$$

$(\Lambda_n)_i$ and $(\Lambda_n)_j$ are the projections of the bearing number vector (Λ_x, Λ_y) evaluated at the vertices i and j, respectively, onto the outward normal vector $\underline{n}_{ij}$ of the boundary line connecting j' and $(j+1)'$. The bearing number vector is a continous known function of space only under a fixed flying attitude. Due to the small size of the slider compared with the radius, the bearing number vector changes slowly across the slider. F is the flux function defined as

$$sF(PH) = (\Lambda_x, \Lambda_y) \cdot \underline{n}_{ij}(PH). \tag{6.5}$$

Temporally, it can be linearized as

$$F(PH)^{n+1} = F(PH)^n + \frac{\partial F}{\partial (PH)}\left((PH)^{n+1} - (PH)^n\right). \tag{6.6}$$

It can be easily shown that the projection of the bearing vector along each line on the disk is a constant, which means the x and y components of the bearing number vector, Λ_x and Λ_y commute with the derivative operator. As a result

$$s\frac{\partial F}{\partial (PH)} = (\Lambda_x, \Lambda_y) \cdot \underline{n}_{ij} = \Lambda_n. \tag{6.7}$$

The final upwind scheme can be written as

$$\left[\frac{A_\Omega}{\Delta T} + \sum_{j=1}^{M} \boldsymbol{I}^+ \Delta l_{ij}\right](PH)_i^{n+1} + \sum_{j=1}^{M} \boldsymbol{I}^- \Delta l_{ij}(PH)_j^{n+1} =$$

$$\left[\frac{A_\Omega}{\Delta T} + \sum_{j=1}^{M} \boldsymbol{I}^+ \Delta l_{ij}\right](PH)_i^n + \sum_{j=1}^{M} \boldsymbol{I}^- \Delta l_{ij}(PH)_j^n \qquad (6.8)$$

$$-\frac{1}{2}\sum_{j=1}^{M}\left\{F\big((PH)_L\big) + F\big((PH)_R\big) - |\overline{\boldsymbol{I}}|\big((PH)_R - (PH)_L\big)\right\}\Delta l_{ij},$$

where

$$2\boldsymbol{s}\boldsymbol{I}^+ = (\Lambda_n)_i + |(\Lambda_n)_i|, \qquad (6.9)$$

and

$$2\boldsymbol{s}\boldsymbol{I}^- = (\Lambda_n)_j - |(\Lambda_n)_j|. \qquad (6.10)$$

If $(PH)_L$ and $(PH)_R$ are evaluated at vertices i and j, then the space discretization has only first order accuracy. Here the linear reconstruction technique in (Barth and Jespersen, 1989) is adopted to achieve a higher order space accuracy. The left and right state variables can be evaluated as

$$(PH)_L = (PH)_i + \Phi_i \nabla(PH)_i \cdot \underline{\Delta r_{ij}}, \qquad (6.11)$$

and

$$(PH)_R = (PH)_j - \Phi_j \nabla(PH)_j \cdot \underline{\Delta r_{ij}}, \qquad (6.12)$$

where $\nabla(PH)$ is the average gradient of PH at vertex i or j, which can be evaluated by use of a simple Green's theorem or least square approach (Barth, 1993). In our calculation, the Green's theorem method is used. $\underline{\Delta r_{ij}} = \frac{1}{2}(\underline{r}_j - \underline{r}_i)$ is the vector pointing from i to j with half its length. To avoid the appearance of new local maximum or minimum after the reconstruction procedure, the variable Φ ranging from 0 to 1 is used to limit the reconstructed left and right hand state variables, which is determined by using the same method as in (Barth and Jespersen, 1989).

6.3 The Residue Distribution Discretization of the Convection Equation

In the residue distribution schemes of Struijs et al. (1991) and Paillere et al. (1994), the residual in triangle T is defined as

$$
\begin{aligned}
\boldsymbol{f}^T &= -\iint_T \frac{\partial(PH)}{\partial T} dA = \iint_T \left(\frac{\Lambda_x}{\boldsymbol{s}}, \frac{\Lambda_y}{\boldsymbol{s}} \right) \cdot \nabla(PH) dA = A_T \overline{\boldsymbol{l}}_T \cdot \nabla(PH) \\
&= \sum_{j=1}^{3} k_j^T (PH)_j
\end{aligned}
\qquad (6.13)
$$

where $\boldsymbol{s}\overline{\boldsymbol{l}}_T = \overline{(\Lambda_x, \Lambda_y)}$ is the averaged wave speed in each triangle. The conservation constraint gives

$$
\overline{\boldsymbol{l}}_T = \frac{1}{A_T \boldsymbol{s}} \iint_T (\Lambda_x, \Lambda_y) dA = \frac{1}{3\boldsymbol{s}} \left[(\Lambda_x, \Lambda_y)_1 + (\Lambda_x, \Lambda_y)_2 + (\Lambda_x, \Lambda_y)_3 \right]. \qquad (6.14)
$$

In the above formulation, the bearing number is assumed to vary linearly in each triangle. The inflow parameter k_j^T is defined as

$$2k_j^T = \overline{\mathbf{I}}_T \cdot \overline{n}_j \,, \tag{6.15}$$

where $\overline{n}_j$ is the inward normal of each edge of the triangle with a magnitude equal to its length (see Fig. 6.2). In the air bearing problem k_j^T only needs to be calculated once and stored for later use.

The residual of each triangle is sent to its three nodes by the distribution coefficient $\mathbf{b}_i^T$

$$\mathbf{f}_i^T = \mathbf{b}_i^T \mathbf{f}^T \,. \tag{6.16}$$

The convection equation can be discretized as

$$\frac{A_\Omega}{\Delta T}\left[(PH)_i^{n+1} - (PH)_i^n\right] = -\sum_{T=1}^{M} \mathbf{f}_i^T = \sum_{T=1}^{M} \mathbf{b}_i^T \mathbf{f}^T = \sum_{T=1}^{M} \mathbf{b}_i^T \sum_{j=1}^{3} k_j^T (PH)_j^{n+1} \,. \tag{6.17}$$

In the above formulation the solution is updated by accumulating the residues at node i triangle by triangle. To put all the schemes in a unified form, it can be re-formulated such that the solution can be updated edge by edge

$$\frac{A_\Omega}{\Delta T}\left[(PH)_i^{n+1} - (PH)_i^{n}\right] = \sum_{T=1}^{M} \boldsymbol{b}_i^{T} \sum_{j=1}^{3} k_j^{T} (PH)_j^{n+1}$$

$$= \sum_{j=1}^{M}\left[\left(\boldsymbol{b}_i^{T1}k_i^{T1} + \boldsymbol{b}_i^{T2}k_i^{T2}\right)(PH)_i^{n+1} + \left(\boldsymbol{b}_i^{T1}k_j^{T1} + \boldsymbol{b}_i^{T2}k_j^{T2}\right)(PH)_j^{n+1}\right],$$

$$(6.18)$$

where $T1$ and $T2$ are the two neigboring triangles sharing the edge ij.

For the PSI scheme (Struijs et al., 1991 and Paillere et al., 1994), the distribution coefficient can be written as

$$\boldsymbol{b}_i^{T} = MinMod\left[-\frac{\max\left(0, k_i^{T}\right)\min\left(0, \left((PH)_i - (PH)_{in}\right)\boldsymbol{f}^{T}\right)}{\boldsymbol{f}^{T}}\right], \qquad (6.19)$$

where $(PH)_{in}$ is the linearly interpolated PH value at the inflow point, which can be evaluated as

$$(PH)_{in} = \frac{\sum\limits_{j=1}^{3}\min\left(0, k_j^{T}\right)(PH)_j}{\sum\limits_{j=1}^{3}\min\left(0, k_j^{T}\right)}. \qquad (6.20)$$

For the SUPG finite element scheme (Hughes and Brooks, 1979) in residue distribution form (Deconinck, 1993), the distribution coefficient can be written as

$$\boldsymbol{b}_i^{T} = \frac{1}{3} + 0.5\frac{h}{\left|\overline{\boldsymbol{I}}_T\right|A_T}k_i^{T}. \qquad (6.21)$$

The length scale h can be approximated as

$$h = \max_{i=1}^{3} \left(\left| (n_i)_x \right|, \left| (n_i)_y \right| \right). \tag{6.22}$$

6.4 The Finite Element Discretization of the Diffusion Term

The diffusion term can be discretized with a Galerkin weighted integral (Barth, 1991)

$$\iint_{A_\Omega} \left[\nabla \cdot \left(QPH^3 \frac{\partial P}{\partial x}, QPH^3 \frac{\partial P}{\partial y} \right) \right] dA = \sum_{j=1}^{M} W_{ij} \left[(P)_j^{n+1} - (P)_i^{n+1} \right]. \tag{6.23}$$

Here A_Ω is the median dual, and the weights W_{ij} are defined as

$$2sW_{ij} = \overline{QPH^3}^L \cot an(a_{Lj}) + \overline{QPH^3}^R \cot an(a_{Rj}), \tag{6.24}$$

where $\overline{QPH^3}^L$ and $\overline{QPH^3}^R$ are the average values of QPH^3 in the triangle to the left or

right of the edge ij. a_{Lj} and a_{Rj} are the opposite angles to the edge ij as shown in Fig.

6.1.

6.5 Iterative Solver of the Discretized Equations

All the above numerical schemes can be written in a unified form as

$$C_i P_i^{n+1} + \sum_{j=1}^{M} C_{ij} P_j^{n+1} = S_i \left(P_i^n, P_j^n \right). \tag{6.25}$$

For the FDS scheme

$$C_i = \left[\frac{A_\Omega}{\Delta T} + \sum_{j=1}^{M} \boldsymbol{I}^+ \Delta l_{ij} \right] H_i + \sum_{j=1}^{M} W_{ij}, \tag{6.26}$$

$$C_{ij} = \boldsymbol{I}^- \Delta l_{ij} H_j - W_{ij}, \tag{6.27}$$

$$S_i \left(P_i^n, P_j^n \right) = \left[\frac{A_\Omega}{\Delta T} + \sum_{j=1}^{M} \boldsymbol{I}^+ \Delta l_{ij} \right] (PH)_i^n + \sum_{j=1}^{M} \boldsymbol{I}^- \Delta l_{ij} (PH)_j^n$$
$$- \frac{1}{2} \sum_{j=1}^{M} \left\{ F\left((PH)_L \right) + F\left((PH)_R \right) - \left| \overline{\boldsymbol{I}} \right| \left((PH)_R - (PH)_L \right) \right\} \Delta l_{ij} \tag{6.28}$$

For schemes in residue distribution form

$$C_i = \frac{A_\Omega}{\Delta T} H_i + \sum_{j=1}^{M} \left(\boldsymbol{b}_i^{T1} k_i^{T1} + \boldsymbol{b}_i^{T2} k_i^{T2} \right) H_i + \sum_{j=1}^{M} W_{ij}, \tag{6.29}$$

$$C_{ij} = -\left(\boldsymbol{b}_i^{T1} k_j^{T1} + \boldsymbol{b}_i^{T2} k_j^{T2} \right) H_j - W_{ij}, \tag{6.30}$$

$$S_i\left(P_i^n, P_j^n\right) = \frac{A_\Omega}{\Delta T}(PH)_i^n .\tag{6.31}$$

Equation (6.25) is still nonlinear, because C_i and C_{ij} depend on P. One simple way to linearize the equation is to take P as the most recent known value of the last iteration, this is the so-called lagging technique. The resulting simultaneous equations are solved by a two sweep point Gauss-Seidel method. The first sweep starts from the beginning of the vertex list, and the second sweep starts from the end of the list. This takes into account the fact that the diffision terms in the Reynolds equation are elliptic in nature, and disturbance information is spread simultaneously in all directions.

The steady state solution for one fixed attitude is found by marching in time. For steady state problems with fixed attitude, the unsteady term is not needed physically, but it is kept here to serve as an under-relaxation term. When a relatively large time step is used, the unsteady term can be ignored, and the technique is more like a direct iteration than time marching. The implicit schemes are unconditionally stable, so an arbitrarily large CFL number such as 1.0E12 can be used. At the beginning of each time step the coefficents are updated once and stored using the solution of the previous time step, and the resulting linear algebraic equations are solved by a fixed number of two sweep Gaussian-Seidel iterations. In our code, about ten to twenty Gauss-Seidel iterations are used to find an approximate solution. The choice of the number of iteration corresponds to optimized overall convergence speed for some sliders. The multi-grid technique in Chapter 5 is used to speed up the convergence rate. Figure 6.3 shows the multi-grid V cycles

6.7 Results and Discussion

Figures 6.4 and 6.5 depict the slider used in the IBM Travelstar 25 Gbit hard disk drive. The length and width in the figures have been normalized by the dimensional length (1mm). Figures 6.6, 6.7 and 6.8 show one set of three initial meshes for the IBM slider. Figure 6.9 shows one adaptively refined third level mesh. Figure 6.10 shows the comparison of the convergence history of the iterations on a single set of mesh and the multi-grid iteration. The 'S' at the legend end represents the iteration on a single set of mesh, while the 'M' represents multi-grid iteration. The convergence difference among different schemes is very small, and it is almost undetectable for the single mesh iteration from the figure. Pat2 is the Patankar scheme extended to triangular mesh in Chapter 4. The sudden error jump in the figure corresponds to mesh adaptation. From the figure it can be seen that for the single mesh iteration, the error initially drops very fast, only ten iterations are needed to bring the error down from about 10^{-2} to 10^{-4}. But after the high frequency error has been smoothed out, the curve flattens. It takes about another 140 iterations to further reduce the error by about two orders of magnitude. The multi-grid curve shows that all error components can be continually and efficently removed. The log error drops almost linearly with the number of iterations (time steps). The figure also shows the multi-grid technique works well for all the schemes on the triangular mesh. For this particular slider only 20 multi-grid cycles are needed to get the converged solution. More than one order of magnitude simulation time is saved by use of the multi-grid technique.

Figures 6.11, 6.12, 6.13, 6.14 and 6.15 show the pressure contours at the steady state attitude obtained by the rectangular mesh solver (Lu, 1997) and the four triangular mesh

solvers, respectively. The disk is rotating at 4500 RPM, and the slider is located at a 15 mm radial position with zero skew angle. The prescribed suspension force is 1.5 g at the center of the slider, the prescribed suspension torque is zero. The pressure contours differ only by very small details. From the above figures we can see that all the regions with large geometric changes or pressure gradients have been efficiently captured by the mesh generation and adaptation techniques.

Figure 6.16 shows the flying height grid convergence comparison between the triangular mesh solvers and the rectangular mesh solver. The difference among the grid converged flying height solution of all the schemes is less than 1 nm. All schemes show a trend to converge to a 16 nm flying height. The PSI and SUPG schemes are less diffusive than the other schemes, which predict a slightly higher flying height. Figures 6.17 and 6.18 show the pitch angle and roll angle grid convergence histories respectively. For the node number corresponding to flying height convergence, all codes reach grid convergence. Figure 6.19 shows a plot of the simulation time for finding the steady state attitude as a function of the grid size. For the same number of node points, the triangular mesh solvers cost more time than the rectangular solver. But this is not always true. The rail shape of the IBM slider is extremely regular. In this case, the rectangular mesh solver is expected to do a good job. But the triangular mesh solvers will have a greater advantage than the rectangular mesh solver when the geometry becomes more complicated.

To demonstrate this, the NSIC slider (Fig. 6.20 and 6.21 with a characteristic length scale of 1 mm) is simulated. Figures 6.22, 6.23, 6.24 and 6.25 show one set of meshes used in the multi-grid iteration. Figure 6.26 shows the convergence history. The disk is

rotating at 7200 RPM, and the slider is located at a 15 mm radial position with a -1.22 $mRad$ skew angle. The prescribed suspension force is 1.5 g at the center of the slider, the prescribed suspension torque is zero. Figure 6.26 shows the grid convergence history, again the multi-grid technique greatly improved the convergence. Only 7 multi-grid cycles are needed to achieve convergence. Figures 6.27, 6.28, 6.29, 6.30 and 6.31 show the pressure contours corresponding to steady state flying height for the different schemes. Figure 6.32 shows the flying height grid convergence comparison between the triangular mesh solvers and the rectangular mesh solver. The PSI and SUPG predict a grid converged flying height around 8 nm, while the other schemes predict a flying height around 7 nm, but all of them still have a trend to fly higher with more grid points added. This clearly shows that the PSI and the SUPG scheme introduce less numerical diffusive effects than the other schemes and are assumed to be more accurate. Figure 6.33 and 6.34 are the grid convergence history for the pitch and roll angles respectively. Figure 6.35 shows the simulation time used to find the steady state flying attitude as a function of node number. This time, at the beginning, when the node number is the same, the triangular mesh solver uses almost the same or less time as the rectangular mesh solver. When the grid number increases, the times needed by the PSI and the SUPG schemes increase faster than by the rectangular mesh solver. But this is due to the nature of the non-nested multi-grid technique we used. The current technique does not require any relationship between the different mesh levels, however the relationship has influence on the performance of the multi-grid iteration. The mesh relationship is decided by several control parameters in our grid generation process. These parameters are optimized to the grid size in the beginning range. When a grid size is far out of that range, a new set of

parameters is needed to give optimized performance. Nevertheless from the above grid convergence figures, we can see that, the PSI and the SUPG schemes achieve grid convergence within that range for sliders as complicated as the IBM and the NSIC sliders.

Figure 6.36 shows the steady state flying heights of the NSIC slider at three radial positions obtained by the five numerical schemes and the preliminary experiments of NSIC. The results predicted by all numerical schemes are quite close to the experimental data. For this particular slider, all other schemes except the PSI and SUPG schemes have a tendency of under-predicting the flying height. We believe this is due to the more diffusive nature of these schemes compared with the PSI and SUPG schemes.

6.8 Summary and Conclusions

Three different schemes are used to discretize the convection part of the generalized Reynolds equation on unstructured triangular mesh, and a Galerkin finite element approach is used to model the diffusion part of the equation. The resulting numerical schemes are shown to be unconditionally stable. A non-nested FAS multi-grid algorithm has been successfully employed to speed up the convergence rate of the above schemes. To get comparable results the PSI and the SUPG triangular mesh solvers are generally four to five times faster depending on the complexity of the rail shape, due to the much improved grid point position strategy and the increased accuracy of the scheme.

Among the schemes, the PSI and the SUPG schemes are the most accurate and achieve grid convergence at the smallest node number.
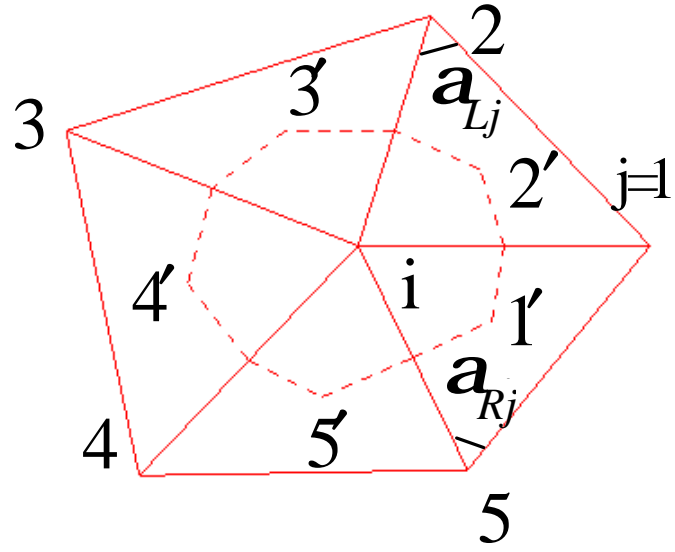
Fig. 6.1 The median dual control volume.
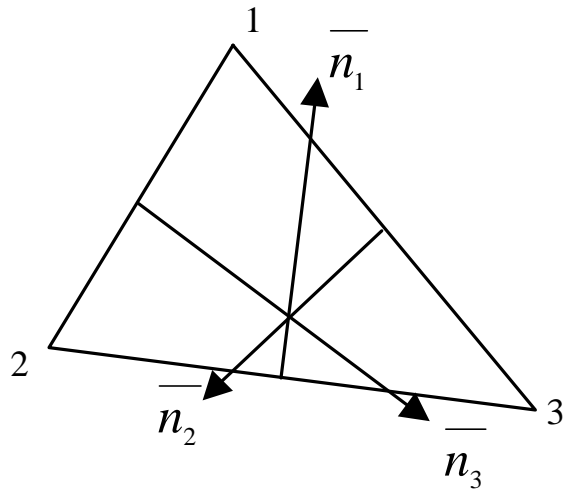
Fig. 6.2 The inward normals of a triangle.
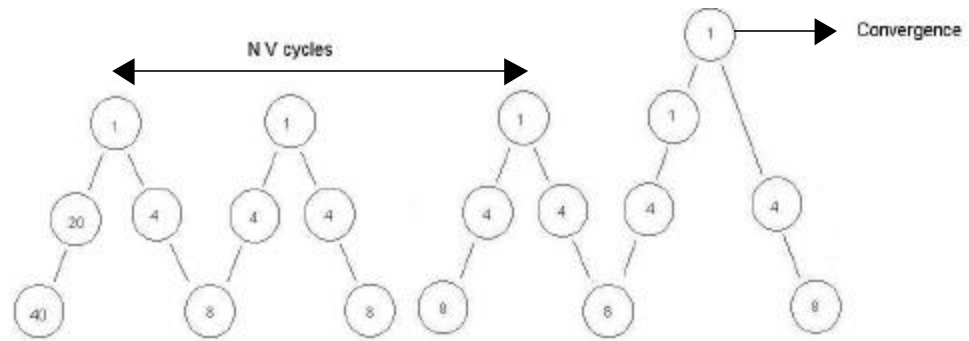
Fig. 6.3 The muti-grid V cycles.
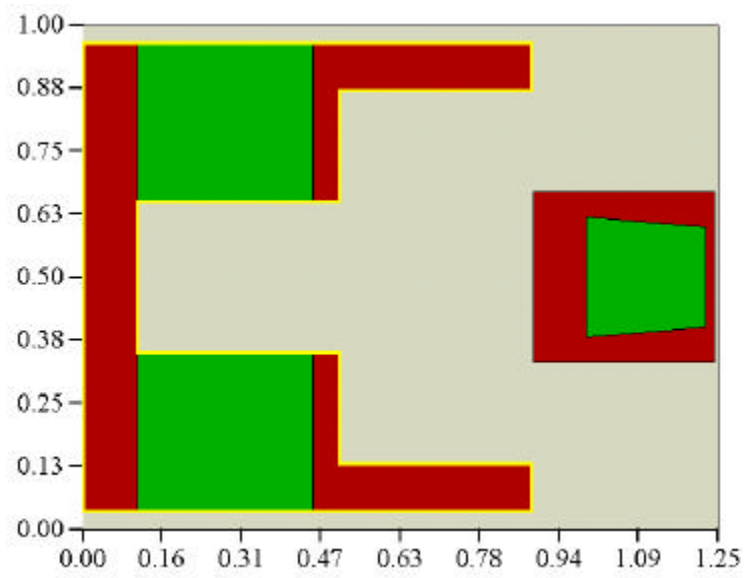
Fig. 6.4 A slider design close to the one used in the IBM Travelstar hard disk drive.
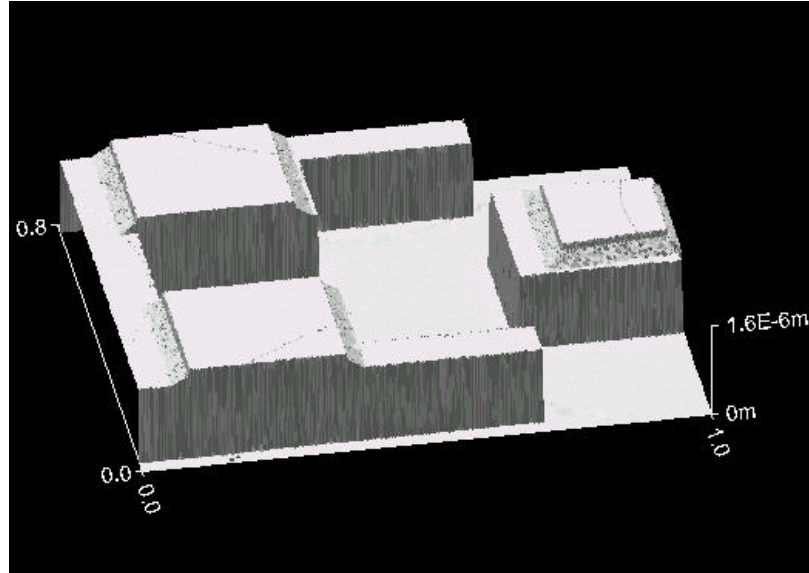
Fig. 6.5 The 3-D gometry of the IBM Travelstar slider.
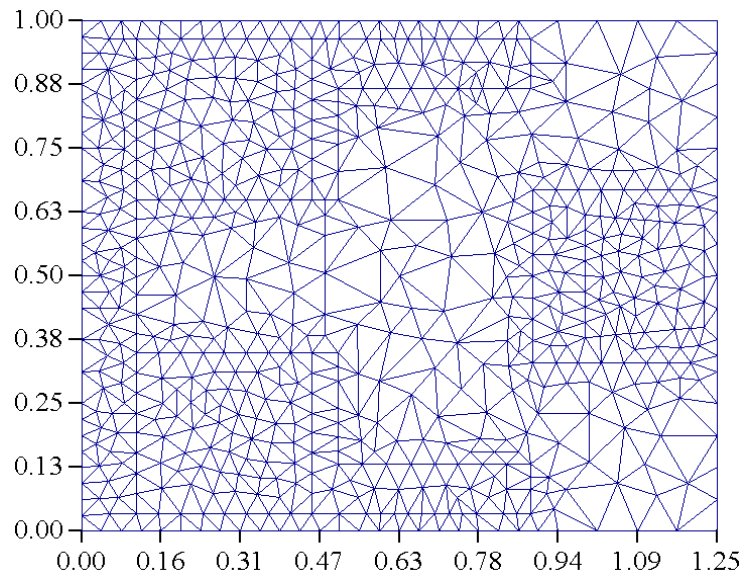
Fig. 6.6 The first level conforming meshes with 659 nodes
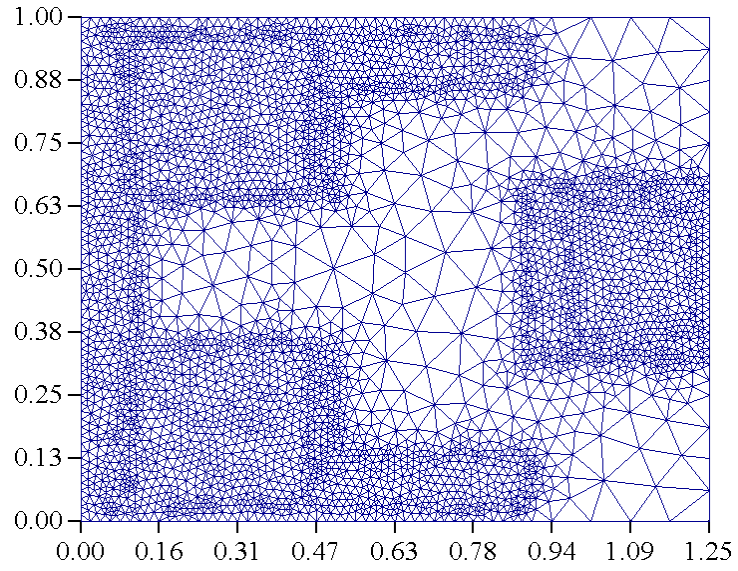
Fig. 6.7 The second level meshes with 4099 nodes.
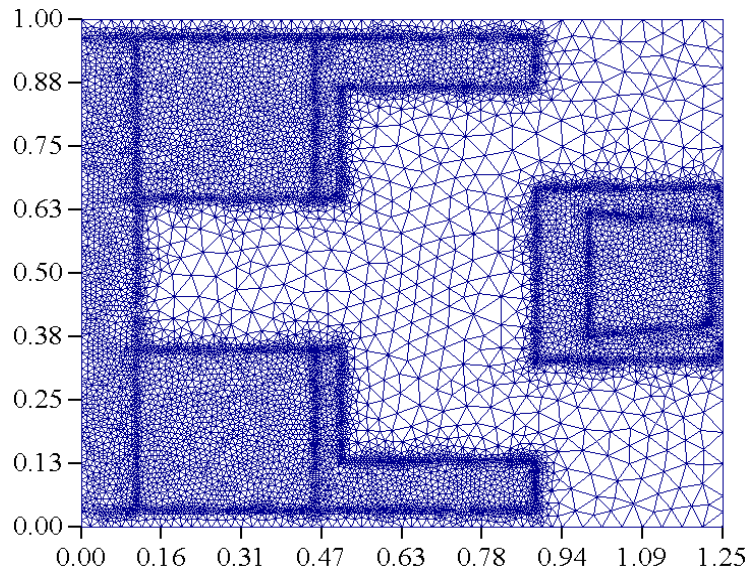
Fig. 6.8 The third level meshes before mesh adaptation with 12636 nodes.
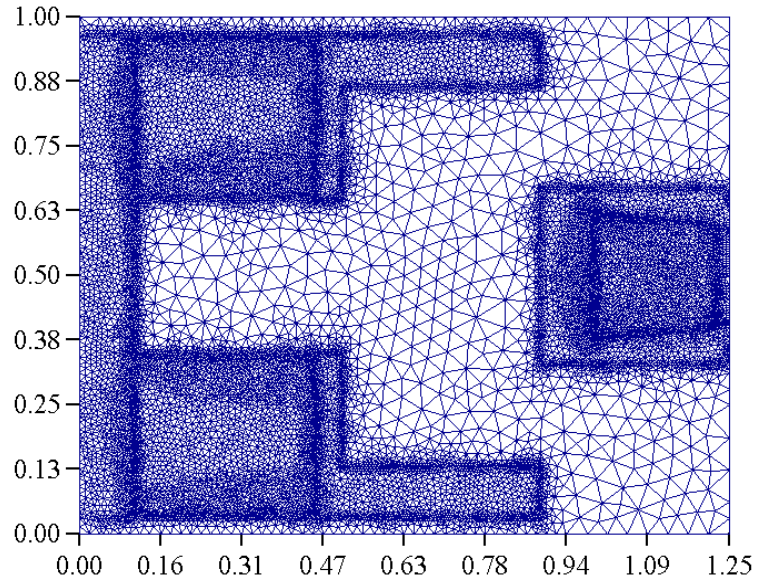
Fig. 6.9 The third level meshes after mesh adaptation with 18140 nodes.
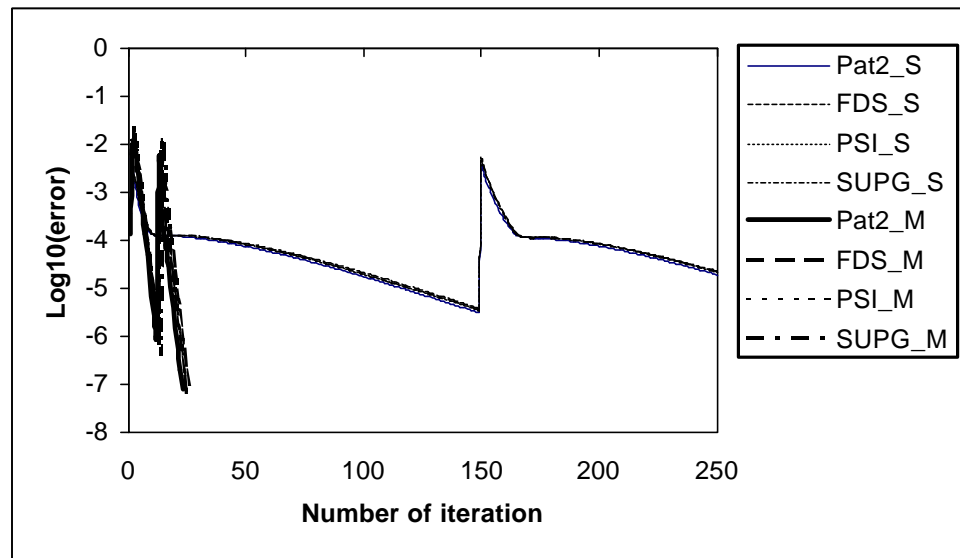
Fig. 6.10 The convergence history comparison between the iteration on a single set of

mesh and that of the multi-grid iteration for different schemes for one fixed flying

attitude .
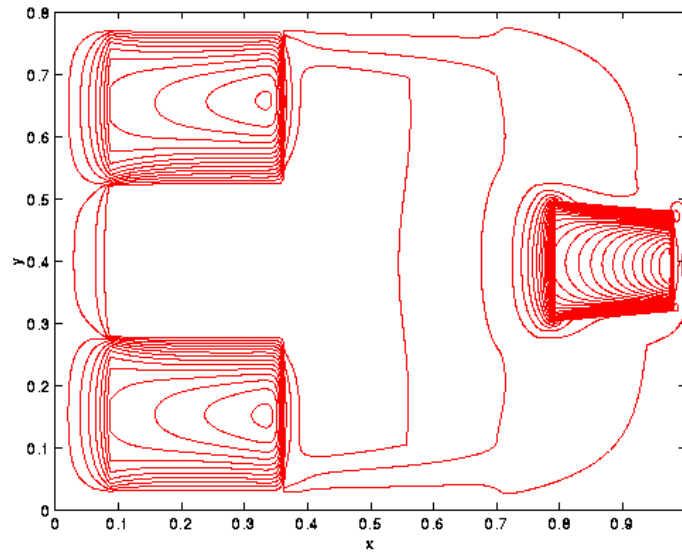
Fig. 6.11 The pressure contour for the steady state flying height at the 15mm radial position calculated by the rectangular mesh Patankar scheme of Lu (1997) with a 385 by 385 mesh.
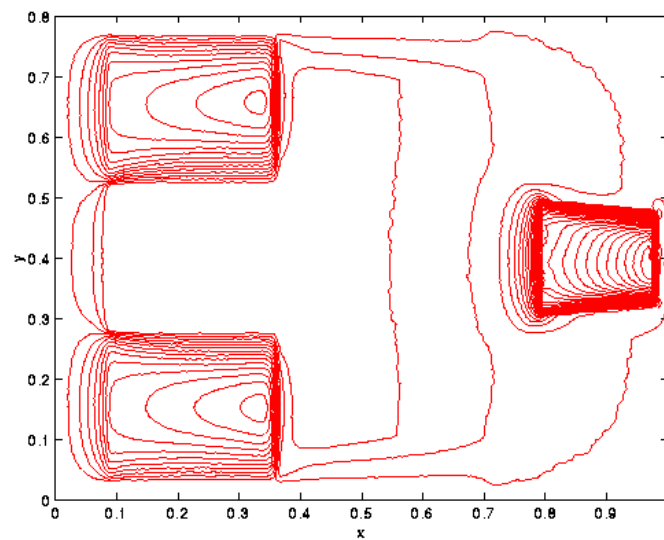
Fig. 6.12 The pressure contour calculated by the Patankar scheme extended to a triangular mesh (Chapter 4) with 18140 nodes for the finest level mesh.
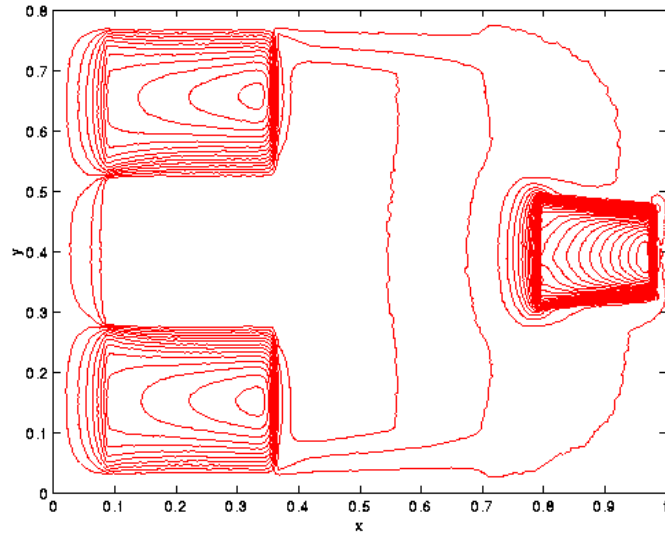
Fig. 6.13 The pressure contour calculated by the present FDS scheme with 18140 nodes
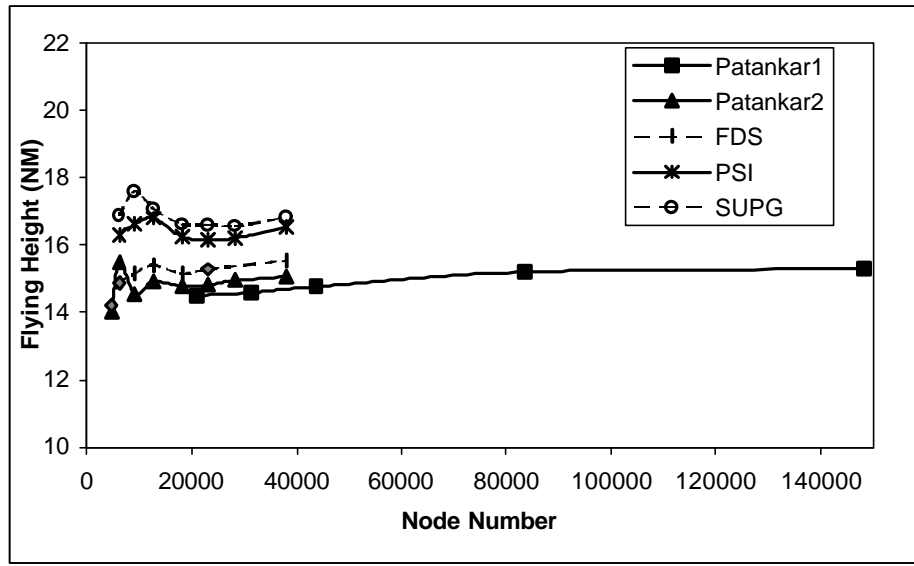
for the finest level mesh.
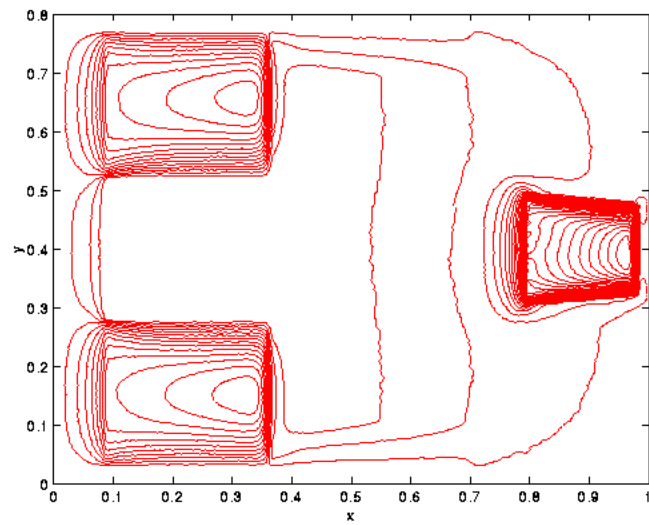
Fig. 6.14 The pressure contour calculated by the present PSI scheme with 18138 nodes

for the finest level mesh.
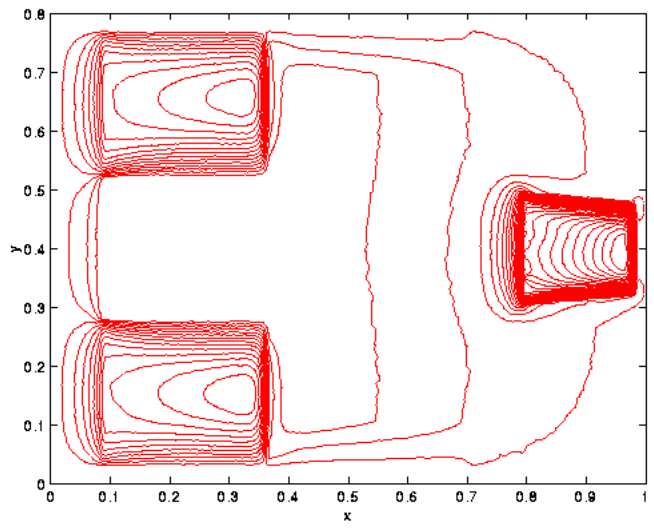
Fig. 6.15 The pressure contour calculated by the present SUPG scheme with 18137 nodes

for the finest level mesh.

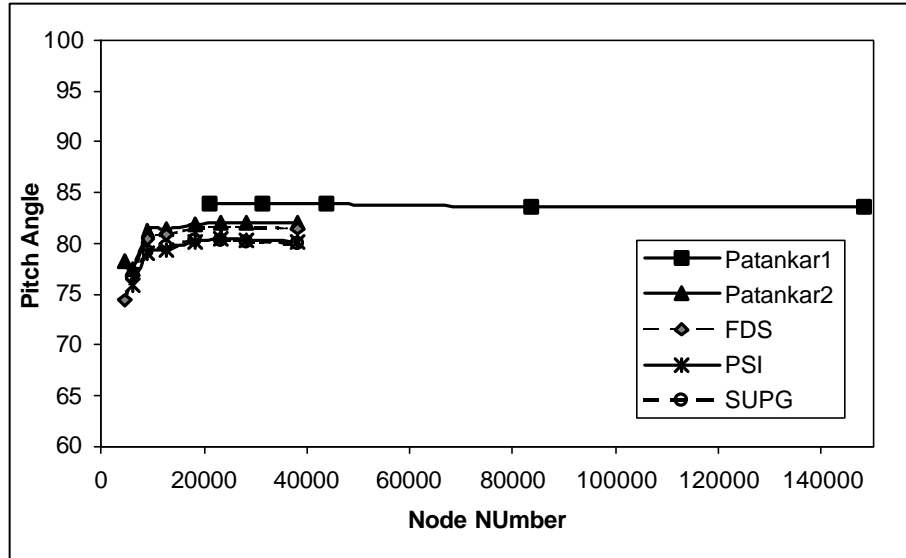**Fig. 6.16** The grid convergence history of nominal flying height for the different

schemes.

Fig. 6.17 The grid convergence history of the pitch angle ($mRad$) for difference
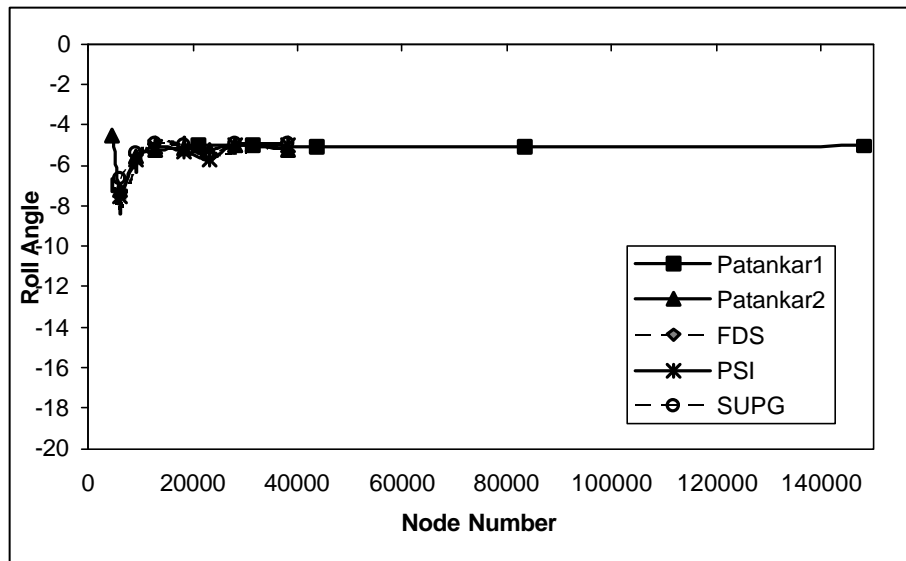
schemes.

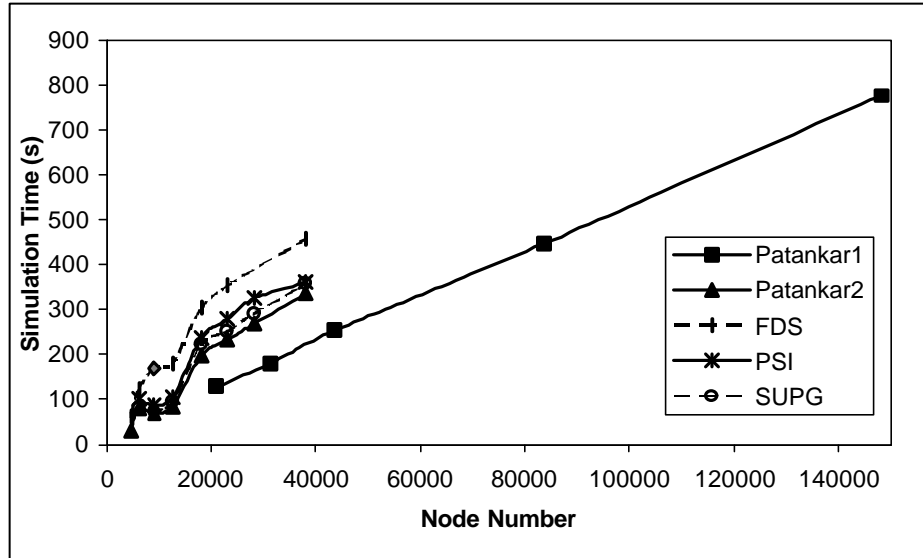**Fig. 6.18** The grid convergence history of the roll angle ($mRad$) for difference schemes.

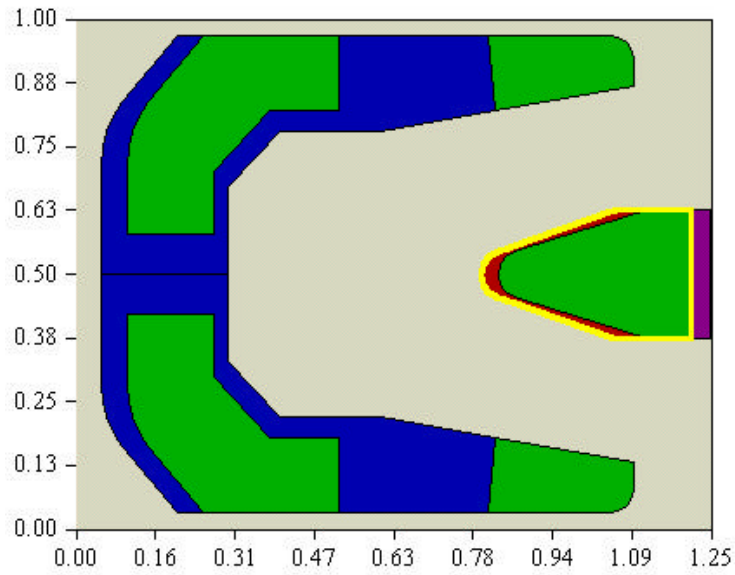**Fig. 6.19** The simulation time on a PII 350 PC as a function of node number.

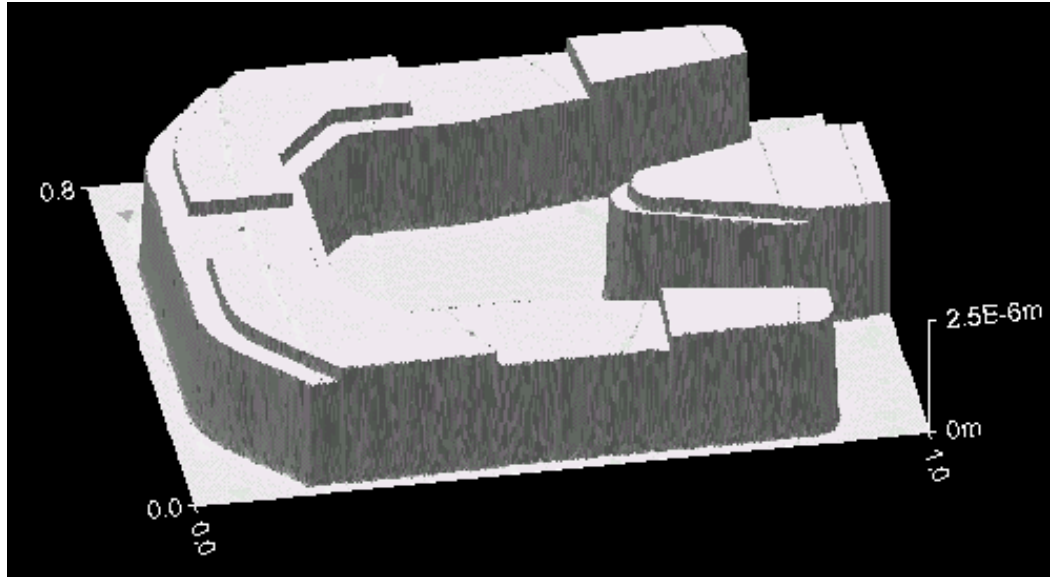**Fig. 6.20** The next generation NSIC slider design.
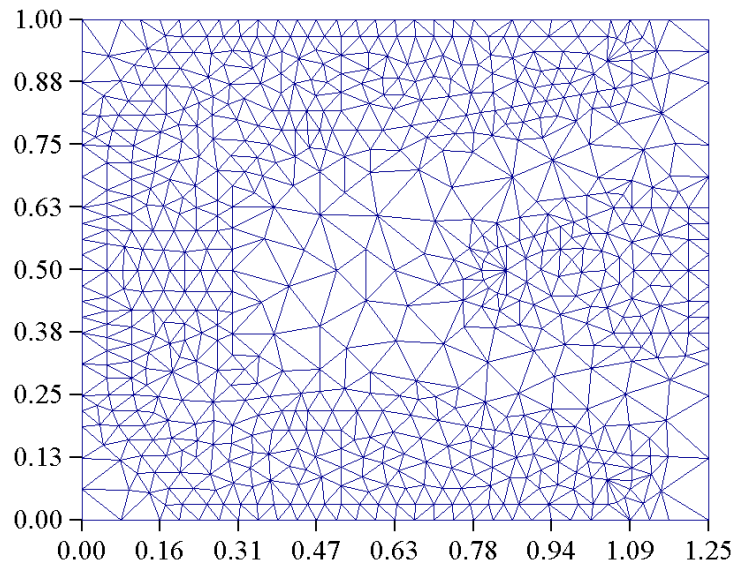
Fig. 6.21 The 3-D geometry of the NSIC slider.

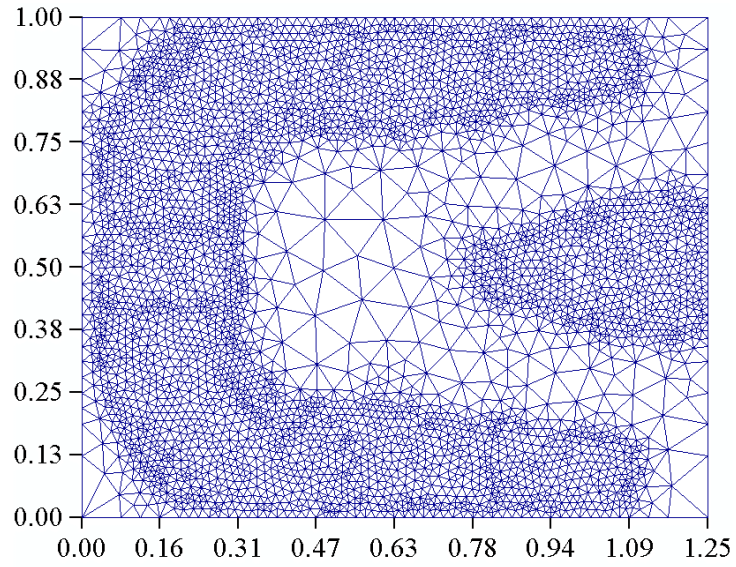**Fig. 6.22** The first level conforming meshes with 717 nodes

125

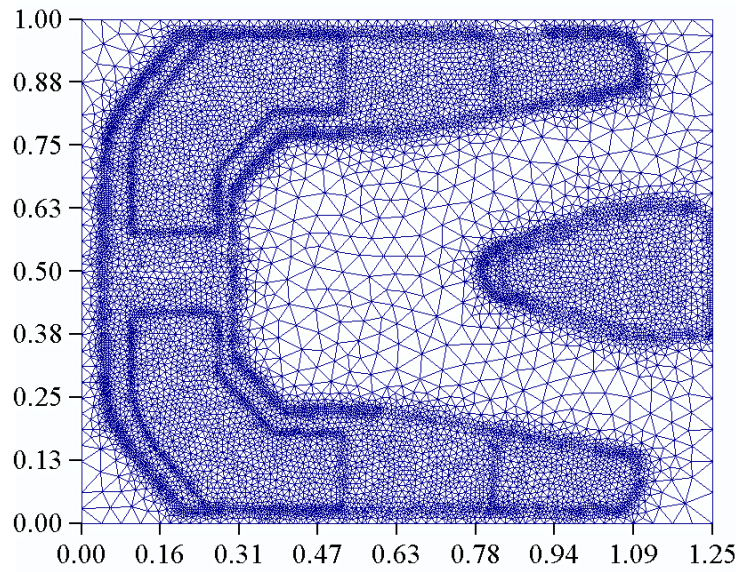**Fig. 6.23** The second level meshes with 4245 nodes.

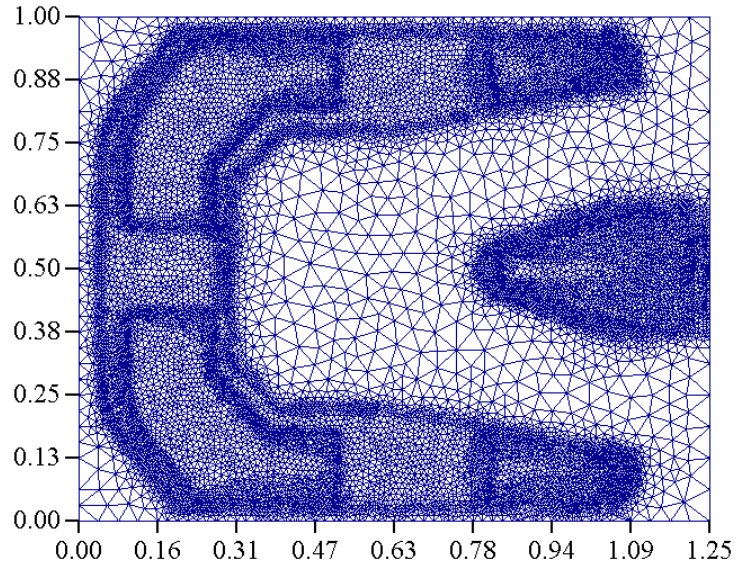**Fig. 6.24** The third level meshes before mesh adaptation with 12612 nodes.

Fig. 6.25 The third level meshes after mesh adaptation with 18112 nodes.
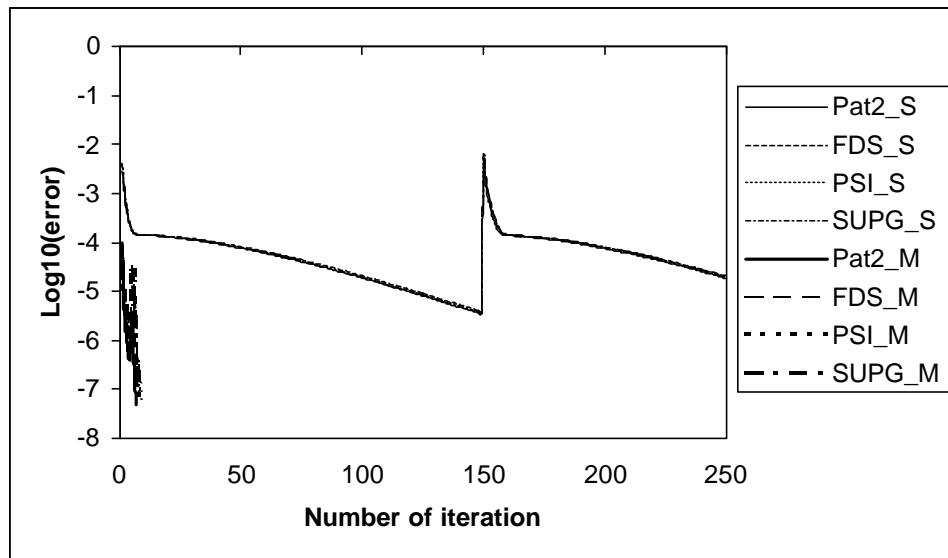
Fig. 6.26 The convergence history comparison between the iteration on a single set of

mesh and that of the multi-grid iteration for different schemes.
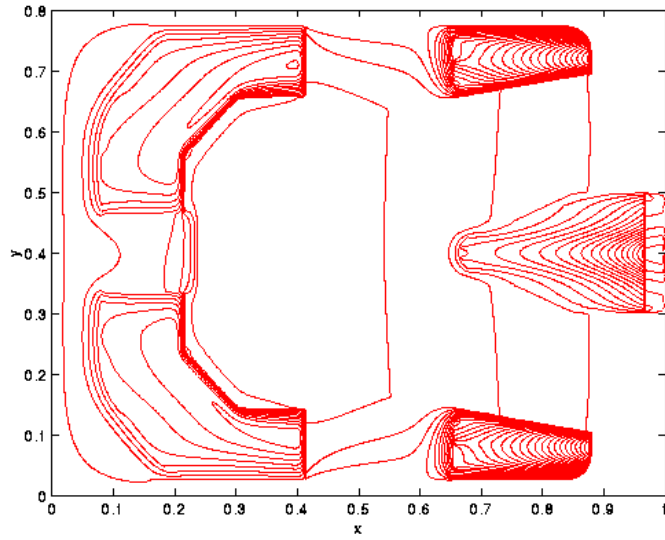
Fig. 6.27 The pressure contour for the steady state flying height at the 15mm radial

position, calculated by the Patankar scheme with a 385 by 385 mesh.
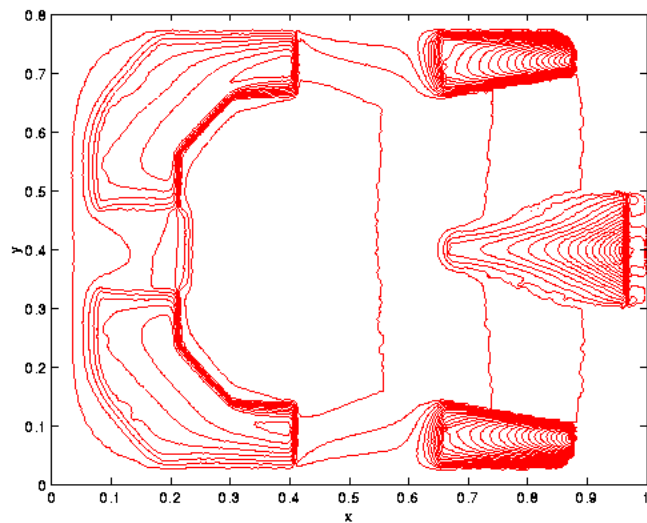
Fig. 6.28 The pressure contour calculated by the Patankar scheme extended to a

triangular mesh with 18112 nodes for the finest level mesh.

128
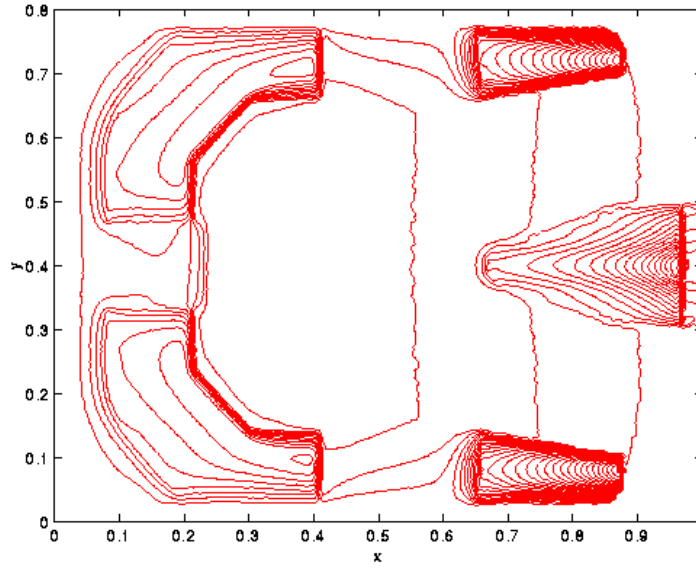
Fig. 6.29 The pressure contour calculated by the FDS scheme with 18111 nodes for the

finest level mesh.
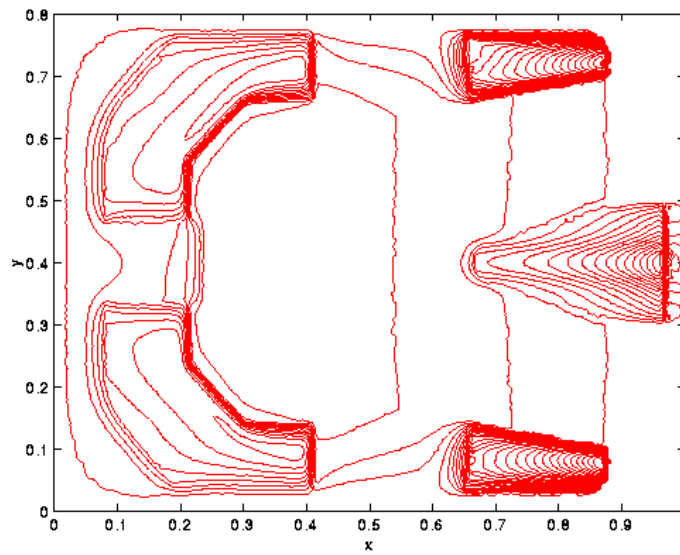
Fig. 6.30 The pressure contour calculated by the PSI scheme with 18110 nodes for the
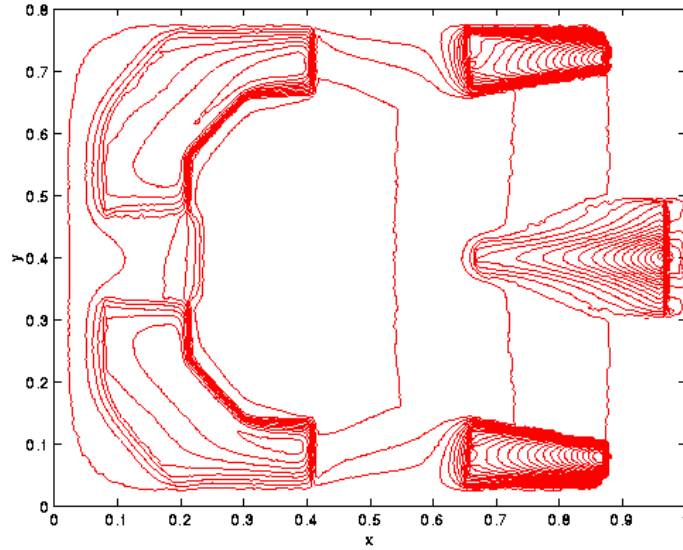
finest level mesh.

Fig. 6.31 The pressure contour calculated by the SUPG scheme with 18110 nodes for the

finest level mesh.
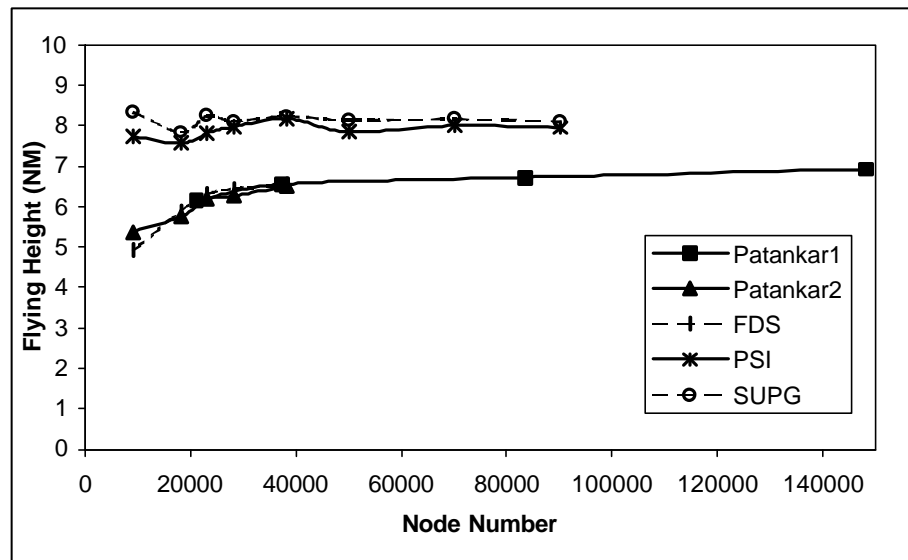
Fig. 6.32 The grid convergence history of nominal flying height for different schemes.
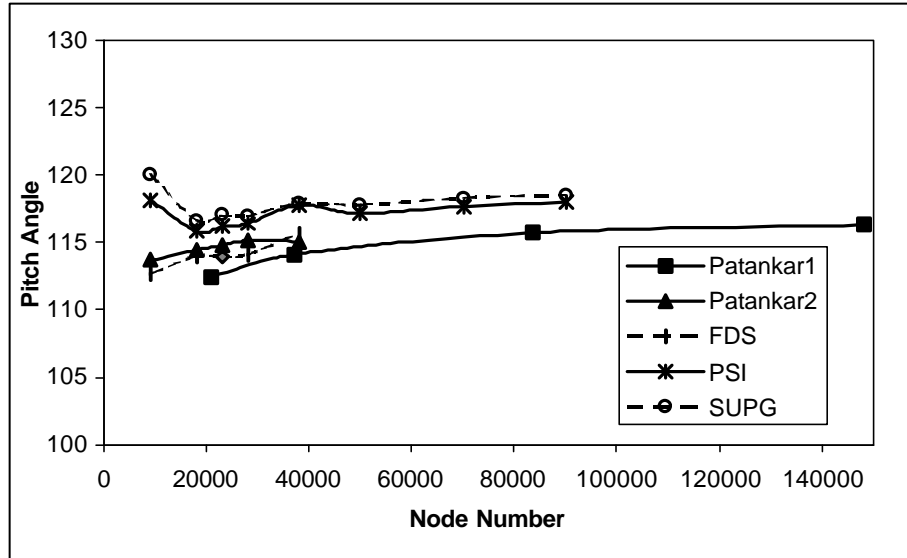
Fig. 6.33 The grid convergence history of the pitch angle ($mRad$) for difference
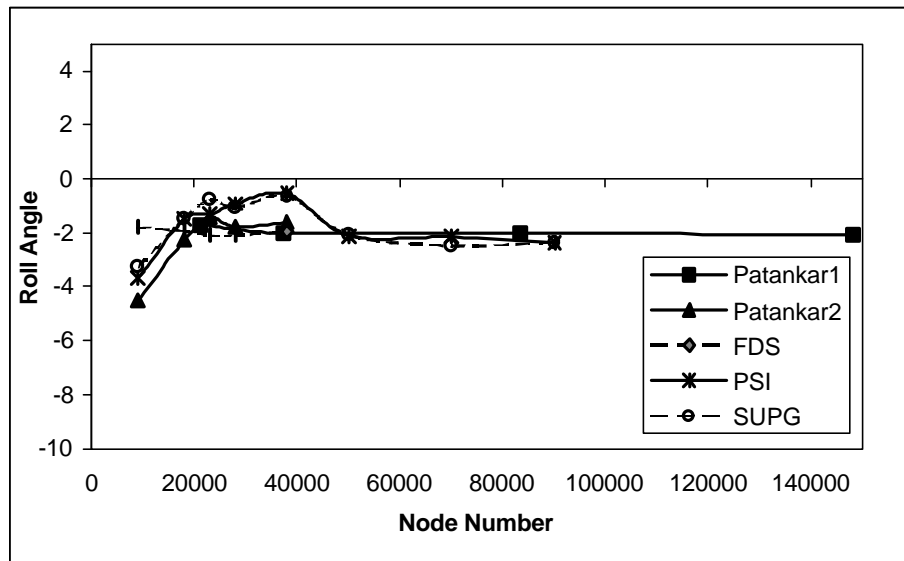
schemes.

Fig. 6.34 The grid convergence history of the roll angle ($mRad$) for difference schemes.
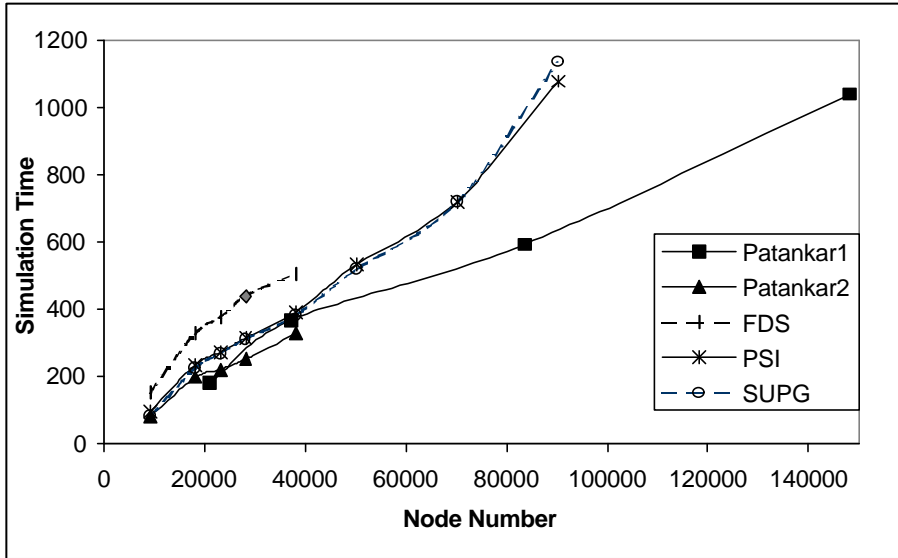
Fig. 6.35 The simulation time on a PII 350 PC as a function of node number.
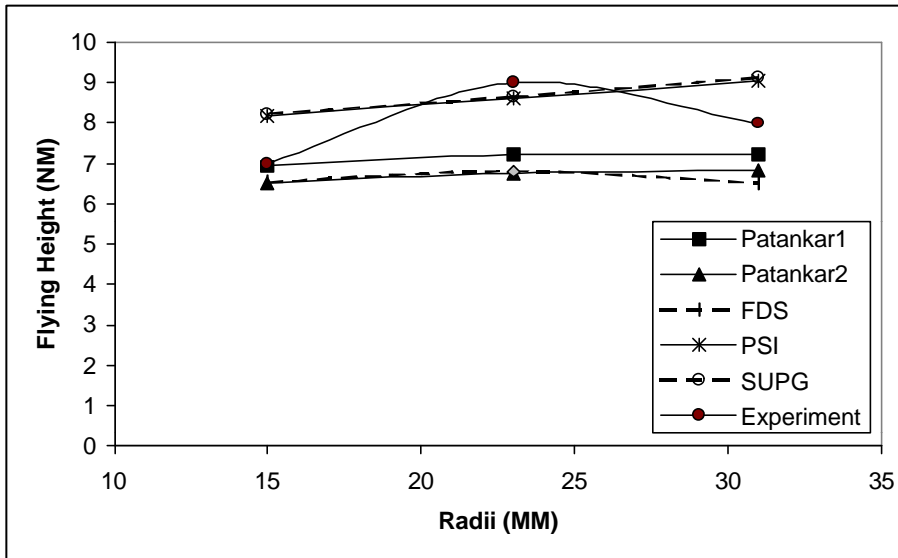
Fig. 6.36 The flying height at different radial position for the NSIC slider.

CHAPTER 7

EFFECT OF THE INTERMOLECULAR FORCES ON THE FLYING

ATTITUDE OF SUB-5 NM FLYING HEIGHT AIR BEARING SLIDERS

7.1 Introduction

Traditionally, the flying attitude of the slider (including the flying height, the pitch and roll angle) is determined by the balance of force and moments contributed from the pre-load of the suspension and the air bearing pressure and shear. The pre-load force and moments from the suspension are assumed to be known. Most studies of air bearing simulations are concerned with the modifications of the Reynolds lubrication equation in order to get reasonably accurate predictions of the air bearing pressure field under rarefied conditions and also the numerical methods that can solve this equation efficiently. To increase the areal density to the range of 1 Tbit/in^2, a flying height around 3nm is believed to be necessary. At such a low spacing, additional physical phenomena that are not important and have been ignored when the slider flies above 10 nm become increasingly more important and may no longer be negligible. For example, the intermolecular forces between the two solid surfaces of the slider and the disk make them attract each other when the distance is less than 10 nm and repel each other at sufficiently small spacing. These forces participate in the balancing process and may have an important influence on the flying attitude of the slider, both statically and dynamically.

For a slider with a flying height around 0.4 to 5 nm, among these forces, the long range attractive van der Waals force is the dominant one, which has an effective range

from 0.2 nm to a distance greater than 10 nm. It is contributed mostly from the dispersion force between two atoms, which is induced by the fluctuations in their electric dipoles. The instantaneous positions of the electrons around an atom generate a finite dipole moment, even though the time average is zero. The electric field generated by the finite dipole moment of one atom also induces a dipole moment in the other atom. This makes the two atoms attract each other. A detailed explanation and theory can be found in Israelachvili (1992).

A previous preliminary investigation using a simplified geometry showed that the van der Waals force changed the load capacity significantly when the bearing spacing is low enough (Zhang and Nakajima, 2000). For a positive pressure flat surface slider with zero roll angle, these authors numerically showed that the van der Waals force causes a lower limit clearance of a few nano-meters, below which the load capacity becomes negative. This clearance limit decreases with the pitch angle (Zhang and Nakajima, 2000). They did not investigate the effect of the van der Waals force on the slider's flying attitude and they ignored the repulsive portion of the intermolecular force. When the spacing is extremely low, this portion of the intermolecular force needs to be included; otherwise the slider would never take off, because at actual contact the purely attractive van der Waals force is extremely large. In addition, to fully understand its effect on the design goal in hard disk drives, more practical and complicated sliders need to be examined, including negative pressure sliders. Since the load capacity of negative pressure sliders is quite different from that of the positive pressure slider, we expect different results or trends between them.

Here we extend the investigation in Zhang and Nakajima (2000) by first formulating the total intermolecular force between an infinite plate and a triangular cell of material of the slider that has a relatively large vertical thickness compared to the acting range of the forces and is oriented in 3-D space. The 3-D air bearing surface is then meshed into triangles. The total force and the pitch and roll angle moment contributions from the intermolecular forces between the slider and the disk surface are calculated and incorporated into the steady state air bearing design code developed in Chapters 4,5 and 6. The intermolecular force effects on the load capacity and flying attitude are demonstrated for particular examples of a positive pressure Tripad slider and a negative pressure Femto slider.

7.2 the Intermolecular Force Between the Slider and the Disk

When two atoms are brought close enough, they start to experience the existence of each other in the form of intermolecular forces. At the beginning, it is an attraction force, and its strength increases with decreasing distance until a maximum point is reached, then it decreases with decreasing distance. When the distance is reduced further, the force becomes repulsive and increasingly stronger. This is reflected in Fig. 7.1, which shows the potential energy between two atoms as a function of their distance. One expression used to describe this potential is the so called Lennard-Jones potential, in which the attractive van der Waals potential is modeled as an inverse sixth power term and the repulsive potential is modeled as a inverse twelfth power term

$$w = -\frac{C}{r^6} + \frac{D}{r^{12}}, \qquad (7.1)$$

where $C = 10^{-77}\, Jm^6$ and $D = 10^{-134}\, Jm^{12}$ are two constants for atoms in vacuum (Israelachvili ,1992). For sliders flying with a few nano-meters spacing, the repulsive potential term can be ignored, and we obtain the purely van der Waals potential

$$w = -\frac{C}{r^6}. \qquad (7.2)$$

Equation (7.1) is the potential between two atoms, and it can be integrated over an infinitely long and infinitely deep half space to obtain the potential between an atom and an infinite plate,

$$W = -\frac{\boldsymbol{p} C \boldsymbol{r}_1}{6h^3} + \frac{\boldsymbol{p} D \boldsymbol{r}_1}{45h^9}, \qquad (7.3)$$

where $\boldsymbol{r}_1$ is the number density of atoms in the infinite plate, and h is the distance between the atom and the plate. Equation (7.3) can be integrated over a volume of material within the slider, which has a triangular intersection area with the air bearing surface, to obtain the total interaction potential between the volume of material of the slider and the infinite plate

$$W_v = -\frac{pCr_1r_2}{6} \iint\limits_\Delta dxdy \int_h^\infty \frac{1}{z^3}dz + \frac{pDr_1r_2}{45} \iint\limits_\Delta dxdy \int_h^\infty \frac{1}{z^9}dz, \qquad (7.4)$$

where r_2 is the number density of atoms within the slider. In Eqs. (7.3) and (7.4), to simplify the problem, the depth of the plate and the thickness of the slider have been taken to be infinite. This is justified, since the actual depth of the plate and the thickness of the slider are several orders larger than the acting range of the intermolecular force. By defining the Hamaker constant as $A = p^2Cr_1r_2$ and another constant $B = p^2Dr_1r_2$ and carrying out the integration in the z direction, we obtain

$$W_v = -\frac{A}{12p} \iint\limits_\Delta \frac{1}{h(x, y)^2} dxdy + \frac{B}{360p} \iint\limits_\Delta \frac{1}{h(x, y)^8} dxdy. \qquad (7.5)$$

To obtain the intermolecular force between each triangular volume of material of the slider and the plate, we need to differentiate the potential of Eq. (7.5) in the direction perpendicular to the plate. After that, the intermolecular force between each triangular cell and the disk can be written as

$$F_v = \frac{dW_v}{dz} = \frac{A}{6p} \iint\limits_\Delta \frac{dxdy}{h^3} - \frac{B}{45p} \iint\limits_\Delta \frac{dxdy}{h^9}. \qquad (7.6)$$

The first term on the right hand side of Eq. (7.6) is the attractive van der Waals force, and the second term is the repulsive intermolecular force. The attractive and repulsive portions of the force have different acting ranges. The attractive van der Waals force has

a much longer acting range than the repulsive portion. The two solid surfaces first experience the attraction force when the distance between them is less than about 10nm. The strength of the attractive force increases with the reduction of the spacing until the spacing becomes small enough such that the short range repulsive force becomes active. We can roughly estimate the acting range of the repulsive intermolecular force by equating the attraction potential and the repulsive potential in equation (7.1)

$$\frac{C}{r^6} \sim \frac{D}{r^{12}}. \tag{7.7}$$

The above equation gives

$$r \sim \left(\frac{D}{C}\right)^{\frac{1}{6}} \approx 0.32 \ nm. \tag{7.8}$$

This is roughly the spacing, below which the repulsive force can not be ignored.

7.3 Numerical Solution of the Balanced Steady State Attitude

The Quasi-Newton iteration method for non-linear problems, described in Dennis and Schnabel (1983), is implemented to find the steady state flying attitude. We can define an objective vector $\underline{R} = (R_1, R_2, R_3)$ with

$$R_1 = F_{air} - F_s - F_v, \qquad (7.9)$$

$$R_2 = \left(M_{air}\right)_p + \left(M_s\right)_p + \left(M_{shear}\right)_p + \left(M_v\right)_p, \qquad (7.10)$$

$$R_3 = \left(M_{air}\right)_r + \left(M_s\right)_r + \left(M_{shear}\right)_r + \left(M_v\right)_r, \qquad (7.11)$$

where F_{air} is the resultant air bearing force of a guessed flying attitude, F_s is the applied suspension force, F_v is the attractive van der Waals force, M_{air}, M_{shear}, M_s and M_v are moments caused by air bearing pressure, viscous shear force at the slider air bearing surface at that guessed attitude, the suspension and the van der Waals force, respectively. The air bearing contributions are found by numerically solving the Reynolds equation using the numerical methods developed in previous chapters   The suspension contributions are known.   The van der Waals force contributions are obtained by summing up the forces evaluated by Eq. (7.6) and its moments in each triangular cell. A 7-points quadrature (Fig. 7.2) is used to evaluate the integration in Eq. (7.6). The steady state attitude corresponding to null $\underline{R}$ is obtained by a few iterations.

7.4 Results

In the simulations, the Hamaker constant A is taken to be $10^{-19} J$ and the constant B is taken to be $10^{-76} Jm^6$, which are typical values for interactions between condensed phases across vacuum or air (the Hamaker constant is in the range 0.4-

$4 \times 10^{-19} J$ for most condensed phases) (Israelachvili, 1992). The first slider used to demonstrate the van der Waals force effect is the posititve pressure Tripad nano slider (Fig. 7.3) with a 3.5g force and zero moment pre-load from the suspension. The disk rotation speed is 5400 rpm. Figure 7.4 shows the different force contributions to the load as a function of the flying height at a fixed pitch angle of $150 mrad$ and zero roll angle. Without the van der Waals force, the total air bearing force curve coincides with the positive air bearing force curve, since the negative air bearing force is negligible for this design. The total load capacity increases with decreasing flying height. However, if the van der Waals force is included, the total load curve starts to deviate from the positive air bearing force curve at a flying height around 3 nm, which corresponds to the height at which the attractive van der Waals force becomes significant, and it no longer increases but instead decreases with decreasing flying height. Below 1 nm, the total load curve bends down and decreases rapidly. As the flying height is reduced further, it becomes negative, which means the slider can not sustain any load. The flying height corresponding to zero load capacity is what is called the low limit clearance in Zhang and Nakajima (2000). As a result, the van der Waals force changes the total load curve at flying heights below 3 nm. In Fig. 7.5, the different force contributions and the total loads have been ploted as functions of the pitch angle. The flying height is fixed at 0.45 nm, and the roll angle is zero. Without the van der Waals force, the total load curve coincides with the positive air bearing force curve and increases with decreasing pitch angle. But the attractive van der Waals force also increases with decreasing pitch angle. The net effect is an almost zero total load capacity at all pitch angles shown. Figure 7.6 shows the flying height of the Tripad slider at different radial positions. The van der

Waals force lowers the flying height from 4.73 nm to 3.71 nm at the inner radius (15 mm), which is a 21.6% reduction. At the outer radius, the difference is negligible, since the flying height is out of the acting range of the van der Waals force. Figure 7.7 shows the van der Waals force effect on the pitch angle of the Tripad slider at different radial positions. At the inner radius, the van der Waals force slightly increases the pitch angle. Again, it has negligible effect at the outer radius. Figure 7.8 shows that the van der Waals force has negligible effect on the roll angle.

Figure 7.9 shows a negative pressure Femto slider design for a 0.5g suspension force and zero moment suspension pre-load and a disk rotation speed of 7200 rpm. Figure 7.10 shows the force contributions to the total load as a function of the flying height. The pitch angle is held at $150\,mrad$, and the roll angle is zero. The negative air bearing force is almost constant with distance, so the total load increases with the positive air bearing force as the flying height is reduced, if the van der Waals force is not included. But when including of the van der Waals force, the total load curve starts to deviate from the curve without van der Waals force at a height of about 5 nm. Below 5 nm, the total load decreases slowly at the beginning, and then decreases rapidly and becomes negative when the flying height is reduced further. There is also a low limit clearance for this slider. Figure 7.11 shows the force contributions to the total load as a function of the pitch angle for the flying height fixed at 4 nm. The same trend as shown in the previous figure can be observed, if the pitch angle is switched with the flying height. Figure 7.12 shows the flying height of the Femto slider at different radial positions with and without the van der Waals force. The van der Waals force changes the flying height significantly, especially at the inner radius. It lowers the flying height from

4.14 nm to 3.14 nm at the inner radius, but only lowers it from 1.65 nm to 1.54 nm at the outer radius. This seems unusual, since at the outer radius the slider flies at lower flying height, so the van der Waals force should have a larger effect. But this particular design has a relatively large pad at the trailing edge, so its van der Waals force is more sensitive to the pitch angle than is the case for the Tripad slider, which has a small and short pad at the trailing edge. It is not difficult to understand that the lower flying height and smaller pitch angle make the van der Waals force stronger, since more material of the slider is brought closer to the disk surface. The Femto slider has a pitch angle of 326.1 $mrad$ at the outer radius versus a 142.4 $mrad$ pitch angle at the inner radius. This is shown in the Fig. 7.13. The much larger pitch angle effect surpasses the lower flying height effect at the outer radius, and the net result is a smaller van der Waals force effect on the flying height at the outer radius. Figure 7.13 also shows that the van der Waals force slightly increases the pitch angle at the inner radius. Figure 7.14 shows that the van der Waals force does not influence the roll angle very much.

Figure 7.15 shows the effect of the repulsive portion of the intermolecular force on the total force for the Tripad slider at a fixed pitch angle of $150 mrad$. At a flying height of about 0.35 nm, which is the place where the repulsive intermolecular force becomes non-negligible, both the total intermolecular force curve and the total force curve start to deviate from their counterparts with only the pure van der Waals force included. They increase rapidly and become positive (repulsive) after a minimum negative value has been reached, instead of continuing to decrease rapidly as was the case with only the van der Waals force included. Figure 7.16 shows the same trend for the Femto slider. This indicates that for sliders with a steady state flying height below

0.4~0.5 nm or having intermittent contact or near contact dynamic performance, the repulsive intermolecular force needs to be included.

7.5 Conclusions

The intermolecular forces have been incorporated into a steady state air bearing design code. Simulation results for two typical slider designs show that the van der Waals force has a significant effect on the total load capacity and flying height of both the positive and negative pressure sliders , when the sliders fly below 5 nm. It significantly lowers the flying height and slightly increases the pitch angle, but it has negligible effect on the roll angle. For sliders with relatively large rear pads, the van der Waals force effect is also sensitive to the pitch angle change, and it must be accounted for in the design code before an accurate flying attitude of the slider can be obtained. The results presented here also demonstrated the same phenomenon observed by other investigators, that the van der Waals force results in a lower limit clearance below which the slider can not sustain any load. This is totally different from the cases where the van der Waals force is not included. Our results also show that the repulsive portion of the intermolecular force needs to be included when the flying height is below 0.4~0.5 nm.
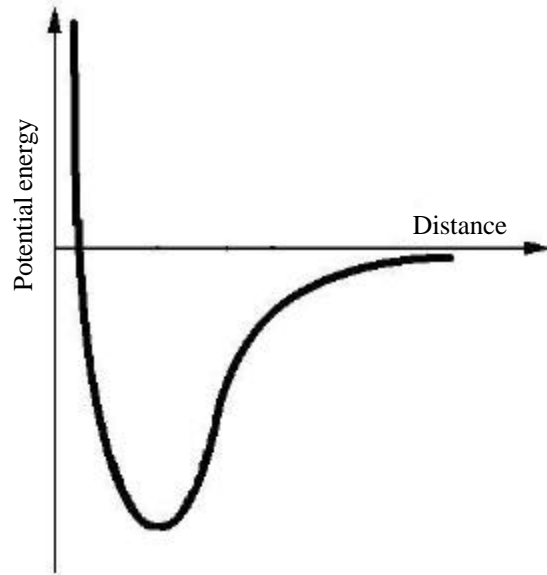
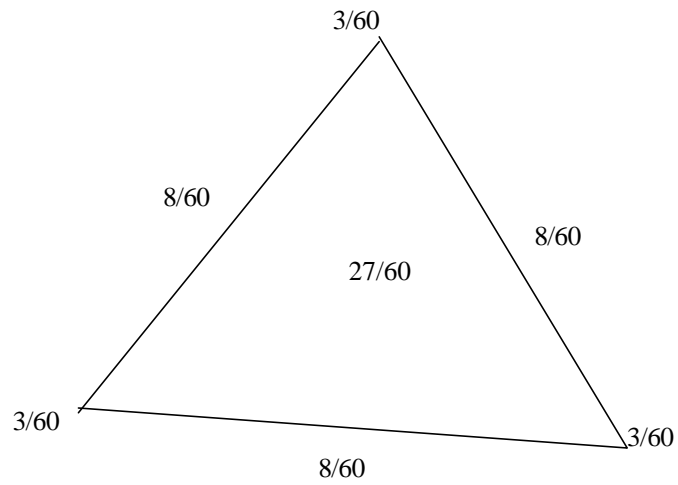**Fig. 7.1** The potential energy between two molecules.

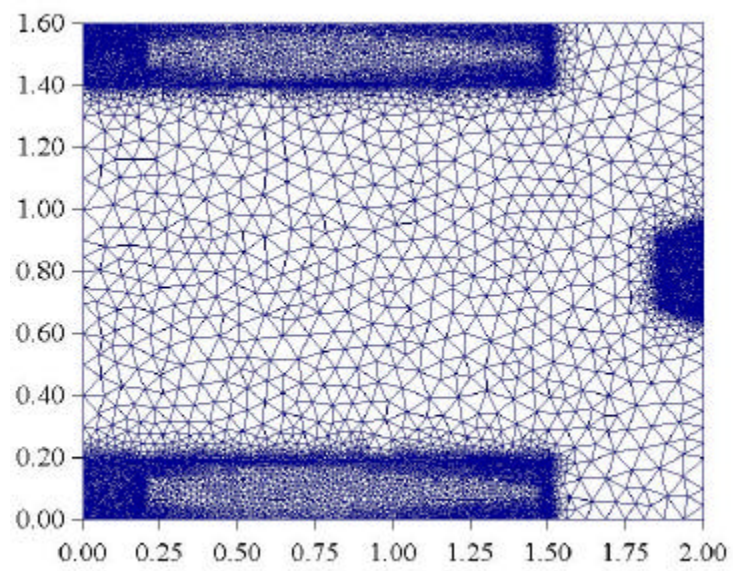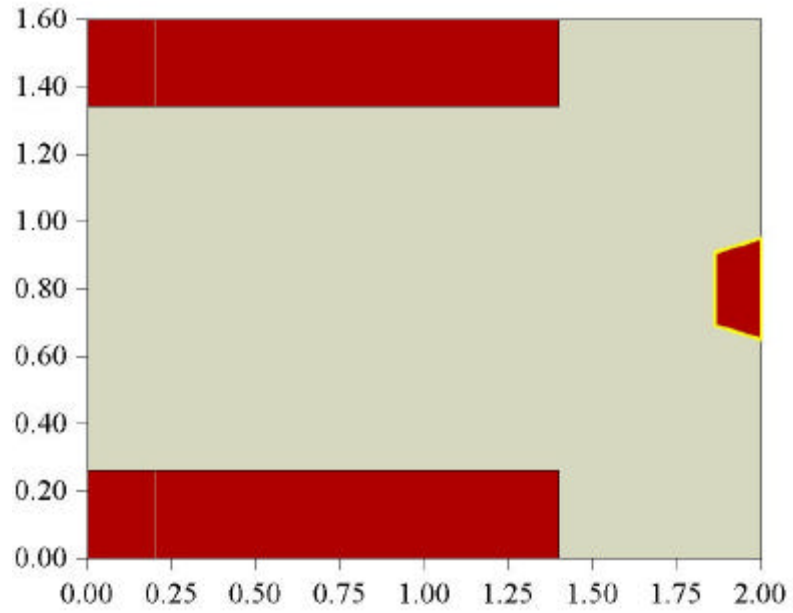**Fig. 7.2** The constants used in the 7 point quadrature.

Fig. 7.3 The Tripad positive pressure slider and the unstructured triangular meshes.
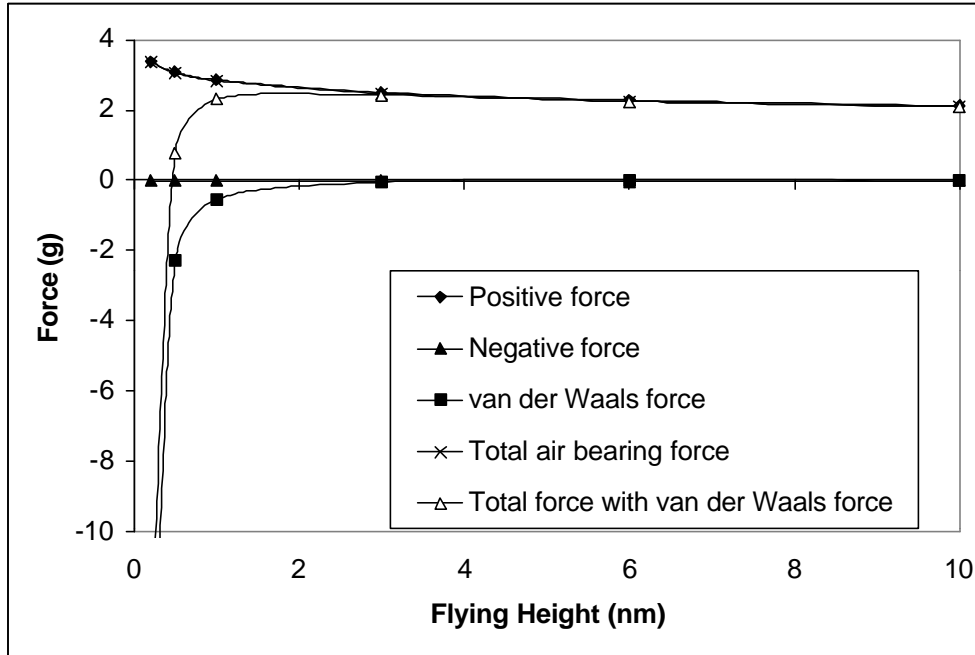
Fig. 7.4 Air bearing forces, the van der Waals force and the load capacity as a function of

the flying height for the Tripad slider at a fixed pitch angle of $150\,\boldsymbol{\mu}\mathit{rad}$.
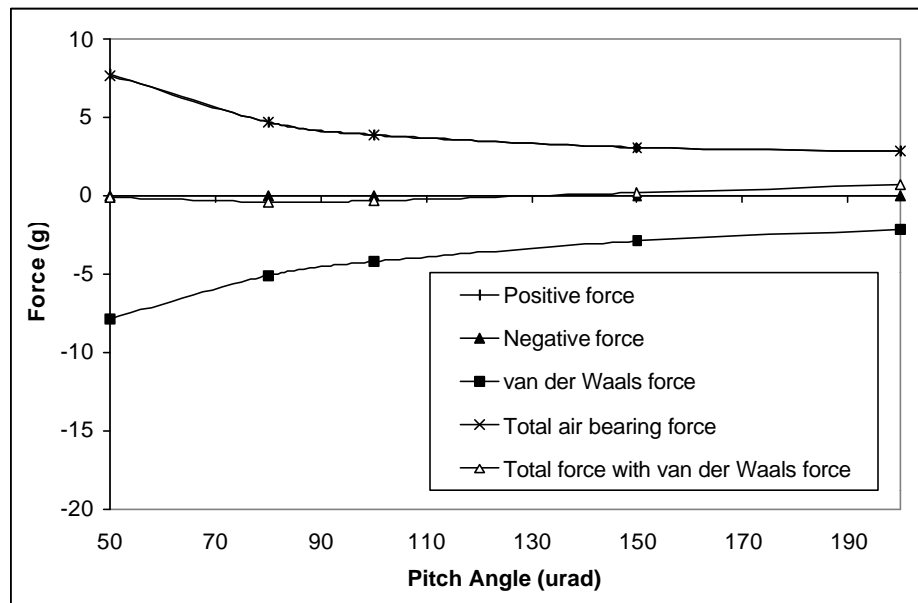

Fig. 7.5 Air bearing forces, the van der Waals force and the load capacity as a function of

the pitch angle for the Tripad slider at a fixed flying height of 0.45 nm.
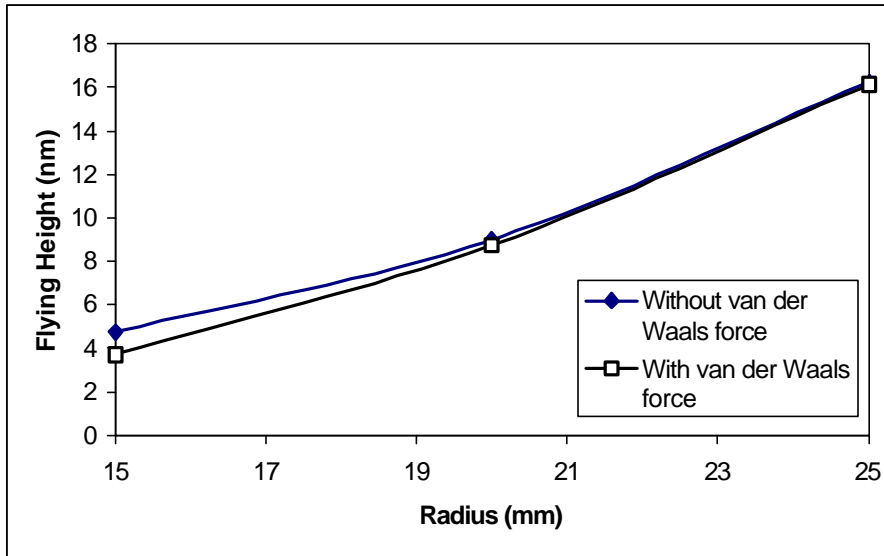
Fig. 7.6 The effect of the van der Waals force on the flying height of the Tripad slider at
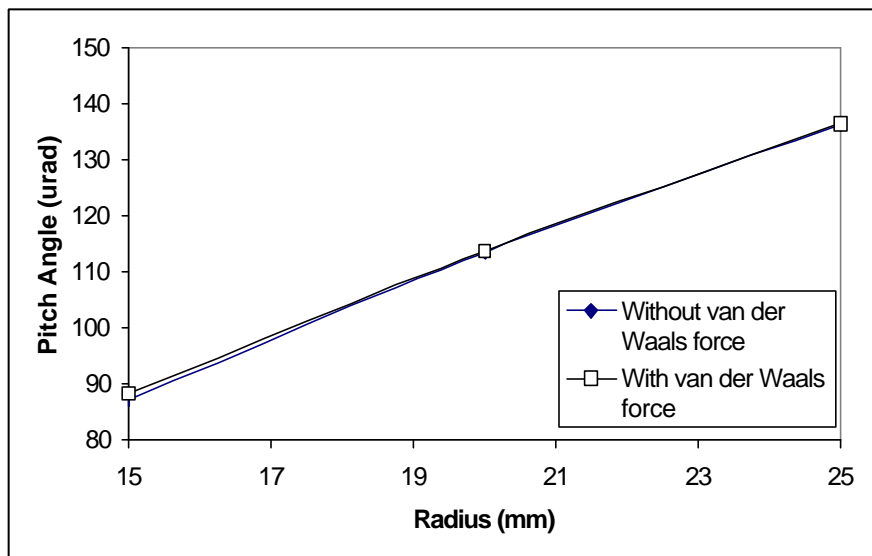
different radial positions.

Fig. 7.7 The effect of the van der Waals force on the pitch angle of the Tripad slider at
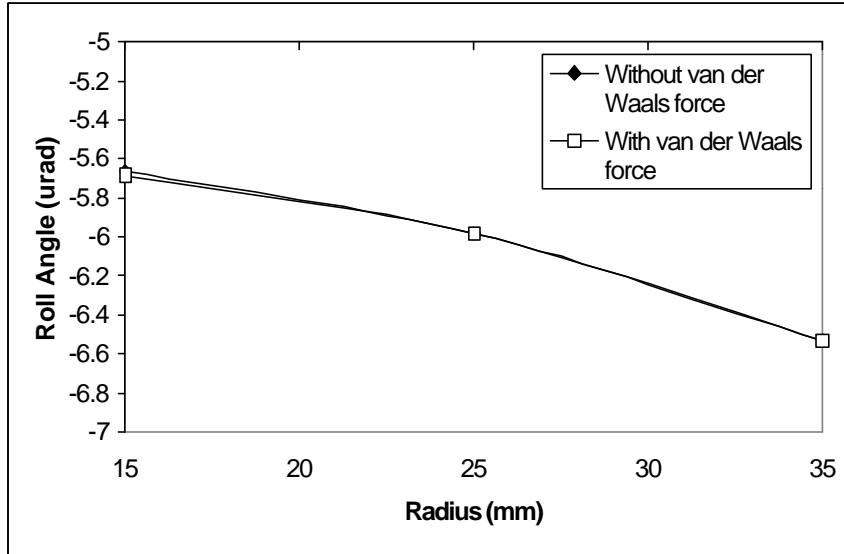
different radial positions.

Fig. 7.8 The effect of the van der Waals force on the roll angle of the Tripad slider at

different radial positions.

Fig. 7.9 The Femto negative pressure slider and the unstructured triangular meshes.

Fig. 7.10 Air bearing forces, the van der Waals force and the load capacity as a function

of the flying height for the Femto slider at a fixed pitch angle of $150\,\mu rad$.
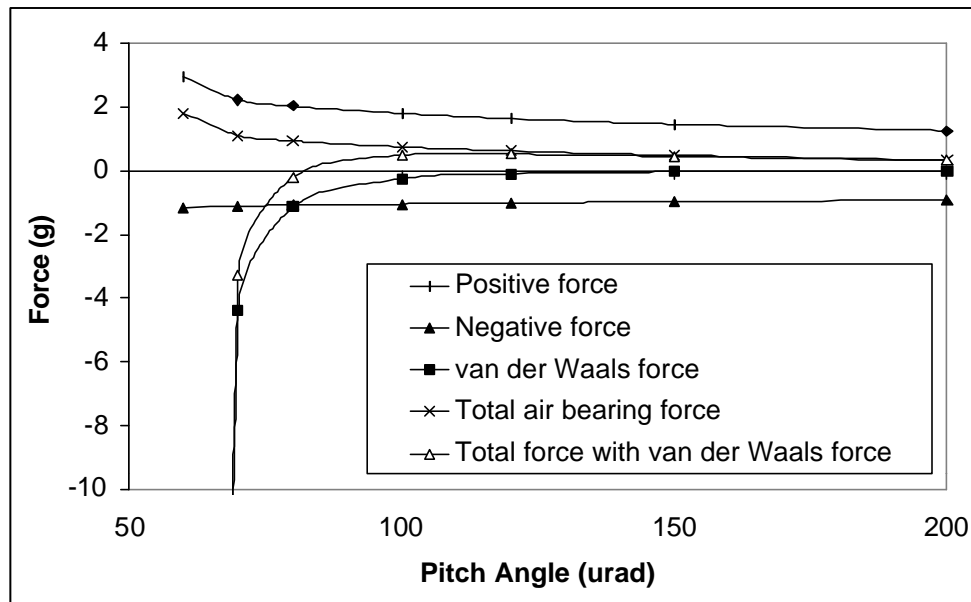
Fig. 7.11 Air bearing forces, the van der Waals force and the load capacity as a function

of the pitch angle for the Femto slider at a fixed flying height of 4 nm.

150
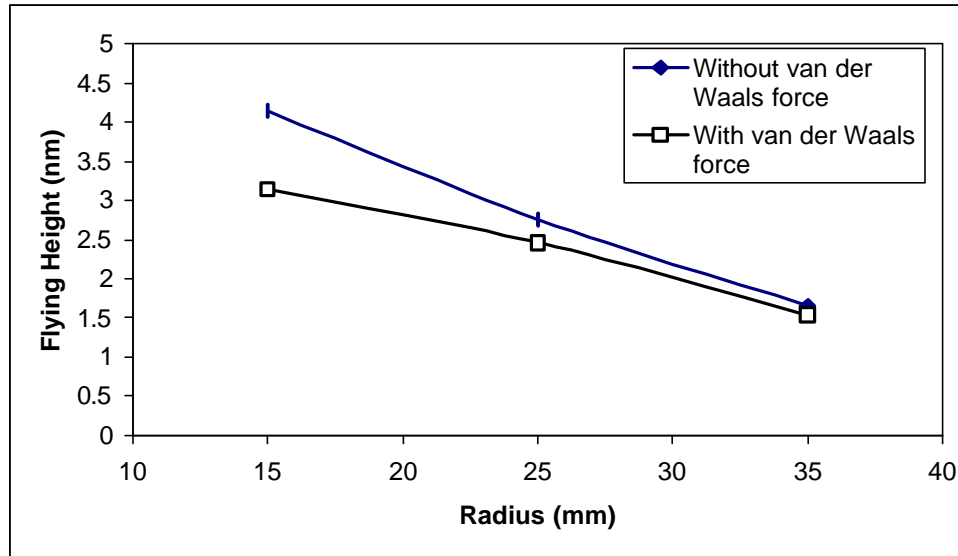
Fig. 7.12 The effect of the van der Waals force on the flying height of the Femto slider at

different radial positions.
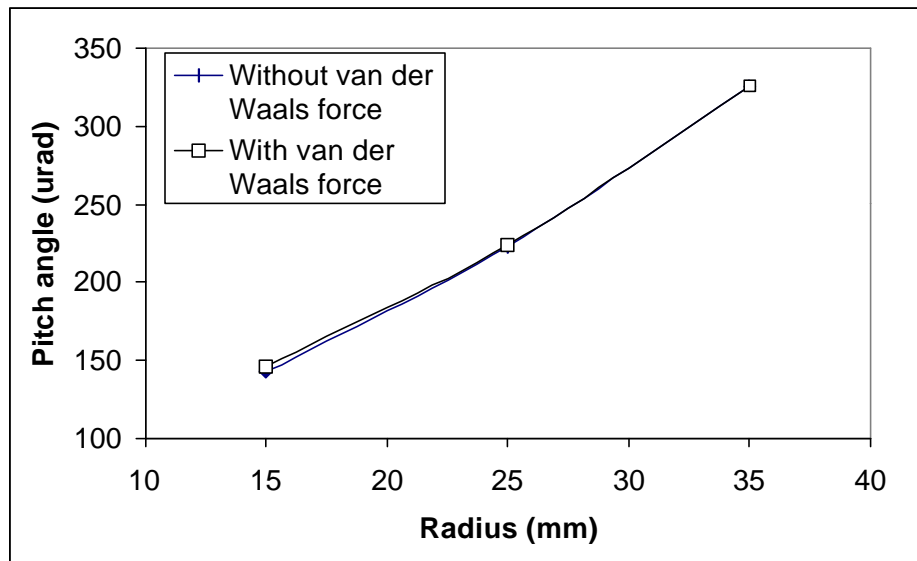
Fig. 7.13 The effect of the van der Waals force on the pitch angle of the Femto slider at

different radial positions.
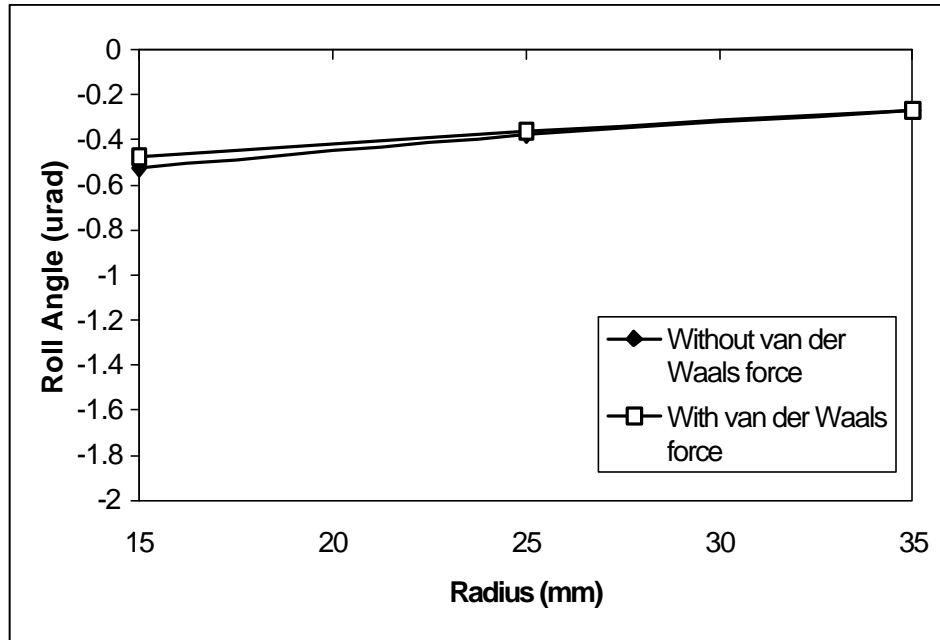
Fig. 7.14 The effect of the van der Waals force on the roll angle of the Femto slider at
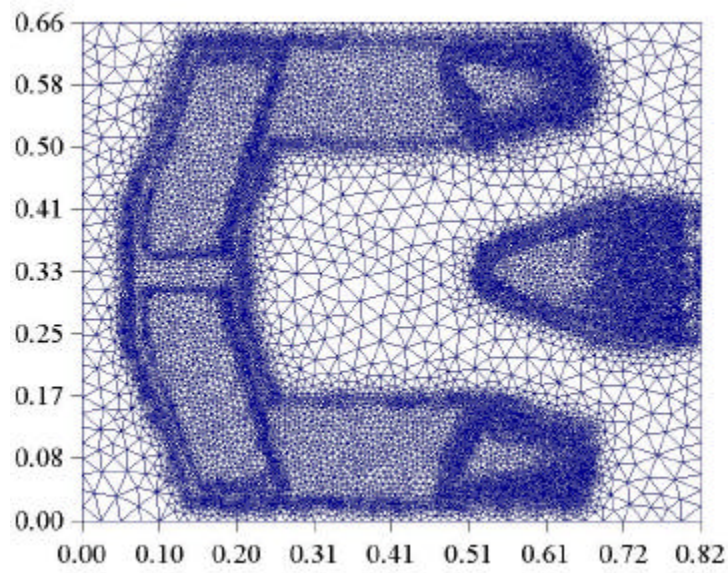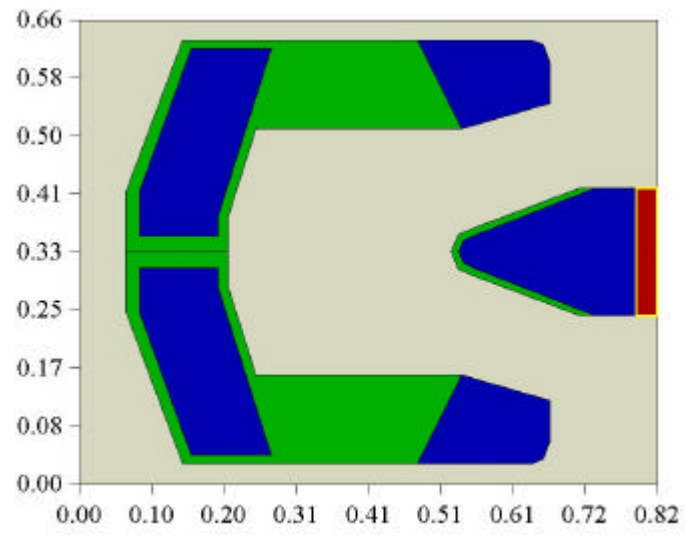
different radial positions.
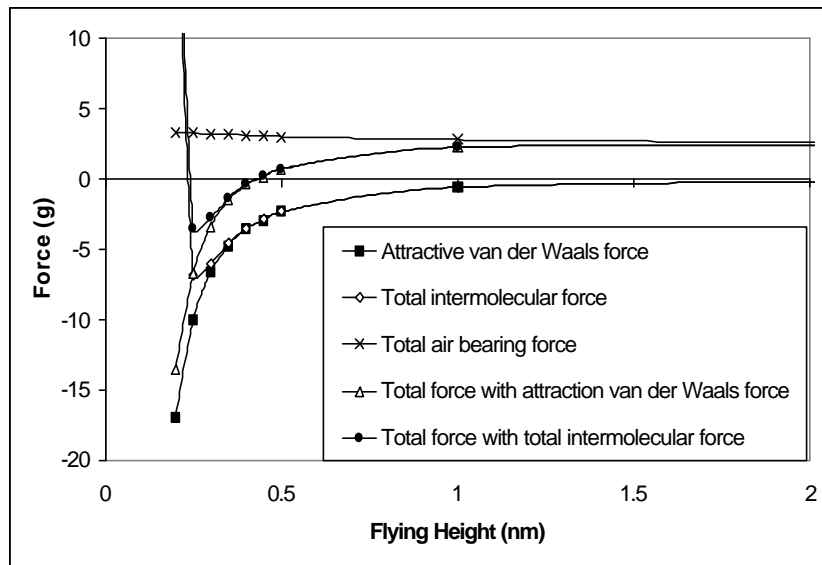
Fig. 7.15 The attractive van der Waals force, the total intermolecular force, the total air bearing force and the load capacity as a function of the flying height for the Tripad slider at a fixed pitch angle of $150\,mrad$.
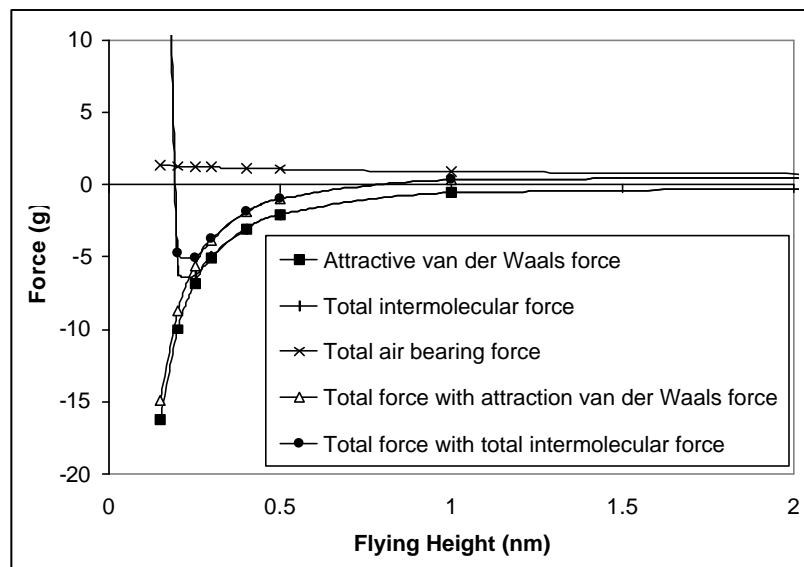
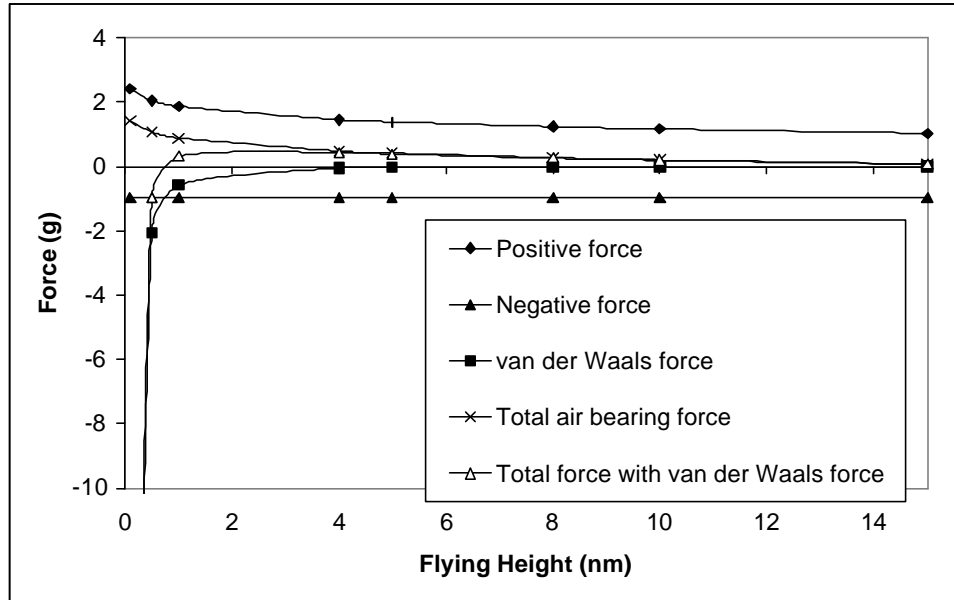**Fig. 7.16** The attractive van der Waals force, the total intermolecular force, the total air bearing force and the load capacity as a function of the flying height for the Femto slider at a fixed pitch angle of $150\,mrad$.

CHAPTER 8

CONCLUSION

As the spacing between the slider and the disk surface has been reduced to a few nanometers to achieve higher areal storage density in the hard disk drives, the physical modeling of the problem becomes even more difficult. This thesis partially addressed this problem by the derivation of two new compressible lubrication equations.

In Chapter 2, a new slip velocity boundary condition at the gas-solid interface is derived through a momentum balance along the wall direction for the compressible problem. Additional slippage is introduced by the Poiseuille flow effect. A new modified Reynolds equation for isothermal and compressible gas lubrication is then derived by using the new slip velocity boundary condition. The resulting equation has a form similar to that of the second order and the 1.5 order slip models in the literature but with different coefficients that come from terms associated with the higher order slippage correction. The new model, together with the second order and the 1.5 order slip models, are theoretically and numerically shown to have no unbounded contact pressure singularities for a 1-D parabolic asperity contact problem. But the first order slip model and the FK model have such unbounded contact pressure singularities. A shock wave like discontinuity is observed at the contact point. When the asperity approaches contact, a boundary layer appears around the minimum spacing point. A new contact boundary condition for the Reynolds equation at the converging or diverging corner is proposed, based on the asymptotic analysis, which can be used as the numerical boundary condition at the contact edge in the numerical simulation if locally the geometry near the contact

point can be approximated by a parabola. The results show that for any modified Reynolds equation to be free of a contact pressure singularity, it must have diffusion terms that go to zero no faster than the convection terms near the contact point as the minimum spacing is reduced to zero.

In Chaper 3, the first order and second order slip model lubrication equations are re-derived from a more physical point of view. The derivation is free of any arbitrarily chosen value of the length scales used in the Taylor expansion of the mean velocity. The newly derived lubrication equations have forms similar to the old first order and the second order slip models, but the new second order slip model predicts results closer to the FK model when the modified inverse Knudsen number is small. The new second order slip model equation does not suffer from the pressure singularity of the FK model at contact.

To evaluate the performance of all existing models, the flying height and the pitch angle of a practical slider are obtained by solving the different modified Reynolds models using numerical methods described in Chapters 4 and 5. Figure 8.1 shows the design of a slider. Figure 8.2 shows the slider's flying height at different radial positions as predicted by all known modified models. As can be seen different models predict different flying heights. The new 1st order slip model predicts the highest, and the pressure gradient slip model of the previous chapter predicts the lowest. The old 2nd order slip model gives the closest prediction to the FK model. But this is not contradictory to previous observation that the new second order slip model predicts closer result to FK model than the old 2nd slip model when the modified inverse Knudsen number is small. This slider's pitch angle is relatively large, so the inverse Knudsen number in most of the air bearing surface

155

region is not so small except at the trailing edge, and the slider's flying height is determined by the air bearing force contributions from all regions. Figure 8.3 shows the slider's pitch angle at different radial positions. As expected, the different models predicts different pitch angles also. The largest difference among them is about 10 $mrad$.

The different models predict different flying heights due to the different amount of the diffusion effect introduced by them. The old 1st order slip model and the new 1st order slip model have a similar form. But the new model has a coefficient 4 instead of 6, as a result, it has less diffusion effect and predicts higher pressure than the old model, which results in a higher flying height. Similar arguments go for the old 2nd order, the 1.5 order, the new 2nd order and the pressure gradient slip models. All of them have a similar form but with different coefficients. The new 2nd slip model has the smallest diffusion effect and predicts the highest flying height. The pressure gradient slip model has the largest diffusion effect and predicts the lowest flying height. Since there are no two models that predict similar results, a natural question is which model gives predictions that are closest to the actual physics? This is a difficult question to answer unless large amounts of repeatable and reliable experimental data become available. Nevertheless, from the derivation point of view, since the new 1st order and 2nd order slip models do not take the Taylor expansion length scale to be the mean free path, but instead they average over all solid angles, the new 1st and 2nd slip models are assumed to be better than the old 1st and 2nd slip models. The pressure gradient slip model introduces additional slippage due to pressure gradient into the slip velocity boundary conditions, which removes the unbounded contact pressure singularity found in the 1st order slip and the FK models. As

a result, it rests on more formal physical ground than the 1st and the 2nd slip models. From this point of view, it is preferable than the 1st and 2nd slip models. The FK model is derived from the linearized Boltzmann equation (BGK equation), which includes both the slip effect and the rarefaction effect. It seems that the FK model includes the most physics among all models, but it predicts an unbounded contact pressure singularity, which is unphysical and requires ad hoc modification for low flying slider designs that may have asperity contact.

To improve the efficiency and accuracy of numerical solution of the air bearing problem, we developed in Chapters 4,5 and 6, unstructured triangular mesh generation techniques and multi-grid finite volume numerical methods.

In Chapter 4, three different mesh refinement and adaptation techniques based on two different Delaunay triangulation algorithms have been utilized to automatically cluster fine meshes to the rail top, the recess wall and the high pressure gradient regions of the slider. The overall mesh generation process gives the user great flexibility and control over the distribution and quality of the meshes. This is demonstrated to be an efficient and convenient way of generating quality meshes over the complex geometries in the air bearing simulations. An explicit finite volume scheme is first constructed and then successfully extended to be fully implicit. The resulting scheme is unconditionally stable, and an arbitrarily large time step can be used.

In Chapter 5, a non-nested FAS multi-grid algorithm has been successfully employed to speed up the convergence rate of the implicit finite volume scheme. The multi-grid algorithm requires no relationship between different mesh levels. On the average, nearly

one order of simulation time has been saved by implementing the multi-grid algorithm. In addition the steady state flying attitude is found by a Quasi-Newton method.

In Chapter 6, to further improve the accuracy and the efficiency of the code, three different schemes are used to discretize the convection part of the generalized Reynolds equation, and a Galerkin finite element approach is used to model the diffusion part of the equation. The resulting numerical schemes are shown to be unconditionally stable. To get comparable results the PSI and the SUPG triangular mesh solvers are generally four to five times faster than the previously developed CML rectangular mesh solver depending on the complexity of the rail shape, due to the much improved grid point position strategy and the increased accuracy of the scheme. Among the schemes, the PSI and the SUPG schemes are the most accurate and achieve grid convergence at the smallest node number.

A new software package is formed by combining the grid generator and the solvers together. The overall software package is user friendly and robust and it can meet the industrial demand to some extent.

The effect of the intermolecular forces between the slider and the disk on the flying attitude of the slider is also studied in Chapter 7. It is found that the van der Waals force has significant influence on the flying height and has non-negligible effect on the pitch angle for both positive pressure sliders and negative pressure sliders, when the flying height is below 5 nm. When the flying height is below 0.5 nm, the repulsive portion of the intermolecular force becomes important and also has to be included.

All of the developments of this thesis have been implemented in the CML Air Bearing Design Code under the new user friendly interface.
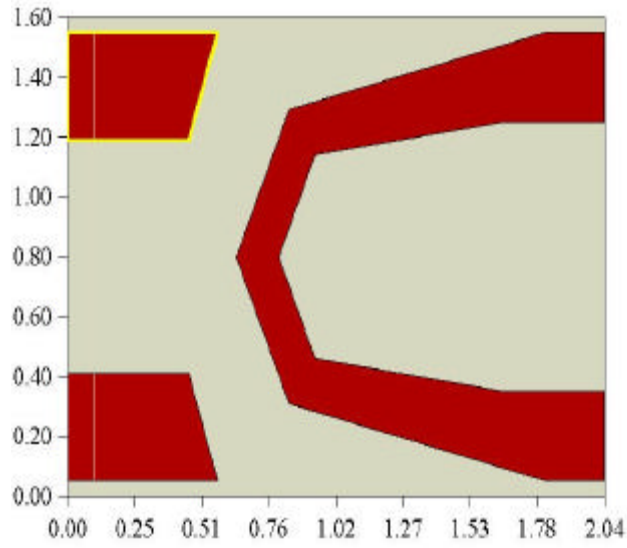
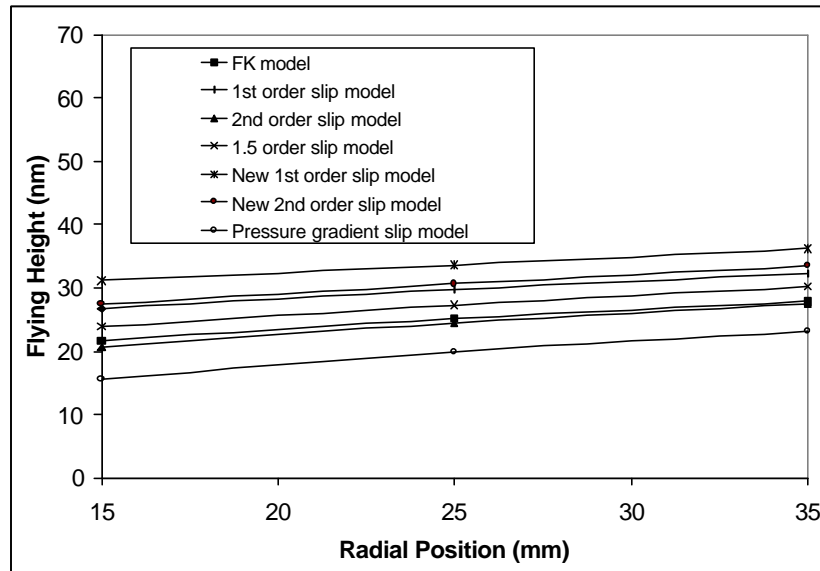**Fig. 8.1** The geometry of a slider design (mm).

Fig. 8.2 The slider's flying height at different radial positions as predicted by the
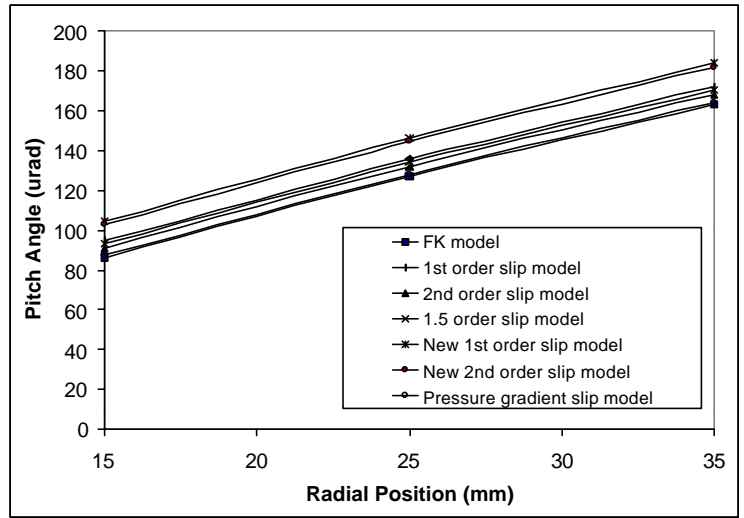
different models.

Fig. 8.3 The slider's pitch angle at different radial positions as predicted by the different models.

REFERENCES

Anaya-Dufresne, M., 1996, "On the development of a Reynolds equation for air bearings with contact," Doctoral dissertation, Department of Mechanical Engineering, Carnegie Mellon University, Pittsburgh, PA.

Anaya-Dufresne, M., and Sinclair, G. B., 1997, "On the breakdown under contact conditions of Reynolds equation for gas lubricated bearings," *ASME J. of Tribology*, Vol. **119**, pp. 71-75.

Barth, T. J., 1991, "Numerical Aspects of Computing Viscous High Reynolds Number Flows on Unstructured Meshes," *AIAA paper 91-0721*.

Barth, T. J., 1993, "Recent Developments in High Order k-exact Reconstruction on Unstructured Meshes," *AIAA paper 93-0668*.

Barth, T. J., and Jespersen, D. C., 1989, "The Design and Application of Upwind schemes on Unstructured Meshes," *AIAA paper 89-0366*.

Brandt, A., 1977, "Multi-Level Adaptive Solutions to Boundary Value Problems," *Math. Comp.*, Vol. 31, pp. 333-390.

Bowyer, A., 1981, "Computing the Dirichlet Tessellations," *Comput. J.*, Vol. 24, No. 2, pp. 162-166.

Burgdorfer, A., 1959, "The influence of the molecular mean free path on the performance of hydrodynamic gas lubricated bearing," *ASME J. of Basic Engineering*, Vol. **81**, pp. 94-100.

Dennis, J. E., and Schnabel, R. B., 1983, *Numerical Methods for Unconstrained Optimization and Nonlinear Equations* , Prentice-Hall, Englewood Cliffs, New Jersey.

Fukui, S., and Kaneko, R., 1990, "Analysis of Ultra-Thin Gas Film Lubrication Based on Linearized Boltzmann Equation: First Report-Derivation of a Generalized Lubrication Equation Including Thermal Creep Flow," *ASME J. of Tribology*, Vol. **110**, pp. 335-341.

Fukui, S., and Kaneko, R., 1990, "A database for interpolation of Poiseuille flow rates for high Knudsen number lubrication problems," *ASME J. of Tribology*, Vol. **112**, pp. 78-83.

Garcia-Suarez, C., Bogy, D. B., and Talke, F. E., 1984, "Use of an Upwind Finite Element Scheme for Air Bearing Calculations," *ASLE SP-16*, pp. 90-96.

Hsia, Y. T., and Domoto, G. A., 1983, "An experimental investigation of molecular rarefaction effects in gas lubricated bearings at ultra-low clearances," *ASME J. of Lubrication Technology*, Vol. **105**, pp. 120-130.

Huang, W., and Bogy, D. B., 1998, "An investigation of a slider air bearing with a asperity contact by a three dimensional direct simulation Monte Carlo method," *IEEE Trans. on Magnetics*, Vol. **34**, pp. 1810-1812.

Huang, W., Honchi, M., and Bogy, D. B., 2000, "An asperity contact model for the slider air bearing," *ASME J. Tribology*, Vol. **122**, pp. 436-443.

Israelachvili, J. N., 1992, *Intermolecular and surface forces*, 2nd ed., Academic Press, San Diego.

Kennard, E. H., 1938, *Kinetic Theory of Gases*, Mcgraw-Hill Book Co., New York.

Lawson, C. L., 1977, *Mathematical Software III*, pp.161-194. Academic Press, New York.

Lo, S. H**.,** 1985, "A New Mesh Generation Scheme for Arbitrary Planar Domains," *Int. J. Numer. Methods. Eng***.,** Vol. **21**, pp. 1403-1426.

Lu, S., 1997, "Numerical Simulation of Slider Air Bearings," Doctoral Dissertation, Department of Mechanical Engineering, University of California, Berkeley.

Lu, S. and Bogy, D. B., 1994, "a Multi-grid Control Volume Method for the Simulation of Arbitrarily Shaped Slider Air Bearings with Multiple Recess Levels," *Technical*

Report No. 94-016 (not published), Computer Mechanics Laboratory, University of California at Berkeley.

Mavriplis, D. and Jameson, A., 1987, "Multigrid Solution of the Two-Dimensional Euler Equations on Unstructured Triangular Meshes," *AIAA paper 87-0353*.

Mavriplis, D. J., 1988, "Multigrid Solution of the Two-Dimensional Euler Equations on Unstructured Triangular Meshes," *AIAA J.*, Vol. **26**, pp. 824-831.

Mitsuya, Y., 1993, "Modified Reynolds equation for ultra-thin film gas lubrication using 1.5-order slip-flow model and considering surface accommodation coefficient," ASME J. of Tribology, Vol. **115**, pp. 289-294.

Patankar, S. V., 1980, *Numerical Heat Transfer and Fluid Flow*, McGraw-Hill, New York.

Press, W. H., Teukolsky, S. A., Vetterling, W. T., and Flannery, B. P., 1992, *Numerical Recipes in Fortran 77*, Cambridge University Press.

Rebay, S., 1993, "Efficient Unstructured Mesh Generation by Means of Delaunay Triangulation and Bowyer-Watson Algorithm," *J. Comput. Phys.*, Vol. 106, pp. 125-138.

Rivara, M. C., 1989, "Selective Refinement/Derefinement Algorithms for sequences of nested triangulations," *Int. J. Numer. Methods Eng.*, Vol. 28, pp. 2889-2906.

Rivara, M., 1997, "New Longest-edge Algorithms for the Refinement and/or Improvement of Unstructured Triangulations," *Int. J. Numer. Methods. Eng.*, Vol. 40, pp. 3313-3324.

Rivara, M., and Inostroza, P., 1997, "Using Longest-side Bisection Techniques for the Automatic Refinement of Delaunay Triangulations," *Int. J. Numer. Methods. Eng.*, Vol. 40, pp. 581-597.

Ruppert, J., 1995, "A Delaunay Refinement Algorithm for Quality 2-Dimensional mesh Generation," *J. of Algorithms*, Vol. 18, pp. 548-585.

Sloan, S. W., 1987, "A Fast Algorithm for Constructing Delaunay Triangulations in the Plane," *Advances in Engng Software*. Vol. 9, pp. 34-55.

Thompson, J. F., Thames, F. C., and Mastin, C. W., 1977, "Boundary-Fitted Curvilinear Coordinate Systems for the Solution of Partial Differential Equations on Fields Containing Any Number of Arbitrary Two-Dimensional Bodies," *NASA CR-2729*.

Zeng, Q. H. and Bogy D. B., 1999, "Slider air bearing designs for load/unload applications," *IEEE Trans. on Magnatics* , Vol. **35**, pp. 746-751.

Zhang, B., and Nakajima, A., 2000, "Surface force in slider air bearings of hard disks," 27th Leeds-Lyon Symposium on Tribology.

Watson, D. F., 1981, "Computing the N-Dimensional Delaunay Tesselation with Application to Voronoi Polytopes," *Comput. J.* , Vol. 24, No.2, pp. 167-172.

White, J. W. and Nigam, A., 1980, "A Factored Implicit Scheme for the Numerical Solution of the Reynolds Equation at Very Low Spacing," *ASME J. Lubrication Technology*, Vol. 102, pp. 80-85.